



universität  
wien

# MASTERARBEIT / MASTER'S THESIS

Titel der Masterarbeit / Title of the Master's Thesis

„Excited state dynamics of 5,6-dihydroxyindole, a  
eumelanin building block in water and methanol“

verfasst von / submitted by

Moritz Heindl, BSc

angestrebter akademischer Grad / in partial fulfilment of the requirements for the degree of  
Master of Science (MSc)

Wien, 2017 / Vienna, 2017

Studienkennzahl lt. Studienblatt /  
degree programme code as it appears on  
the student record sheet:

A 066 862

Studienrichtung lt. Studienblatt /  
degree programme as it appears on  
the student record sheet:

Masterstudium Chemie

Betreut von / Supervisor:

Univ.-Prof. Dr. Leticia González Herrero



# Contents

<b>Abstract</b>	<b>i</b>
<b>List of Abbreviations</b>	<b>iv</b>
<b>List of Symbols</b>	<b>v</b>
<b>1 Introduction</b>	<b>1</b>
1.1 Motivation . . . . .	1
1.2 State of the Art . . . . .	2
1.3 Scope of this Thesis . . . . .	4
<b>2 Theory</b>	<b>5</b>
2.1 The Schrödinger equation . . . . .	5
2.2 The Born-Oppenheimer Approximation . . . . .	5
2.3 Electronic Structure Methods . . . . .	8
2.3.1 Hartree-Fock Approximation . . . . .	8
2.3.2 Configuration Interaction . . . . .	10
2.3.3 Multi-Configurational Self-Consistent Field . . . . .	13
2.3.4 Perturbation Theory . . . . .	14
2.3.5 Algebraic Diagrammatic Construction . . . . .	18
2.3.6 Density Functional Theory . . . . .	20
2.4 Surface Hopping Dynamics . . . . .	23
2.4.1 Propagation of the Nuclei and the Electronic Wavefunction	24
2.4.2 Hopping Probabilities . . . . .	26
2.4.3 Wigner Sampling . . . . .	26
<b>3 Results and Discussion</b>	<b>28</b>
3.1 Cluster Systems . . . . .	28
3.1.1 DHI-H <sub>2</sub> O Cluster . . . . .	30
3.1.2 DHI-MeOH Cluster . . . . .	30
3.2 Stationary Excited State Calculations . . . . .	31
3.2.1 CASPT2 Electronic Structure of the Clusters . . . . .	33
3.2.2 Preliminary Benchmarking . . . . .	34
3.3 Non-adiabatic Dynamics Calculations . . . . .	38
3.3.1 ADC(2) Trajectories . . . . .	38

3.3.2	CASSCF Trajectories . . . . .	42
3.3.3	Relaxation Pathways in the Cluster Systems . . . . .	45
3.4	A Posteriori Benchmarking of CASSCF . . . . .	58
3.4.1	Static Calculations at Key Points in the Trajectories . . . . .	58
3.4.2	Rigid Scans . . . . .	60
<b>4</b>	<b>Summary</b>	<b>62</b>
<b>A</b>	<b>Appendix</b>	<b>64</b>
A.1	Initial Stationary Calculations . . . . .	64
A.2	Increasing the Size of the Microsolvation Model . . . . .	64
A.3	Influence of the Chosen Method on the Geometry of the Clusters . . . . .	66
	<b>Bibliography</b>	<b>69</b>
	<b>Acknowledgments</b>	<b>77</b>

# Abstract

It is the goal of this work to contribute to the elucidation of the excited state relaxation dynamics of 5,6-dihydroxyindole (DHI), which is one of the main building blocks of eumelanin, after irradiation with UV light. To this end, non-adiabatic surface hopping dynamics have been employed using as a starting point recent theoretical and experimental findings[Nogueira *et al.*, *J. Phys. Chem. Lett.* 8(5) 1004-1008, 2017] on the deactivation mechanism of DHI in water and methanol. These findings proposed a transfer of an electron and a proton to the surrounding solvent as a first step in the deactivation mechanism. Investigation of excited state dynamics following this first step is the focus of this work. The algebraic diagrammatic construction scheme of second order (ADC(2)) and the complete active space self-consistent field (CASSCF) methods were used for the underlying electronic structure calculations of the dynamics simulations. Using two methods for the dynamics allows for cross-validation of both methods which is important to verify the accuracy of CASSCF on this system as CASSCF is not as reliable as ADC(2) for specific systems. Once the accuracy of CASSCF is validated, it offers more information about our system as it allows the simulation of the dynamics after relaxation to the ground state, which is not possible with ADC(2).

In water, 60% and 65% of the trajectories returned to the ground state when using ADC(2) and CASSCF, respectively. The corresponding deactivation time constants were found to be 274 fs with ADC(2) and 196 fs with CASSCF. In methanol, 90% and 85% of ADC(2) and CASSCF trajectories relaxed to the ground state. The associated time constants equal 18 fs for ADC(2) and 24 fs for CASSCF. Therefore, both methods agreed well on the amount of deactivating trajectories and the order of magnitude of the corresponding time constants.

The CASSCF simulations revealed two different relaxation pathways from the first excited state to the ground state: A restoring pathway where first the electron and then the proton returns from the solvent to DHI, and a dissociative pathway where a hydrogen radical is formed. The restoring pathway was found to be the major deactivation channel in water while the dissociative pathway was found to be favored in methanol.

# Abstract

Diese Arbeit hat sich die Untersuchung relaxationsdynamischer Prozesse eines Hauptbestandteils von Eumelanin, 5,6-Dihydroxyindol (DHI), nach Anregung mit UV Licht zum Ziel gesetzt. Den Grundstein dieser Untersuchung bildet die aktuelle experimentelle und theoretische Arbeit von Nogueira *et al.* [Nogueira *et al.*, *J. Phys. Chem. Lett.* 8(5) 1004-1008, 2017], welche die Relaxationsprozesse von DHI in Wasser und Methanol behandelt. Die theoretische Untersuchung dieser Systeme führte zur Postulierung eines Deaktivierungsmechanismus', der auf dem Transfer eines Elektrons und in der Folge eines Protons von DHI zum umgebenden Lösungsmittel basiert. Die vorliegende Arbeit befasst sich mit den dynamischen Prozessen, die diesen einleitenden Schritten folgen. Diese Untersuchung erfolgt mittels computergestützter Simulation dynamischer Prozesse unter Verwendung nicht-adiabatischer surface-hopping Simulationen. Für die Berechnungen der elektronischen Struktur des Systems im Lauf der Simulationen wurden zwei verschiedene Methoden gewählt: zum einen das Algebraic Diagrammatic Construction scheme of second order (ADC(2)) und zum anderen die Complete Active Space Self-Consistent Field (CASSCF) Methode. ADC(2) ist eine stabile Methode, die jedoch den Nachteil hat, dass es nicht möglich ist, die Dynamik weiterzuverfolgen sobald der Grundzustand und der erste angeregte Zustand kreuzen. CASSCF erlaubt die Simulation über diesen Zeitpunkt hinaus, kann aber je nach System Ergebnisse unterschiedlich guter Qualität liefern. Die Simulationen wurden mit beiden Methoden ausgeführt, da diese sich ergänzen: Die ADC(2) Simulationen können verwendet werden um die Genauigkeit der CASSCF Simulationen abzuschätzen bis dieser Kreuzungspunkt erreicht wird, während die CASSCF Dynamik Informationen nach diesem Punkt liefern kann.

In Wasser relaxierten 60% der mit ADC(2) simulierten Trajektorien zum Grundzustand und 65% der mit CASSCF simulierten. Die dazugehörigen Relaxationskonstanten sind 274 fs mit ADC(2) und 196 fs mit CASSCF. In Methanol erreichten 90% (ADC(2)) und 85% (CASSCF) der Trajektorien den Grundzustand. Die Relaxationszeitkonstanten betragen 18 fs mit ADC(2) und 24 fs mit CASSCF. Somit wurde eine gute Übereinstimmung zwischen ADC(2) und CASSCF Trajektorien erzielt was die Verwendung von CASSCF zur Bestimmung des Deaktivierungsmechanismus' nach der Relaxation zum Grundzustand rechtfertigt.

Die CASSCF Simulationen zeigten die Existenz zweier Deaktivierungsmechanismen in beiden Lösungsmitteln auf: einerseits gibt es einen wiederherstellenden Mechanismus im Zuge dessen zuerst das Elektron und dann das Proton vom Lösungsmittel zu DHI transferriert werden. Andererseits existiert ein dissozierender Mechanismus bei dem ein Wasserstoffradikal gebildet wird. Der wiederherstellende Mechanismus wurde vorwiegend in Wasser beobachtet während der dissozierende der dominierende Mechanismus in Methanol ist.

# List of Abbreviations

---

---

DHI	5,6-Dihydroxyindole
PES	Potential energy surface
NAC	Non-adiabatic coupling
HF	Hartree-Fock
SCF	Self-consistent field
CI	Configuration interaction
CID	Configuration interaction including doubly excited determinants
MCSCF	Multi-configurational self-consistent field
SA	State-averaging
CASSCF	Complete active space self-consistent field
CASPT2	Complete active space second order perturbation theory
FOI	First-order interaction space
DFT	Density functional theory
HK	Hohenberg-Kohn
KS	Kohn-Sham
ADC	Algebraic diagrammatic construction
SHARC	Surface hopping including arbitrary couplings
H <sub>2</sub> O	Water
MeOH	Methanol
CT	Charge transfer

---

---

# List of Symbols

---

---

$t$	Time
$c_i$	Coefficient
$a_i$	Coefficient in the CI expansion
$n_{el}$	Number of electrons
$N_{nu}$	Number of nuclei
$n_\phi$	Number of orbitals
$M_A$	Mass of the nucleus $A$
$Z_A$	Charge of the nucleus $A$
$r_{ij}$	Distance between electron $i$ and electron $j$
$R_{AB}$	Distance between nucleus $A$ and nucleus $B$
$w$	Weight in the SA-approach
$h_{\beta \rightarrow \alpha}^{diag}$	Hopping probability in the diagonal representation
$v_{KS}$	Kohn-Sham potential
$v_{ex}$	External potential
$v_{HF}$	Hartree-Fock potential
$v_{xc}$	Exchange-correlation potential
$f_{xc}$	Exchange-correlation kernel
$l$	CASPT2 level shift value
$x$	Coordinates of the normal mode
$p$	Momentum of the normal mode
$\xi$	Spin coordinate
$\kappa$	Spin funcion
$\theta$	Basis function
$\rho$	Electron density
$\lambda$	Perturbation factor
$\iota$	Eigenvalue in the linear response matrix equation
$\delta$	Kronecker delta
$\omega$	Frequency
$\mu$	Reduced mass
$\eta$	Angular momentum
$\Pi$	Polarization propagator

---

---

---



---

$E_{tot}$	Total energy
$E_{el}$	Electronic energy
$E_{PES}$	Energy of the potential energy surface
$E_{HF}$	Hartree-Fock energy
$E_{corr}$	Correlation energy
$E_{CI}$	Configuration interaction energy
$E_{MCSCF}$	MCSCF energy
$E_{MCSCF}^{av}$	SA-MCSCF energy
$\epsilon_i$	Orbital energy
$e_{solv}^-$	Solvated electron
$\Psi$	Wavefunction
$\Psi_{nu}$	Nuclear wavefunction
$\Psi_{el}$	Electronic wavefunction
$\Psi_{HF}$	Hartree-Fock wavefunction
$\Psi_{CI}$	Configuration interaction wavefunction
$\Psi_{MCSCF}$	Multi-configuration self-consistent field wavefunction
$\chi$	Spin orbital
$\chi_{occ}$	Occupied spin orbital
$\chi_{vir}$	unoccupied spin orbital
$\phi$	Spatial orbital
$\phi^{KS}$	Kohn-Sham orbital
$\Phi$	Determinant
$\Phi_{HF}$	Hartree-Fock determinant
$\Phi_{i \neq 0}$	Excited determinant
$\Phi_{ij}$	Doubly excited determinant
$\vec{R}$	Spatial position of the nuclei
$\bar{R}$	Parametric dependence on the spatial position of the nuclei
$\vec{r}$	Spatial position of the electrons
$\vec{v}$	Classical velocity of the nuclei
$\vec{a}$	Classical acceleration of the nuclei
$\vec{c}$	Coefficients of the electronic states

---



---

---



---

$\hat{H}$	Hamilton Operator
$\hat{H}_0$	Unperturbed Hamilton Operator
$\hat{H}'$	Perturbed Hamilton Operator
$\hat{T}$	Kinetic energy operator
$\hat{T}_{nu}$	Kinetic energy operator for the nuclei
$\hat{T}_{el}$	Kinetic energy operator for the electrons
$\hat{V}$	Potential energy operator
$\hat{V}_{nu,nu}$	Potential energy operator between two nuclei
$\hat{V}_{nu,el}$	Potential energy operator between nuclei and electrons
$\hat{V}_{el,el}$	Potential energy operator between two electrons
$\hat{f}$	Fock operator
$\hat{h}$	One-electron operator
$\hat{J}$	Coulomb operator
$\hat{K}$	Exchange operator
$\hat{\gamma}$	Creation operator
$\hat{\gamma}^\dagger$	Annihilation operator
<b>F</b>	Fock matrix
<b>C</b>	Coefficient matrix
<b>S</b>	Overlap matrix
$\epsilon$	Orbital energy matrix
<b><math>\Pi</math></b>	Matrix of the polarization propagator
<b>x</b>	Transition amplitude matrix
<b>1</b>	Unit matrix
<b><math>\Omega</math></b>	Excitation energy matrix
<b>Y</b>	Transformation matrix
<b>M</b>	Transformed excitation energy matrix
<b>f</b>	Transformed transition amplitude matrix
<b>H</b>	Hamilton matrix
<b>H<sup>diag</sup></b>	Diagonalized Hamilton matrix
<b>T</b>	Coupling matrix
<b>P</b>	Propagator matrix
<b>P<sup>diag</sup></b>	Propagator matrix in the diagonal representation

---



---

# 1. Introduction

## 1.1 Motivation

Melanins form a large class of heterogeneous pigments that can be found in all classes of living organisms like animals, plants, and fungi.<sup>1</sup> In humans, melanins are mainly responsible for the pigmentation of skin, hair, and eyes, but high concentrations have also been detected in the inner ear and in parts of the brain.<sup>2</sup> In epidermal cells, two types of melanins can be distinguished: the dark eumelanin and the reddish-yellow pheomelanin. Both pigments are formed in the melanocytes from dopaquinone in a multi-step process which either yields monomeric eumelanin building blocks in the absence of thiols, or pheomelanin ones in their presence.<sup>3</sup> These constituents readily undergo oxidative polymerization and form either eumelanin or pheomelanin pigments. Experimental investigations revealed that the structure of these pigments follows a strict hierarchical order.<sup>4</sup> This is shown in Figure 1.1 where the monomers form oligomeric sheets of unknown size that stack via  $\pi\pi$  interactions with other oligomeric sheets. These large assemblies then in turn aggregate to form the whole pigment.

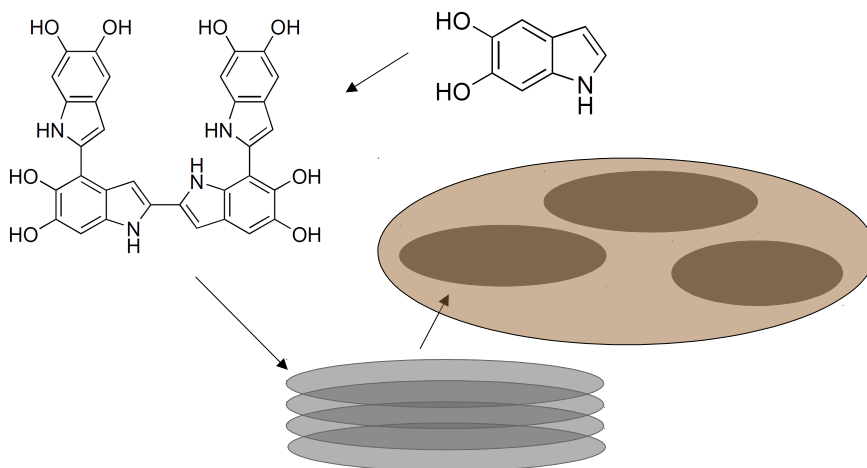


**Figure 1.1:** Organization order of building blocks in the formation of a melanin pigment.

The main biological function of eumelanin and pheomelanin pigments is the photo-protection of DNA against UV induced damages.<sup>5</sup> The photoprotection provided by melanins does not depend only on the amount of melanin pigments but also on their type since eumelanin acts as an anti-oxidant while pheomelanin has been shown to promote the formation of reactive oxygen species.<sup>6</sup> This could be one of the reasons why the risk for formation of skin cancer is 70 times higher for people with fair skin than for people with dark skin, as the ratio of eumelanin to pheomelanin is lower in people with fair skin. Due to its biological relevance, the mechanisms of how eumelanin is capable of dissipating the absorbed UV energy without suffering structural damage have received increased interest throughout the last decade.

## 1.2 State of the Art

Investigation of the excited state deactivation pathways of the whole eumelanin pigment revealed ultrafast non-radiative relaxation to the electronic ground state and formation of a small amount of another long-lived species.<sup>7,8</sup> However, the experimentalists were confronted with the inability to pinpoint the contributions of the various molecular species present in eumelanin to the observed excited-state decay. This whole investigation is hindered even further by the fact that the actual composition of the whole pigment is still unknown as a lot of different species can be found in the pigments at once. Furthermore, it is still not clear, to what extent these pigments are solvent-accessible. The heterogeneity found in the eumelanin pigment resulted in the emergence of a bottom-up approach in the investigation of this compound, where the excited state dynamics of smaller building blocks are investigated. Knowledge of the excited-state behavior of the building blocks of eumelanin is expected to finally lead to the unraveling of the mysteries surrounding the eumelanin excited-state deactivation. Recently, spectroscopic studies on synthetic eumelanin polymers and quantum chemical calculations revealed that the broad absorption spectrum of the melanin pigment can be assembled by combining the absorption spectra of independent oligomeric units.<sup>9-11</sup> Therefore, a large number of investigations focuses on monomeric, dimeric, trimeric and tetrameric systems of the main building blocks of eumelanin, which are 5,6-dihydroxyindole-2-carboxylic acid (DHICA) and 5,6-dihydroxyindole (DHI). Small structural or geometric disorder in these oligomeric units lead to a monotonically increasing absorbance towards lower wavelengths, as has been shown both experimentally and theoretically.<sup>12-15</sup> It has also been proposed, that the reduced forms of these building blocks partake in the deactivation mechanism<sup>16</sup> or play an essential role in the UV absorption pattern.<sup>17</sup> This reduction in the size of the investigated systems from the polymer to small oligomers allowed the use of accurate quantum chemical methods and dynamics approaches.

A tremendous effort has been devoted in the last decade to elucidate the excited-state deactivation mechanism of the building blocks DHI and DHICA and their oligomers, with most research focusing on DHICA. This is due to the fact, that the synthesis of DHI has proven rather challenging, as it tends to polymerize during the preparation. Although significant insight has been gained in the case of DHICA, the full deactivation mechanism is far from being understood, especially the role of intermolecular interactions between monomers and the role of the environment. This is even more severe for DHI, where only a few proposed deactivation pathways exist. A general simplistic depiction of the photoreaction of DHI is shown in Figure 1.2I., where the monomeric DHI is excited from the ground (Figure 1.2I.a) to the excited state (Figure 1.2I.b) from where it relaxes back to the ground state. The different results obtained from recent investigations on the nature of this deactivation are presented in the following.

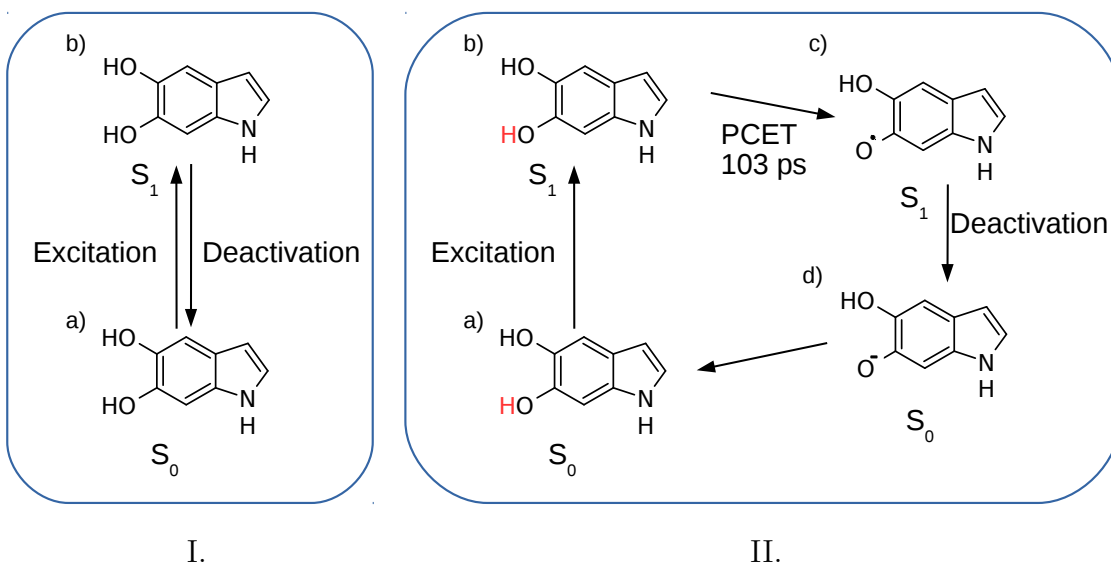


**Figure 1.2:** The left hand side (I.) represents the general reaction scheme, where a) DHI in the electronic ground state gets excited to the first excited state b). From there, DHI deactivates back to the ground state in the initial geometry. The right hand side (II.) presents the deactivation mechanism in solvent found in Reference 18, where a) and b) represent the same steps as in I.. From b) to c) a proton-coupled electron transfer to the solvent occurs which means that both an electron and a proton (marked in red in a) and b) ) are transferred from DHI to the solvent, resulting in species c). The deactivation from c) to d) was not observed in Reference 18 and has only been proposed.

Initial theoretical calculations in gas phase proposed that the DHI monomer decays by an intramolecular hydrogen atom transfer from one of the hydroxy groups to an aromatic carbon, which then tautomerizes to form 6-hydroxy-1,4-

dihydroindol-5-one.<sup>19</sup> Recent experimental measurements suggested three parallel excited-state decay mechanisms for DHI: a fast decay via formation of a radical cation and a solvated electron, intersystem crossing to the triplet state, and radiative decay via fluorescence to the ground state.<sup>2,20</sup> Additionally, long-lived excited-state species were observed in DHI polymers.<sup>21</sup> Current theoretical investigations found a deactivation pathway via elongation of the OH and NH bonds in gas phase.<sup>22</sup> Another current combined experimental and theoretical investigation resulted in a deactivation mechanism via a proton-coupled electron transfer (PCET) which is depicted in Figure 1.2II.<sup>18</sup> This latter work has shown that DHI dissipates its excited-state energy on a 100 ps timescale by a sequential PCET mechanism to the water (see Figure 1.2II.b and 1.2II.c). In this process, an electron is first transferred to the solvent in the form of a solvated electron while DHI is a cationic radical. Then a proton is transferred from DHI to the solvent forming a solvent cation, which completes the PCET. With the PCET completed, DHI is now a radical as it harbours one unpaired electron. This mechanism is in accordance with one of the deactivation mechanisms proposed by experimentalists earlier.<sup>2,20</sup> However, this mechanism is only known to the point where the PCET to the solvent has been completed in the first excited state (Figure 1.2II.c) and does not cover the actual relaxation to the ground state or other possible pathways. For the theoretical investigation of the interactions of DHI with the solvent, some solvent molecules were modeled explicitly to form small cluster systems with DHI which were then investigated using quantum chemistry. A solvent dependency of this deactivation mechanism was observed in the experiment between water and methanol.<sup>18</sup> The solvent dependency was reasoned with the height of the energy barrier of the proton transfer to the solvent in the PCET mechanism. This barrier was computed to be three times larger for methanol than for water in the corresponding cluster systems.<sup>18</sup>

### 1.3 Scope of this Thesis

The aim of this work is to investigate the different deactivation pathways accessible after the PCET proposed in Reference 18 has been completed (see Figure 1.2II.c), by performing excited state dynamics. Exploring the excited state dynamics following this initial PCET will reveal the different pathways available from these conformations and whether or not fast relaxation to the ground state is observed. Fast relaxation to the ground state would indicate that the main barrier in this deactivation channel has already be overcome by completing the PCET. Furthermore, dynamics simulations are perfectly suited to discern possibly different behaviors in different solvent clusters, here water and methanol.

## 2. Theory

This thesis investigates the electronic relaxation pathways of 5,6-dihydroxyindole (DHI) in solvent clusters. For this, an approach suitable to describe the evolution of the DHI-solvent clusters in time is needed, as well as a reliable method to calculate the excited states at every time step of the simulation. In the following chapter, the theoretical framework for the different electronic structure methods used throughout this work and the dynamic propagation model are presented.

### 2.1 The Schrödinger equation

The time-dependent Schrödinger equation gives the complete non-relativistic quantum mechanical description of a system.<sup>23,24</sup> In atomic units<sup>i</sup> it can be written as

$$i\frac{\partial}{\partial t}|\Psi(\vec{R}, \vec{r}, t)\rangle = \hat{H}(\vec{R}, \vec{r}, t)|\Psi(\vec{R}, \vec{r}, t)\rangle \quad (2.1)$$

where  $|\Psi(\vec{R}, \vec{r}, t)\rangle$  represents the time-dependent wavefunction. It depends on the position of all nuclei ( $\vec{R}$ ) and electrons ( $\vec{r}$ ), and the time ( $t$ ). The Hamilton operator  $\hat{H}(\vec{R}, \vec{r}, t)$  contains all particle-particle interactions. This equation contains both nuclear and electronic structure information. Unfortunately, since its first formulation in 1926, exact solutions to the Schrödinger equation can only be calculated for two particle systems like the hydrogen atom, therefore prohibiting the direct application of the Schrödinger equation to larger systems. In the following decades a high number of approximations to solve the Schrödinger equation have been proposed, with the most prominent one being the Born-Oppenheimer approximation.

### 2.2 The Born-Oppenheimer Approximation

The Born-Oppenheimer approximation<sup>25</sup> is based on the separation of the total wavefunction ( $|\Psi\rangle$ ) into a nuclear ( $|\Psi_{nu}\rangle$ ) and an electronic wavefunction

---

<sup>i</sup>If not stated otherwise, atomic units will be used throughout the theory part of this thesis

( $|\Psi_{el}\rangle$ ), which can then be calculated separately in the framework of this approximation. This can be most easily understood when starting from the time-independent Schrödinger equation which describes stationary systems using a time-independent Hamilton operator:

$$\hat{H}(\vec{R}, \vec{r})|\Psi(\vec{R}, \vec{r})\rangle = E_{tot}|\Psi(\vec{R}, \vec{r})\rangle \quad (2.2)$$

where the total energy of the system ( $E_{tot}$ ) is obtained as the eigenvalue of the now time-independent Hamilton operator. The Hamilton operator is composed of kinetic terms ( $\hat{T}$ ) for the particles and potential terms ( $\hat{V}$ ) between the particles. It can be written as

$$\hat{H}(\vec{R}, \vec{r}) = \hat{T}_{nu}(\vec{R}) + \hat{T}_{el}(\vec{r}) + \hat{V}_{nu,nu}(\vec{R}) + \hat{V}_{nu,el}(\vec{R}, \vec{r}) + \hat{V}_{el,el}(\vec{r}). \quad (2.3)$$

Here,  $\hat{T}_{nu}$  and  $\hat{T}_{el}$  are the nuclear and electronic kinetic operators,  $\hat{V}_{nu,nu}$  and  $\hat{V}_{el,el}$  describe the coulomb repulsion between particles of identical charge, and  $\hat{V}_{nu,el}$  the attraction between electrons and nuclei. When considering a molecule with  $n_{el}$  electrons and  $N_{nu}$  nuclei, the explicit contributions of the different terms can be written as

$$\hat{T}_{nu} = - \sum_{A=1}^{N_{nu}} \frac{1}{2M_A} \nabla_A^2 \quad (2.4)$$

$$\hat{T}_{el} = - \sum_{i=1}^{n_{el}} \frac{1}{2} \nabla_i^2 \quad (2.5)$$

$$\hat{V}_{nu,nu} = \sum_{A=1}^{N_{nu}} \sum_{B>A}^{N_{nu}} \frac{Z_A Z_B}{R_{AB}} \quad (2.6)$$

$$\hat{V}_{nu,el} = - \sum_{A=1}^{N_{nu}} \sum_{i=1}^{n_{el}} \frac{Z_A}{r_{Ai}} \quad (2.7)$$

$$\hat{V}_{el,el} = \sum_{i=1}^{n_{el}} \sum_{j>i}^{n_{el}} \frac{1}{r_{ij}} \quad (2.8)$$

with  $M_A$  and  $Z_A$  being the mass and the atomic number of the nuclei. The denominators  $R_{AB}$ ,  $r_{Ai}$  and  $r_{ij}$  represent the distance between two nuclei, one nucleus and one electron, and between two electrons, respectively. Starting from Eq 2.2 this, the Born-Oppenheimer approximation can be applied. In a first step, we separate the total wavefunction into a nuclear and an electronic part:

$$|\Psi(\vec{R}, \vec{r})\rangle = |\Psi_{nu}(\vec{R})\Psi_{el}(\vec{r}; \vec{R})\rangle \quad (2.9)$$

where we assume, that the movement of electrons occurs much faster than the movement of the nuclei. Therefore, the electronic wavefunction depends only

parametrically on the position of the nuclei ( $\bar{R}$ ), i.e. the nuclei are assumed to be static during the calculation of  $|\Psi_{el}\rangle$ . This renders the kinetic energy of the nuclei zero and the interaction between nuclei a constant. For the nuclei the opposite effect is observed: the electrons are assumed to move on such a short timescale that the nuclei are not subject to explicit electron-nucleus interactions but move in the average field of electrons instead. Rewriting Eq. 2.2 using  $|\Psi_{el}(\vec{r}; \bar{R})\rangle$  gives the time-independent Schrödinger equation in the framework of the Born-Oppenheimer approximation:

$$\hat{H}_{el}(\vec{r}; \bar{R})|\Psi_{el}(\vec{r}; \bar{R})\rangle = E_{el}|\Psi_{el}(\vec{r}; \bar{R})\rangle \quad (2.10)$$

with  $E_{el}$  being the electronic energy and  $\hat{H}_{el}(\vec{r}; \bar{R})$  being the electronic Hamilton operator which only contains the following terms:

$$\hat{H}_{el}(\vec{r}; \bar{R}) = \hat{T}_{el} + \hat{V}_{nu,el} + \hat{V}_{el,el}. \quad (2.11)$$

Eq. 2.10 results in a specific energy for a given nuclear geometry. Varying the nuclear conformations, calculating the corresponding electronic energies and adding the nucleus-nucleus repulsion, results in the so-called potential energy surface (PES)

$$E_{PES}(\bar{R}) = E_{el} + \sum_{A=1}^{N_{nu}} \sum_{B>A}^{N_{nu}} \frac{Z_A Z_B}{r_{AB}} \quad (2.12)$$

on which the nuclear wavefunction evolves according to the nuclear Schrödinger equation. Inserting the factorized wavefunction (Eq. 2.9) and the result obtained from solving the electronic Schrödinger equation (Eq. 2.10) into the time-independent Schrödinger equation (Eq. 2.2) leads to

$$E_{PES}|\Psi_{el}(\vec{r}; \bar{R})\Psi_{nu}(\vec{R})\rangle + \hat{T}_{nu}|\Psi_{el}(\vec{r}; \bar{R})\Psi_{nu}(\vec{R})\rangle = E_{tot}|\Psi_{el}(\vec{r}; \bar{R})\Psi_{nu}(\vec{R})\rangle \quad (2.13)$$

with

$$\begin{aligned} \hat{T}_{nu}|\Psi_{el}(\vec{r}; \bar{R})\Psi_{nu}(\vec{R})\rangle &= - \sum_{A=1}^{N_{nu}} \frac{1}{2M_A} \nabla_A^2 |\Psi_{el}(\vec{r}; \bar{R})\Psi_{nu}(\vec{R})\rangle \quad (2.14) \\ &= - \sum_{A=1}^{N_{nu}} \frac{1}{2M_A} [\nabla_A^2 |\Psi_{el}(\vec{r}; \bar{R})\rangle + 2\nabla_A |\Psi_{el}(\vec{r}; \bar{R})\rangle \nabla_A + |\Psi_{el}(\vec{r}; \bar{R})\rangle \nabla_A^2] |\Psi_{nu}(\vec{R})\rangle. \end{aligned} \quad (2.15)$$

The derivatives of the electronic wavefunction with respect to the nuclear wavefunction are called non-adiabatic couplings (NACs) and represent the couplings between different electronic states. In the framework of the Born-Oppenheimer approximation the NACs are neglected, i.e. the electronic wavefunction is assumed to be subject to only small changes with small changes of the nuclear

wavefunction. This assumption breaks down when two electronic states come close in energy, as the mixing of states leads to a strong change in the character of the electronic wavefunction with small differences in the geometry. Nevertheless, the Born-Oppenheimer approximation serves as a starting point for almost all types of electronic structure calculations, as the separation of the nuclear and electronic wavefunctions reduces the complexity of the Schrödinger equation drastically. Despite this, the calculation of the separated equations poses a serious problem and further approximations have to be introduced. The following section will deal with different electronic structure methods to approximate the electronic Schrödinger equation to obtain the PES.

## 2.3 Electronic Structure Methods

### 2.3.1 Hartree-Fock Approximation

One of the main obstacles in solving the electronic Schrödinger equation is the many-body nature of the electronic wavefunction. The main goal of the Hartree-Fock approximation (HF) therefore consists in describing the multi-electron wavefunction with the use of single-electron wavefunctions.<sup>26</sup> These one-electron wavefunctions ( $|\chi(\vec{\xi})\rangle$ ) are called spin orbitals which can be written as

$$|\chi_i(\vec{\xi}_i)\rangle = |\phi_i(\vec{r}_i)\rangle|\kappa(\xi)\rangle \quad (2.16)$$

where  $\vec{r}$  is the position of an electron,  $\phi$  a spatial orbital, and  $|\kappa(\xi)\rangle$  a spin function. Hence, two spin orbitals can differ in the spin component (spin up or spin down) while being identical in the coordinates of the electrons  $\vec{r}$  and therefore occupying the same spatial orbital. These spin orbitals are calculated as eigenfunctions of the one-electron operators. Initially, the total approximated wavefunction ( $|\Psi_{HF}\rangle$ ) was derived as a so-called Hartree product of the single-electron wavefunctions:

$$|\Psi_{HF}\rangle = \prod_{i=1}^{n_{el}} |\chi_i(\vec{\xi}_i)\rangle. \quad (2.17)$$

This ansatz neglects the Pauli exclusion principle which states that a wavefunction built up from fermions has to change its sign upon exchange of two fermions. Slater<sup>27</sup> proposed to denote the wavefunction as a determinant ( $\Phi$ ) which is antisymmetric upon exchange of two rows or columns:

$$|\Psi_{HF}\rangle = |\Phi_{HF}\rangle = \frac{1}{\sqrt{n_{el}!}} \begin{vmatrix} \chi_1(\vec{\xi}_1) & \chi_2(\vec{\xi}_1) & \cdots & \chi_{n_{el}}(\vec{\xi}_1) \\ \chi_1(\vec{\xi}_2) & \chi_2(\vec{\xi}_2) & \cdots & \chi_{n_{el}}(\vec{\xi}_2) \\ \vdots & \vdots & \ddots & \vdots \\ \chi_1(\vec{\xi}_{n_{el}}) & \chi_2(\vec{\xi}_{n_{el}}) & \cdots & \chi_{n_{el}}(\vec{\xi}_{n_{el}}) \end{vmatrix} \quad (2.18)$$

This approach proved itself to be an advantageous method to construct a many-body wavefunction out of single electron wavefunctions. Hence, these so-called Slater-determinants are found at the heart of many quantum chemical methods.

The Hartree-Fock equations can be obtained by inserting the Slater determinant (Eq. 2.18) in the electronic Schrödinger equation and applying the variational principle. The variational principle states that any wavefunction created by a method that obeys it yields an energy which is equal or greater than the energy obtained with the exact wavefunction. The HF equations therefore minimize the energy of each orbital to yield the best one-electron wavefunction possible. As the orbitals have to retain their orthonormality, this minimization with respect to the energy is conducted using Lagrange multipliers. The resulting equations then read as

$$\hat{f}(\vec{\xi}_1)|\chi_i(\vec{\xi}_1)\rangle = \epsilon_i|\chi_i(\vec{\xi}_1)\rangle \quad (2.19)$$

with

$$\hat{f} = \hat{h} + \sum_{j=1}^{n_{el}} (\hat{J}_j - \hat{K}_j) \quad (2.20)$$

where  $\hat{f}$  is the Fock operator,  $\hat{h}$  is the one-electron operator which contains  $\hat{T}_{el}$  and  $\hat{V}_{nu,el}$ , and  $\hat{J}$  and  $\hat{K}$  are the Coulomb and exchange operator, respectively, while  $\epsilon_i$  is an eigenvalue of the Fock operator.  $\hat{J}$  describes the classical repulsion between two charge distributions, while  $\hat{K}$  has no classical analogy but is a result of the antisymmetry condition. Inserting Eq. 2.20 into Eq. 2.19 gives three different terms:

$$\hat{h}(\vec{\xi}_1)|\chi_i(\vec{\xi}_1)\rangle = - \left( \frac{1}{2} \nabla_1^2 - \sum_{A=1}^{N_{nu}} \frac{Z_A}{r_{Ai}} \right) \chi_i(\vec{\xi}_1) \quad (2.21)$$

$$\hat{J}_j(\vec{\xi}_1)|\chi_i(\vec{\xi}_1)\rangle = \left\langle \chi_j(\vec{\xi}_2) \left| \frac{1}{r_{12}} \right| \chi_j(\vec{\xi}_2) \right\rangle |\chi_i(\vec{\xi}_1)\rangle \quad (2.22)$$

$$\hat{K}_j(\vec{\xi}_1)|\chi_i(\vec{\xi}_1)\rangle = \left\langle \chi_j(\vec{\xi}_2) \left| \frac{1}{r_{12}} \right| \chi_i(\vec{\xi}_2) \right\rangle |\chi_j(\vec{\xi}_1)\rangle \quad (2.23)$$

$$\cdot \quad (2.24)$$

The HF equations can be further simplified by discriminating between closed shell systems where every electron is paired and open shell systems. In the case of a closed shell systems, two paired electrons are assumed to always occupy the same spatial orbital and to only differ in their spin function. For simplicity, spatial orbitals will be used in the following sections.

The HF approximation represents a useful tool to construct the electronic ground state wavefunction of a system. A drawback of the HF equations is the description of the calculated orbitals. In theory, every spatial point with a non-zero probability to find an electron has to be calculated in theory or a grid is used

to approximate the wavefunction. To circumvent this problem, the single-electron wavefunctions are approximated using a set of known basis functions ( $\theta$ )

$$|\phi_i\rangle = \sum_{\alpha=1}^{M_b} c_{\alpha i} |\theta_\alpha\rangle \quad (2.25)$$

where  $c$  is a coefficient and  $M_b$  is the number of functions used to describe the orbital.<sup>28</sup> This linear combination of basis functions reduces the problem of finding the best orbitals to finding the best coefficients for the basis functions in the so-called Roothaan-Hall equations. The HF equations can be rearranged in matrix notation to represent an eigenvalue problem:

$$\mathbf{FC} = \mathbf{SC}\epsilon \quad (2.26)$$

where  $\mathbf{F}$  is the Fock matrix, containing the Fock operators,  $\mathbf{C}$  the matrix of coefficients,  $\mathbf{S}$  the matrix of overlaps between the basis functions, and  $\epsilon$  the matrix of orbital energies. When using the HF approach, one has to keep in mind that a direct solution of the whole set of HF equations is impossible as the Fock operators depend on the orbitals which are the unknown factor in this equation. This means, that the HF equations are solved in an iterative way, where every iteration step results in orbitals which give lower energies than the previous orbitals which in turn modify the Fock operators. Once no further change in the orbitals is observed upon a new iteration step, the calculation is deemed to have converged to the best possible solution given the current basis set. This whole iterative approach is termed self-consistent field (SCF) approach and is one of the main strengths of the HF method, as it is self-optimizing.

With a suitable choice of the basis set, ground state wavefunctions and energies can be calculated with reasonable accuracy. But even with an infinite number of basis functions, the exact energy is not obtained. The resulting error is systematic and caused by the use of a single Slater determinant and the mean-field approximation which does not account fully for the explicit interaction between two electrons. To correct for this error, various post-Hartree-Fock methods have been established.

### 2.3.2 Configuration Interaction

The Hartree-Fock method replaces the electron-electron repulsion by an average interaction (mean-field approximation), leading to an error. This error is the electron correlation energy ( $E_{corr}$ ), which is the difference between the Hartree-Fock energy ( $E_{HF}$ ) at the limit of a complete basis set and the exact electronic energy ( $E_{el}$ ).<sup>29</sup>

$$E_{corr} = E_{el} - E_{HF} \quad (2.27)$$

This correlation energy can be further separated into dynamic and static correlation. Dynamic correlation stems from the omittance of explicit and instantaneous

electron-electron interaction in the HF scheme, while static correlation is caused by using just a single Slater determinant, i.e. taking only one electronic configuration into account. To retrieve some or all of the missing correlation energy, different so-called post-Hartree-Fock methods have been established. An early proposed method which is able to fully incorporate electronic correlation is configuration interaction (CI).<sup>30</sup>

The CI method was designed to overcome the inherent limitation of the HF method of being based on just a single Slater determinant. This is achieved by assembling the total wavefunction as a linear combination of the ground state determinant ( $|\Phi_{HF}\rangle$ ) and all possible excited determinants ( $|\Phi_{ex}\rangle$ ). These excited determinants can be subdivided into singly, doubly, triply, etc., excited determinants relative to the ground state configuration. The CI wavefunction ( $|\Psi_{CI}\rangle$ ) then reads as

$$|\Psi_{CI}\rangle = a_0|\Phi_{HF}\rangle + \sum_S a_S|\Phi_S\rangle + \sum_D a_D|\Phi_D\rangle + \sum_T a_T|\Phi_T\rangle + \dots = \sum_{i=0} a_i|\Phi_i\rangle \quad (2.28)$$

where  $S$ ,  $D$ , and  $T$  are the single, double, and triple excitations, respectively, and  $a$  the CI expansion coefficients. Excited state determinants are obtained by replacing occupied orbitals in the HF calculation with unoccupied ones. Essentially this represents moving an electron from an occupied orbital to an unoccupied one without taking the influence of this excitation on the orbitals into account. In other words, the HF orbitals are not optimized during the CI procedure. Optimizing  $|\Psi_{CI}\rangle$  with respect to the energy results in a wavefunction based on multiple configurations which accounts fully for static and dynamic correlation if all possible determinants are used. To obtain the energy of the CI wavefunction ( $E_{CI}$ ), the following equation has to be solved:

$$E_{CI} = \langle \Psi_{CI} | \hat{H} | \Psi_{CI} \rangle = \sum_{i=0} \sum_{j=0} a_i a_j \langle \Phi_i | \hat{H} | \Phi_j \rangle, \quad (2.29)$$

which can be written as a  $nxn$  CI matrix where  $n$  is the number of determinants in this case. The matrix elements  $H_{ij}$  take the form

$$H_{ij} = \langle \Phi_i | \hat{H} | \Phi_j \rangle. \quad (2.30)$$

The number of elements that have to be calculated in the CI matrix can be drastically reduced by considering the nature of the used determinants: all determinants are comprised of orthonormal orbitals. Utilizing the fact, that the Hamilton operator only contains one- and two-electron operators, matrix elements will be zero if they differ in more than two orbitals. This is due to the fact that in these cases there will always be an integral of two different orbitals that will be zero due to the orthonormality. Hence, only matrix elements that differ in up to two orbitals have to be considered. The Slater-Condon rules<sup>27,31</sup> give

the exact number of non-zero integrals that have to be solved for each matrix element, representing a useful tool to facilitate the use of CI methods. Additionally, Brillouin’s theorem states that the matrix element between the HF determinant and any singly excited wavefunction has to be zero. The CI matrix can then be written as

$$\begin{array}{l}
 \langle \Phi_{HF} | \\
 \langle \Phi_S | \\
 \langle \Phi_D | \\
 \langle \Phi_T | \\
 \langle \Phi_Q | \\
 \vdots
 \end{array}
 \begin{pmatrix}
 | \Phi_{HF} \rangle & | \Phi_S \rangle & | \Phi_D \rangle & | \Phi_T \rangle & | \Phi_Q \rangle \\
 E_{HF} & 0 & x & 0 & 0 & \cdots \\
 0 & E_S & x & x & 0 & \cdots \\
 x & x & E_D & x & x & \cdots \\
 0 & x & x & E_T & x & \cdots \\
 0 & 0 & x & x & E_Q & \cdots \\
 \vdots & \vdots & \vdots & \vdots & \vdots & \ddots
 \end{pmatrix}
 \quad (2.31)$$

where  $x$  represents some non-zero value. Despite the enormous reduction in calculated integrals through the use of the Slater-Condon rules and Brillouin’s theorem, the immense growth of possible determinants with system size limits the use of CI with all determinants (full CI) to rather small molecules. Therefore, truncated CI methods are used, where excited determinants are only included up to a specific excitation order. When doing so, including only single excitations yields no improvement over the HF energy, as the matrix elements between those determinants are zero. An improvement in energy is only obtained when including at least doubly excited determinants in a CI doubles approach (CID). As the doubly excited determinants have non-zero matrix elements with the singly excited determinants, inclusion of those in a CID calculation (CISD, CI singles doubles) further improves the results. CISD accounts for a large part of the correlation energy and scales as  $M_b^6$ , giving a good compromise between accuracy and still being computationally affordable. However, restricting our CI expansion to a specific size introduces some errors.

One of the major drawbacks in using truncated CI methods is the lack of size consistency. A method is size consistent if the sum of the energies of two systems (A and B) equals the energy of both systems (A + B) at infinite separation. Assuming a CISD scheme, the highest order of occurring excitations are double excitations for the isolated systems. In the case of single helium atoms, CISD corresponds to full CI, recovering the complete electron correlation. However, in the case of two helium atoms at infinite separation, a four electron system is encountered which is described exactly only after inclusion of quadruply excited determinants. Hence, these energies differ due to the limitation to a specific excitation order of the determinants while the size of the considered electronic system increases.

The underlying principles of the CI form the foundation of multi-configurational self-consistent field methods (MCSCF), that are nowadays the most common ansatz to treat systems that are not well described using a single Slater determi-

nant, i.e., systems that contain large amounts of static correlation.

### 2.3.3 Multi-Configurational Self-Consistent Field

An alternative to truncated CI are multiconfigurational self-consistent field methods (MCSCF), which are also useful to describe excited states. As the name implies, the total wavefunction ( $|\Psi_{MCSCF}\rangle$ ) is comprised of multiple Slater determinants and can be written in an analogous manner as the equation for the CI wavefunction (compare Eq. 2.28):

$$|\Psi_{MCSCF}\rangle = \sum_{i=0} a_i |\Phi_i\rangle. \quad (2.32)$$

In the CI formulation, all Slater determinants are built using the initially calculated HF orbitals. These are not assumed to change when exchanging a former occupied orbital with an unoccupied one. Therefore, any form of orbital relaxation, i.e. adaption of the orbitals to the new configuration, is neglected. Contrary to the CI approach, the orbitals are allowed to relax in MCSCF methods. Hence, not only the coefficients of the determinants ( $a_i$ ) have to be optimized, but also the coefficients of every orbital ( $c_i$ ). This leads to more involved calculations for MCSCF wavefunctions when compared to their CI counterparts, disqualifying the former from including large amounts of determinants. Nevertheless, MCSCF wavefunctions already include a large part of the static correlation and represent qualitatively correct wavefunctions if enough determinants are included. This wavefunction can then be used in a method able to describe dynamic correlation to yield very accurate results.

#### State-Averaging MCSCF

CI and MCSCF can be used to calculate excited states, as they both inherently include excited determinants, which are able to describe excited state wavefunctions. When calculating excited states with these methods, every state would be optimized using its own set of  $c_i$  and  $a_i$  coefficients. This results in well optimized excited states, but the computed states will most likely not be orthogonal. This complicates any calculation of properties where two different states are coupled. To prevent this, state-average MCSCF (SA-MCSCF) methods optimize all states at the same time with respect to the averaged energy ( $E_{MCSCF}^{av}$ ) of all states using the same set of  $c_i$ , therefore guaranteeing orthogonality:

$$E_{MCSCF}^{av} = \sum_i^k w_i E_{MCSCF,i} = \sum_i^k w_i \langle \Psi_{MCSCF,i} | \hat{H} | \Psi_{MCSCF,i} \rangle \quad (2.33)$$

where  $k$  is the number of states and  $w_i$  is the weight of state  $i$  with

$$\sum_i^k w_i = 1. \quad (2.34)$$

The use of  $w_i$  allows for determining the influence a given state has on the shared set of orbitals.

## Complete Active Space Self-Consistent Field

One of the advantages of MCSCF methods is the flexibility in choosing which determinants are included in the calculation. Depending on the question at hand, the number of determinants that enter the calculation can be reduced, as their contribution to a specific problem may be negligible. At the same time this is also one of the weaknesses of MCSCF methods, as it can never be taken for granted that all important configurations are included. Therefore, different MCSCF approaches exist, that offer various selection schemes to gather the components of a MCSCF calculation. One of the most prominent methods is the complete active space self-consistent field (CASSCF) approach.<sup>32,33</sup>

In CASSCF the orbitals of the HF calculation are divided into active and inactive orbitals. The inactive ones retain their HF occupation value (either 2 or zero) while the active ones are used to generate a set of excited determinants that enter the calculation. This is done by performing a full CI within the subspace of active orbitals while keeping the inactive ones fixed. All determinants obtained in this way now enter Eq 2.32. This simplifies the problem of choosing the determinants to selecting the right orbitals. The chosen active space is commonly denoted as  $(n_{el}, n_{\phi})$ -CASSCF, where  $n_{\phi}$  is the number of orbitals. As a complete CI expansion is conducted in the active space, the size of the active space has to be limited to a small selection of orbitals. However, these orbitals should be able to describe the behavior of the system.

With the use of CASSCF we obtain a multi-configurational wavefunction that gives a qualitatively correct description of our system. We account for large parts of the static correlation but are missing the dynamical correlation. The method of choice to recover the missing correlation is perturbation theory.

### 2.3.4 Perturbation Theory

Perturbation theory represents a useful tool for approximating properties that cannot be accessed directly and is applied in many fields of physics. It is based on the assumption that the exact solution to a problem may be unknown, but a large part of the problem can be solved, reducing the unknown part to a small fraction of the initial system. The perturbation is expanded in a Taylor series to yield an improvement in accuracy over the unperturbed system that was known. In our case, the unperturbed system is defined by any approximated wavefunction we obtained. The perturbation that we cannot account for, is the missing correlation energy. This energy is rather small compared to the total energy we already know, hence, the requirements for using perturbation theory are met.

In the general case of applying perturbation theory to quantum mechanics, the Hamilton operator is split into a unperturbed Hamilton operator ( $\hat{H}_0$ ) and a perturbed one ( $\hat{H}'$ )

$$\hat{H} = \hat{H}_0 + \lambda \hat{H}' \quad (2.35)$$

with  $\lambda$  describing the strength of the perturbation. If  $\lambda$  equals zero, we are treating an unperturbed system. Increasing  $\lambda$  leads to continuous changes in the properties of our system. As we have a continuous change of our observables and only a small perturbation, we can expand our properties into a Taylor series:

$$\begin{aligned} E &= E^{(0)} + \lambda^1 E^{(1)} + \lambda^2 E^{(2)} + \lambda^3 E^{(3)} + \dots \\ |\Psi\rangle &= |\Psi^{(0)}\rangle + \lambda^1 |\Psi^{(1)}\rangle + \lambda^2 |\Psi^{(2)}\rangle + \lambda^3 |\Psi^{(3)}\rangle + \dots \end{aligned} \quad (2.36)$$

with the numbers in parenthesis indicating the order of the term. Inserting these expansions and Eq 2.35 into the time-independent Schrödinger equation (Eq. 2.2) gives

$$(\hat{H}_0 + \lambda \hat{H}')(|\Psi^{(0)}\rangle + \lambda^1 |\Psi^{(1)}\rangle + \dots) = (E^{(0)} + \lambda^1 E^{(1)} + \dots)(|\Psi^{(0)}\rangle + \lambda^1 |\Psi^{(1)}\rangle + \dots). \quad (2.37)$$

Terms of the same power of  $\lambda$  can then be separated to give

$$\begin{aligned} \lambda^0 : \hat{H}_0 |\Psi^{(0)}\rangle &= E^{(0)} |\Psi^{(0)}\rangle \\ \lambda^1 : \hat{H}_0 |\Psi^{(1)}\rangle + \hat{H}' |\Psi^{(0)}\rangle &= E^{(0)} |\Psi^{(1)}\rangle + E^{(1)} |\Psi^{(0)}\rangle \\ \lambda^2 : \hat{H}_0 |\Psi^{(2)}\rangle + \hat{H}' |\Psi^{(1)}\rangle &= E^{(0)} |\Psi^{(2)}\rangle + E^{(1)} |\Psi^{(1)}\rangle + E^{(2)} |\Psi^{(0)}\rangle \\ \lambda^n : \hat{H}_0 |\Psi^{(n)}\rangle + \hat{H}' |\Psi^{(n-1)}\rangle &= \sum_{i=0}^n E^{(i)} |\Psi^{(n-1)}\rangle. \end{aligned} \quad (2.38)$$

These are the zero-, first-, second- and  $n^{th}$ -order perturbation equations, respectively. The zero<sup>th</sup> order equation equals the Schrödinger equation of the unperturbed system and contains only known terms. The first-order equation contains two unknown quantities. Solving it for the first-order energy correction ( $E^{(1)}$ ) by projecting onto  $\langle \Psi^{(0)} |$  results in

$$\langle \Psi^{(0)} | \hat{H}' | \Psi^{(0)} \rangle = E^{(1)}. \quad (2.39)$$

Calculation of the second and higher order equations require the knowledge of the  $(n-1)^{th}$ -order wavefunctions. These can be expanded in the subspace of the  $(n-2)^{th}$ -order wavefunctions. In the case of the second-order equation,  $\Psi^{(1)}$  can be expanded in the subspace of the zero<sup>th</sup>-order wavefunctions:

$$|\Psi^{(1)}\rangle = \sum_i c_i |\Psi_i^{(0)}\rangle. \quad (2.40)$$

Solving the second-order equation for the coefficients gives

$$c_i = \frac{\langle \Psi_i^{(0)} | \hat{H}' | \Psi_0^{(0)} \rangle}{E_0^{(0)} - E_i^{(0)}} \quad (2.41)$$

which can now be used to obtain the second-order energy correction  $E^{(2)}$ :

$$E^{(2)} = \sum_{i \neq 0} \frac{\langle \Psi_0^{(0)} | \hat{H}' | \Psi_i^{(0)} \rangle \langle \Psi_i^{(0)} | \hat{H}' | \Psi_0^{(0)} \rangle}{E_0^{(0)} - E_i^{(0)}}. \quad (2.42)$$

Although use of lower order wavefunctions permits the calculation of even higher-order perturbation terms, terms that go beyond second-order are commonly omitted. This is due to decreasing contributions to the total energy when going to higher-order terms while computational cost increases. Furthermore, perturbational methods are not variational and do not necessarily give better results when more terms are considered.

Using the methodology derived in this section, we now have to define our known part of the calculation  $\hat{H}_0$  which is chosen to be a sum over Fock operators in Møller-Plesset perturbation theory.<sup>34</sup>

### Møller-Plesset Perturbation Theory

When defining our unperturbed Hamilton operator  $\hat{H}_0$  as a sum over Fock operators, we get

$$\hat{H}_0 = \sum_i^{n_{el}} \left( \hat{h}_i + \sum_j^{n_{el}} (\hat{J}_j - \hat{K}_j) \right). \quad (2.43)$$

The difference to the exact (electronic) Hamilton operator then equals the difference between the exact electron-electron interaction and the mean field approximation applied in HF where the latter is counted twice due to the double sum in Eq 2.43:

$$\hat{H}' = \hat{H} - \hat{H}_0 = \langle \hat{V}_{el,el} \rangle - 2\langle \hat{V}_{el,el} \rangle \quad (2.44)$$

where  $\langle \hat{V}_{el,el} \rangle$  represents the expectation value of  $\hat{V}_{el,el}$ . The zero<sup>th</sup> order energy ( $E(\text{MP0})$ ) can then be calculated to give

$$E(\text{MP0}) = E^{(0)} = \langle \Psi^{(0)} | \hat{H}_0 | \Psi^{(0)} \rangle = \left\langle \Psi^{(0)} \left| \sum_{i=1}^{n_{el}} \hat{f}_i \right| \Psi^{(0)} \right\rangle = \sum_{i=1}^{n_{el}} \epsilon_i. \quad (2.45)$$

Therefore our unperturbed energy is simply a sum over the HF orbital energies. This is a rather crude estimate, rendering  $E(\text{MP0})$  worse than the pure HF energy.

Inserting our definition of  $\hat{H}'$  into Eq 2.39 gives the first-order energy correction  $E^{(1)}$ :

$$E^{(1)} = \langle \Psi^{(0)} | \hat{H}' | \Psi^{(0)} \rangle = \langle \hat{V}_{el,el} \rangle - 2\langle \hat{V}_{el,el} \rangle = -\langle \hat{V}_{el,el} \rangle. \quad (2.46)$$

Applying this correction term to  $E(\text{MP0})$ , we obtain the first-order energy  $E(\text{MP1})$  which equals the HF energy as the correction term simply removes the double counting of the electron-electron interaction:

$$E(\text{MP1}) = E(\text{MP0}) + E^{(1)} = E_{HF} \quad (2.47)$$

Only after incorporation of second-order terms, electron correlation is taken into account. Using the relation in Eq 2.35 the numerators of the second-order energy correction equation (Eq 2.42) can now be written as

$$\langle \Psi_0^{(0)} | \hat{H}' | \Psi_i^{(0)} \rangle = \langle \Psi_0^{(0)} | \hat{H} | \Psi_i^{(0)} \rangle - \left\langle \Psi_0^{(0)} \left| \sum_j^{n_{el}} \hat{f}_j \right| \Psi_i^{(0)} \right\rangle \quad (2.48)$$

When constructing our zero<sup>th</sup>-order subspace using excited Slater determinants, this equation can be drastically simplified. Applying the Slater-Condon rules to the above equation gives non-zero terms only for the interaction between  $\langle \Psi_0^{(0)} |$  and doubly excited determinants. This was explained in Section 2.3.2 where the current equation corresponds to the first row of the matrix in Eq 2.31. The Møller-Plesset second-order energy correction therefore reads as

$$E^{(2)} = \sum_{i < j}^{\chi_{occ}} \sum_{a < b}^{\chi_{vir}} \frac{\langle \Phi_0 | \hat{H}' | \Phi_{ij}^{ab} \rangle \langle \Phi_{ij}^{ab} | \hat{H}' | \Phi_0 \rangle}{E_0^{(0)} - E_{ij}^{ab}} \quad (2.49)$$

where  $\chi_{occ}$  and  $\chi_{vir}$  are the number of occupied and virtual orbitals, respectively.  $\Phi_{ij}^{ab}$  denotes a doubly excited determinant where one electron has been promoted from the occupied orbitals  $\chi_i$  and  $\chi_j$  to the unoccupied orbitals  $\chi_a$  and  $\chi_b$ .  $E_{ij}^{ab}$  is the corresponding energy of this determinant.

The second-order energy correction accounts for large parts of the missing correlation energy and is commonly used as the highest perturbation order that is considered, as the increase in computational cost when going to higher orders of the perturbation renders these methods unfeasible for most cases.

## Complete Active Space Second-Order Perturbation Theory

As presented in Section 2.3.3, CASSCF wavefunctions are subject to a full CI expansion in the chosen active space. Therefore, any electron correlation that occurs inside this active space is accounted for. Any electron-electron interaction that occurs between the inactive space and the active space or in the inactive space alone, is not considered. Perturbation theory can be applied to recover some of this missing correlation. In the specific case of second-order perturbation theory on a CASSCF wavefunction, the corresponding method is termed complete active space second order perturbation theory (CASPT2).<sup>35,36</sup>

In CASPT2, a scheme similar to Møller-Plesset perturbation theory is employed, where the the Fock operators are projected onto the CASSCF reference

space to describe  $\hat{H}_0$ . Additionally, a so-called first-order interaction space (FOI) is defined, which includes all states that have non-zero matrix elements with the ground state reference. This FOI is then used to calculate the second-order energy correction according to Eq 2.49. When using CASPT2, care has to be taken as some states in the FOI are almost isoenergetic to the reference state. When calculating the contribution of these so-called intruder states, the denominator is reduced to a very small number, which in turn increases the contribution this state has to the total energy correction although the initial coupling between the states could be very weak. To circumvent this problem, various shifting techniques exist, like the level shift.<sup>37</sup> When using the level shift, a small shift value ( $l$ ) is added to the denominator of the second-order energy correction:

$$E^{(2)} = \sum_{i < j}^{\chi_{occ}} \sum_{a < b}^{\chi_{vir}} \frac{\langle \Phi_0 | \hat{H}' | \Phi_{ij}^{ab} \rangle \langle \Phi_{ij}^{ab} | \hat{H}' | \Phi_0 \rangle}{E_0^{(0)} - E_{ij}^{ab} + l}. \quad (2.50)$$

The influence of intruder states diminishes when using a sufficiently large level shift. It has to be kept in mind however, that setting a shift value influences all contributions to the second-order energy correction on a different footing.

When using a state-averaged function, multi-state CASPT2 (MS-CASPT2) can be used to overcome problems at CASSCF crossing points that would be encountered otherwise.<sup>38</sup> Here a multidimensional reference space is spanned by the state-averaged states that is then used to define an effective Hamilton operator, of a specific order to yield the corresponding energy correction.

### 2.3.5 Algebraic Diagrammatic Construction

The algebraic diagrammatic construction scheme of the polarization propagator owns its rather exotic name to the basic concepts of its formulation.<sup>39,40</sup> As the name implies, ADC is based upon the polarization propagator  $\Pi_{pq,rs}(t)$ , which describes the time evolution of the polarization in a many-electron system. In doing so, it inherently contains information on the excited states of the system.<sup>41</sup> To be able to use the properties included in the polarization propagator, it has to be converted from a time-dependent to a frequency-dependent representation  $\Pi_{pq,rs}(\omega)$ . In the Lehmann-representation it reads as

$$\Pi_{pq,rs}(\omega) = \sum_{n \neq 0} \frac{\langle \Psi_0 | \hat{\gamma}_q^\dagger \hat{\gamma}_p | \Psi_n \rangle \langle \Psi_n | \hat{\gamma}_r^\dagger \hat{\gamma}_s | \Psi_0 \rangle}{\omega + E_0^{n_{el}} - E_n^{n_{el}}} + \sum_{n \neq 0} \frac{\langle \Psi_0 | \hat{\gamma}_r^\dagger \hat{\gamma}_s | \Psi_n \rangle \langle \Psi_n | \hat{\gamma}_q^\dagger \hat{\gamma}_p | \Psi_0 \rangle}{-\omega + E_0^{n_{el}} - E_n^{n_{el}}}. \quad (2.51)$$

Here  $\Psi_0$  and  $\Psi_n$  are the electronic ground state and excited state wavefunctions, respectively, with the corresponding energies  $E_0^{n_{el}}$  and  $E_n^{n_{el}}$ .  $\hat{\gamma}_q$  and  $\hat{\gamma}_p^\dagger$  are the creation and annihilation operators that add or remove an electron from a corresponding one-electron wavefunction, hence creating excited wavefunctions. Here it can be seen that the excitation energies of the excited states are found as poles

in this representation of the polarization propagator, where  $\omega = E_0^{n_{el}} - E_n^{n_{el}}$ . Denoting the polarization propagator in more compact matrix notation gives

$$\mathbf{\Pi}(\omega) = \mathbf{\Pi}^+(\omega) - \mathbf{\Pi}^-(\omega). \quad (2.52)$$

where  $\mathbf{\Pi}^+(\omega)$  and  $\mathbf{\Pi}^-(\omega)$  are the left and the right sum of the right-hand side of Eq 2.51, respectively. Both sums contain identical information, hence it is sufficient to focus on  $\mathbf{\Pi}^+(\omega)$ . The corresponding matrix equation can be written as

$$\mathbf{\Pi}^+(\omega) = \mathbf{x}^\dagger(\omega\mathbf{1} - \mathbf{\Omega})^{-1}\mathbf{x} \quad (2.53)$$

with the matrix elements

$$x_{n,rs} = \langle \Psi_n | \hat{\gamma}_r^\dagger \hat{\gamma}_s | \Psi_0 \rangle \quad (2.54)$$

$$\Omega_{nm} = -(E_0^{n_{el}} - E_n^{n_{el}})\delta_{nm}. \quad (2.55)$$

Therefore, the elements of  $\mathbf{x}$  represent the transition amplitudes while  $\mathbf{\Omega}$  represents a diagonal matrix containing all excitation energies. However, to obtain the excitation energies, one still needs to solve Eq 2.55, which in turn needs the energy of the excited state to be known and therefore cannot be solved directly. To be able to circumvent this problem, the diagonal excitation energy matrix is transformed into a non-diagonal form via unitary transformation using a transformation matrix  $\mathbf{Y}$ :

$$\mathbf{1} = \mathbf{Y}\mathbf{Y}^\dagger \quad (2.56)$$

$$\mathbf{M} = \mathbf{Y}\mathbf{\Omega}$$

$$\mathbf{f} = \mathbf{Y}\mathbf{x}$$

which results in

$$\mathbf{\Pi}^+(\omega) = \mathbf{f}^\dagger(\omega\mathbf{1} - \mathbf{M})^{-1}\mathbf{f}. \quad (2.57)$$

Using this transformation,  $\mathbf{M}$  is a non-diagonal representation of an effective Hamilton operator. As such,  $\mathbf{M}$  and  $\mathbf{f}$  can be expanded in a perturbational series similar to the procedure presented in Section 2.3.4 to give

$$\mathbf{M} = \mathbf{M}^{(0)} + \mathbf{M}^{(1)} + \mathbf{M}^{(2)} + \dots \quad (2.58)$$

$$\mathbf{f} = \mathbf{f}^{(0)} + \mathbf{f}^{(1)} + \mathbf{f}^{(2)} + \dots$$

Collecting terms of similar order results in  $\mathbf{\Pi}^+(\omega)$ s of different order:

$$\mathbf{\Pi}^+(\omega) = \mathbf{\Pi}^+(\omega)^{(0)} + \mathbf{\Pi}^+(\omega)^{(1)} + \dots \quad (2.59)$$

with the first two terms being

$$\begin{aligned} \mathbf{\Pi}^+(\omega)^{(0)} &= \mathbf{f}^{(0)\dagger}(\omega\mathbf{1} - \mathbf{M}^{(0)})^{-1}\mathbf{f}^{(0)} \\ \mathbf{\Pi}^+(\omega)^{(1)} &= \mathbf{f}^{(1)\dagger}(\omega\mathbf{1} - \mathbf{M}^{(0)})^{-1}\mathbf{f}^{(0)} + \mathbf{f}^{(0)\dagger}(\omega\mathbf{1} - \mathbf{M}^{(0)})^{-1}\mathbf{f}^{(1)} \\ &\quad + \mathbf{f}^{(0)\dagger}(\omega\mathbf{1} - \mathbf{M}^{(0)})^{-1}\mathbf{M}^{(1)}(\omega\mathbf{1} - \mathbf{M}^{(0)})^{-1}\mathbf{f}^{(0)}. \end{aligned} \quad (2.60)$$

Comparing these equations with Feynman diagrams and their corresponding representations yields algebraic descriptions for  $\mathbf{f}^{(n)}$  and  $\mathbf{M}^{(n)}$  that allow for the calculation of these elements. The use of Feynman-diagrams to overcome this final obstacle in the calculation resulted in the rather misleading name of ADC. Now being able to calculate both  $\mathbf{M}$  and  $\mathbf{f}$ , the excitation energies can be obtained by re-diagonalizing  $\mathbf{M}$ .

Different ADC schemes exist that differ in their order of considered perturbation terms. They are generally denoted as ADC( $n$ ) where  $n$  is the highest-order term that is calculated. ADC(2) is nowadays the most commonly used approach due to its favorable scaling of  $\mathcal{O}(n_{el}^5)$  although ADC(3) has recently been implemented in some widely distributed quantum chemical programs.

### 2.3.6 Density Functional Theory

The Schrödinger equation relies on the wavefunction to obtain atomic or molecular properties through the use of suitable operators. The wavefunction however, is itself a very elusive property and has to be generated using approximate methods as discussed in previous sections. Furthermore, it lacks a direct experimentally quantifiable observable and only the square of the wavefunction, the probability density, can be measured. Therefore, a frantic search for quantities was conducted that could be used as substitutions for the wavefunction, aimed at providing a physical observable capable of being used in the calculation of molecular properties. This search resulted in the foundation of density functional theory (DFT), which is unsurprisingly based on the electronic density  $\rho(\vec{r})$  of a system. The electronic density is simply the integral over the probability density:

$$\rho(\vec{r}) = \int |\Psi(\vec{r}_1, \vec{r}_2, \dots, \vec{r}_{n_{el}})|^2 d\vec{r}_1 \dots d\vec{r}_{n_{el}}. \quad (2.61)$$

X-ray experiments directly measure the electronic density, which is a three-dimensional property. It includes information about the position of all electrons and can therefore be used to express any operator which depends on the position of the nuclei as a functional of the electron density. As the energy of the electronic Schrödinger equation is based on the position of the electrons, it can be represented as a functional of  $\rho(\vec{r})$ :

$$E = E[\rho(\vec{r})] = T_{el}[\rho(\vec{r})] + V_{nu,el}[\rho(\vec{r})] + V_{el,el}[\rho(\vec{r})] \quad (2.62)$$

where the notation in square brackets represents functionals of the electron density and  $T_{el}$ ,  $V_{nu,el}$ , and  $V_{el,el}$  represent the functionals of the corresponding operators.

### Hohenberg-Kohn Theorems

The theoretical framework of all molecular DFT methods was provided in the Hohenberg-Kohn (HK) theorems.<sup>42</sup> The first HK theorem postulates that the

electronic density of the ground state is uniquely defined by an external potential, which is simply the potential the electrons experience in the presence of the nuclei. Every electron density is therefore related to a specific energy and other specific molecular properties. The second HK theorem states that DFT is subject to the variational principle. Therefore, DFT calculations can be systematically improved by finding the electron density that minimizes the energy. However, this only holds in the case the exact energy functional ( $E[\rho(\vec{r})]$ ), as will be explained in the next section.

One of the main advantages of DFT lies in the reduction of coordinates compared to wavefunction-based methods:  $\rho(\vec{r})$  depends only on three coordinates while the wavefunction depends on  $4n_{el}$  coordinates. However, current implementations of such orbital-free approaches suffer from inaccurate kinetic energy density functionals.<sup>43</sup> The most widely used DFT approaches are therefore based on the orbital-ansatz introduced by Kohn and Sham (KS)<sup>44</sup> where the dependency on  $3n_{el}$  coordinates re-emerges.

### Kohn-Sham Approach

As mentioned above, the kinetic energy functional has only approximate formulations in orbital-free methods. In the KS approach, the kinetic-energy operator is split into two terms: one of them is known exactly while the other is unknown. To be able to calculate the exact part of the kinetic energy, all electrons are treated as non-interacting particles in the Kohn-Sham approach. This leads to a system that closely resembles the HF method, as the Hamilton operator can then be denoted as a sum of one-electron operators with molecular orbitals as eigenfunctions. To account for the non-interacting nature of the system, an external potential ( $v_{KS}(\vec{r})$ ) is chosen in such a way that the electrons behave like interacting ones. The resulting one-electron KS equations yield the corresponding KS orbitals  $|\phi^{KS}\rangle$

$$\epsilon_i |\phi_i^{KS}(\vec{r})\rangle = \left[ -\nabla_i^2 \frac{1}{2} + v_{KS}(\vec{r}) \right] |\phi_i^{KS}(\vec{r})\rangle \quad (2.63)$$

with

$$v_{KS}(\vec{r}) = v_{ex}(\vec{r}) + v_{HF}(\vec{r}) + v_{xc}(\vec{r}) \quad (2.64)$$

where  $v_{KS}(\vec{r})$  is the KS potential and  $v_{HF}(\vec{r})$  represents the classical electron-electron repulsion.  $v_{xc}(\vec{r})$  is the exchange-correlation term containing the unknown kinetic energy term as well as potential correlation and exchange energy. The exact exchange-correlation functional ( $E_{xc}[\rho(\vec{r})]$ ) that defines  $v_{xc}(\vec{r})$  is unknown and has to be approximated. Throughout decades no functional was found that performs reasonable well in all cases. Hence, various classes of approximation schemes exist to derive the exchange-correlation functional. Most of these classes contain many different functionals and careful testing of different functionals precedes most applications of DFT in computational chemistry. As  $E_{xc}[\rho(\vec{r})]$  is

only approximated, the total energy functional is also only approximated, which prohibits the use of the variational principle.

With a good choice of a correlation-exchange functional, the non-degenerate ground state energy and other properties of a system can be calculated using DFT. However, the nature of the current thesis necessitates the ability to calculate excited states, which is not possible in the basic DFT method. Fortunately, Runge and Gross set the cornerstone for the incorporation of excited state calculations into the DFT framework in their formulation of time-dependent DFT (TDDFT).<sup>45</sup>

### Time-Dependent Density Functional Theory

To be able to formulate a time-dependent DFT method, the pillars of DFT have to be proven to have time-dependent counterparts.<sup>46</sup> This was shown to be the case by Runge and Gross, who first derived a unique relation between the time-dependent electronic density ( $\rho(\vec{r}, t)$ ) as well as the applicability of the variational principle in the time-dependent case.

With the two HK theorems proven for the time-dependent case, a similar approach as in DFT can be chosen to calculate all properties of interest. By assuming non-interacting electrons and defining time-dependent Kohn-Sham orbitals, the same methodology as in ground state DFT can be employed. The one-electron KS equations are based on the time-dependent Schrödinger equation and contain explicit time-dependence.

$$i \frac{\partial}{\partial t} |\phi_i^{KS}(\vec{r}, t)\rangle = \left[ -\nabla_i^2 \frac{1}{2} + v_{KS}(\vec{r}, t) \right] |\phi_i^{KS}(\vec{r}, t)\rangle \quad (2.65)$$

with

$$v_{KS}(\vec{r}, t) = v_{ex}(\vec{r}, t) + v_{HF}(\vec{r}, t) + v_{xc}(\vec{r}, t). \quad (2.66)$$

Similar as in regular DFT, TDDFT suffers from not knowing the exact exchange-correlation functional. The methodological closeness of both DFT and TDDFT allows for the use of DFT-derived exchange-correlation functionals in TDDFT, negating the need to develop completely new sets of functionals to approximate the time-dependent exchange-correlation functional.

Knowledge of the time-dependent electron density permits the use of linear response theory to obtain excited state properties. For this, the response of the system to an externally applied perturbation is calculated. Similar to the procedure in Section 2.3.4, the KS Hamilton operator is split into an unperturbed part and a perturbed one which is considered small. Expanding the perturbation in a Taylor series and cutting the terms after the first order gives the linear response of a system. In the case of TDDFT, the linear response can be calculated by expressing the response-dependent changes in the KS-Hamilton operator using the first-order perturbed density matrix. After some reformulation, one obtains

the following matrix equation:

$$\begin{bmatrix} \mathbf{A} & \mathbf{B} \\ \mathbf{B}^* & \mathbf{A}^* \end{bmatrix} \begin{bmatrix} \vec{X} \\ \vec{Y} \end{bmatrix} = \begin{bmatrix} 1 & 0 \\ 0 & -1 \end{bmatrix} \begin{bmatrix} \vec{X} \\ \vec{Y} \end{bmatrix} \iota \quad (2.67)$$

where  $\iota$  is the eigenvalue of the second matrix on both sides of the equation.  $\vec{X}$  and  $\vec{Y}$  represent perturbation densities, and the matrix elements of  $\mathbf{A}$  and  $\mathbf{B}$  can be written in Dirac notation as

$$\begin{aligned} A_{ia,jb} &= \delta_{ij} \delta_{ab} (\epsilon_a - \epsilon_i) + \langle ij|ab \rangle + \langle ij|f_{xc}|ab \rangle \\ B_{ia,jb} &= \langle ib|aj \rangle + \langle ib|f_{xc}|aj \rangle \end{aligned} \quad (2.68)$$

where  $f_{xc}$  is the exchange-correlation kernel, which is the derivative of the external potential with respect to the time-dependent density.  $\delta_{ab}$  is the Kronecker delta.

Using TDDFT, excited state properties can be obtained at a computationally rather low cost. However, the approximate nature of the available exchange-correlation functionals represents one of the main disadvantages of TDDFT. Other drawbacks include the poor description of charge-transfer or exclusion of doubly excited states. Therefore, no equal description of all classes of excited states is achievable when using TDDFT.

## 2.4 Surface Hopping Dynamics

Different methods were presented in the previous sections that are able to approximate ground and excited state properties of the electronic wavefunction. However, as discussed in Section 2.2, the nuclear part of the total wavefunction which is needed to compute the desired evolution of the system in time is still unknown. The nuclear wavefunction represents a distribution of the position of the nuclei that move along the PES. Calculating the movement of such a disperse wave according to the Schrödinger equation is computationally not feasible without introducing further approximations. In applying different approximations schemes, two ways of treating the nuclear wavefunction emerge: either it is described using gaussian functions that move along the PES or as a single point in phase space that resembles a specific molecular geometry instead of a probability distribution. When treating the nuclei as a wave and propagating this wave according to the time-dependent Schrödinger equation, a quantum dynamics approach is used. In quantum dynamics all information about the dynamics can be obtained by doing a single simulation, as the so-called wavepacket of the nuclei can split and explores all relevant parts of the phase space that can be reached during the simulation time. Considering excited state dynamics, this means that the wavepacket splits at a crossing point between states where the total population of the two wavepackets is determined by the transition amplitude at the

crossing point. This behavior is lost when treating the nuclei classically. In applying this classical model to the nuclei and reducing the distribution of geometries to a single one, the possibility to split at a crossing point is forfeited for the sake of computational efficiency. In the aforementioned case of excited state dynamics, this means that a single dynamics simulation can only be carried out in one state at a given time step, so no division at the crossing point is possible, forcing the simulation to choose which state to be in based on the transition probability. To account for the ability of the real nuclear dynamics in the latter methods, multiple dynamics simulations are conducted where each of these so-called trajectories now traverses different parts of the phase space. When a crossing point is encountered it is stochastically determined in which state each trajectory ends up. Hence, given enough trajectories the ratio of trajectories in different states after the crossing point equals the statistical probability to switch the state at the crossing point. An approach employing such a scheme is surface hopping.<sup>47</sup> In surface hopping, trajectories are propagated along a adiabatic PES and the probability to switch from one state to another is determined by the NACs between those two states. Different approaches to surface hopping exist and the method used throughout this thesis is the surface hopping algorithm as implemented into the surface hopping including arbitrary couplings (SHARC) method.<sup>48–50</sup>

### 2.4.1 Propagation of the Nuclei and the Electronic Wavefunction

In the SHARC method, the movement of the classical nuclei in time is given by Newton’s second law of motion:

$$M_A \frac{d}{dt^2} \vec{R}_A(t) = -\nabla_A E_\beta(\vec{R}_A(t)) \quad (2.69)$$

where  $\beta$  is the current electronic state of the trajectory and  $-\nabla_A E_\beta(\vec{R}_A(t))$  the gradient the nuclei are subject to in this state. Actual propagation of the nuclei is calculated employing the velocity-Verlet<sup>51</sup> algorithm:

$$\begin{aligned} \vec{R}_A(t + \Delta t) &= \vec{R}(t)_A + \vec{v}_A(t)\Delta t + \frac{\Delta t^2}{2}\vec{a}_A(t) \\ \vec{v}_A(t + \Delta t) &= \vec{v}_A(t) + \frac{\Delta t}{2}(\vec{a}_A(t) + \vec{a}_A(t + \Delta t)) \\ \vec{a}_A(t + \Delta t) &= -\frac{1}{M_A}\nabla_A E_\beta(\vec{R}_A(t + \Delta t)) \end{aligned} \quad (2.70)$$

where  $\vec{v}_A$  and  $\vec{a}_A$  are the velocity and acceleration of nucleus  $A$  respectively. Here it can be seen that the acceleration at the new time step ( $t + \Delta t$ ) can be obtained using the gradient of the current time step. From the acceleration both the new velocity and the new position can be calculated in turn.

To be able to describe the selection of the active state in which the classical trajectory is propagated, the time-evolution of the electronic wavefunction needs to be known. Thus the electronic time-dependent wavefunction is expanded using a sum of electronic states that satisfy the completeness relation:<sup>ii</sup>

$$|\Psi\rangle = \sum_{\alpha} |\psi_{\alpha}\rangle \langle \psi_{\alpha} | \Psi \rangle \quad (2.71)$$

where  $\psi$  represents electronic states. Inserting this equality into the the time-dependent Schrödinger equation (Eq 2.1) and projecting onto  $\langle \psi_{\beta} |$  one obtains

$$i \sum_{\alpha} \left( \langle \psi_{\beta} | \frac{d}{dt} |\psi_{\alpha}\rangle \langle \psi_{\alpha} | \Psi \rangle + \langle \psi_{\beta} | \psi_{\alpha} \rangle \frac{d}{dt} \langle \psi_{\alpha} | \Psi \rangle \right) = \sum_{\alpha} \langle \psi_{\beta} | \hat{H}_{el} | \psi_{\alpha} \rangle \langle \psi_{\alpha} | \Psi \rangle. \quad (2.72)$$

Utilizing the orthonormality of  $\psi_{\alpha}$  and  $\psi_{\beta}$  gives

$$\frac{d}{dt} \langle \psi_{\beta} | \Psi \rangle = - \sum_{\alpha} \left( i \langle \psi_{\beta} | \hat{H}_{el} | \psi_{\alpha} \rangle + \langle \psi_{\beta} | \frac{d}{dt} | \psi_{\alpha} \rangle \right) \langle \psi_{\alpha} | \Psi \rangle. \quad (2.73)$$

Collecting all terms of the previous equation into matrices and vectors gives

$$\frac{d}{dt} \vec{c} = -(i\mathbf{H} + \mathbf{T})\vec{c} \quad (2.74)$$

where  $\vec{c}$  is a vector of the coefficients of the wavefunction that contains the overlap between all  $\langle \psi |$  and  $|\Psi\rangle$ ,  $\mathbf{H}$  all elements of the form  $\langle \psi_{\beta} | \hat{H}_{el} | \psi_{\alpha} \rangle$  and  $\mathbf{T}$  the remaining  $\langle \psi_{\beta} | \frac{d}{dt} | \psi_{\alpha} \rangle$  terms that include the NACs. The propagation of the electronic wavefunction equals the propagation of  $\vec{c}$ . In SHARC this is done by integrating Eq 2.74 for the time step  $\Delta t$  which can also be an interpolated time step:

$$\vec{c}(t + \Delta t) = e^{-(i\mathbf{H} + \mathbf{T})\Delta t} \vec{c}. \quad (2.75)$$

The solutions of the previous equation can be collected in a so-called propagator matrix  $\mathbf{P}$  that propagates the  $\vec{c}(t)$  to  $\vec{c}(t + \Delta t)$ . In the adiabatic picture of the Born-Oppenheimer approximation,  $\mathbf{H}$  is diagonal, which simplifies Eq 2.75. However, inclusion of perturbational terms that represent additional couplings like couplings with laser fields or spin-orbit couplings results in off-diagonal elements in  $\mathbf{H}$ . In SHARC,  $\mathbf{H}$  is diagonalized using a unitary transformation to give  $\mathbf{H}^{diag}$ . This representation is then used to describe the electronic states of interest. These diagonal states can then be propagated by extending the unitary transformation to the propagator matrix to yield  $\mathbf{P}^{diag}$ .

---

<sup>ii</sup>The dependencies of the electronic wavefunction are dropped in the following for simplicity

## 2.4.2 Hopping Probabilities

Being now armed with a way to propagate both the electronic wavefunction as well as the position of the nuclei, the last part missing to perform surface hopping dynamics are the hopping probabilities. Most surface hopping algorithms are currently based on Tully's fewest switches criterion.<sup>52</sup> Due to the diagonalization in the SHARC methodology, a different expression of the same criterion has to be applied to avoid inconsistencies that arise due to the transformation. Using the diagonalized coefficient vector  $\vec{c}^{diag}$  and the diagonal propagator matrix  $\mathbf{P}^{diag}$  the probability to hop from the active state  $\beta$  to another state  $\alpha$  ( $h_{\beta \rightarrow \alpha}^{diag}$ ) is given by:

$$h_{\beta \rightarrow \alpha}^{diag} = \left( 1 - \frac{|c_{\beta}^{diag}(t + \Delta t)|^2}{|c_{\beta}^{diag}(t)|^2} \right) \frac{Re \left[ c_{\alpha}^{diag}(t + \Delta t) \left( P_{\alpha\beta}^{diag} \right)^* \left( c_{\beta}^{diag}(t) \right)^* \right]}{|c_{\beta}^{diag}(t)|^2 - Re \left[ c_{\beta}^{diag}(t + \Delta t) \left( P_{\beta\beta}^{diag} \right)^* \left( c_{\beta}^{diag}(t) \right)^* \right]} \quad (2.76)$$

where  $Re$  represents the real part of the subsequent expression. Additionally,  $h_{\beta \rightarrow \beta}^{diag}$  is set to zero as  $h_{\beta \rightarrow \alpha}^{diag}$  if the hopping probability is negative.

Combining the hopping probability with the propagation of our trajectory, surface hopping dynamics can now be conducted. Nevertheless, a set of suitable starting conditions has to be provided to give a qualitative picture of the surpassed PES. This necessity arises due to the neglect of the quantum nature of the nuclei as was discussed above and the need of initial geometries and momenta to initiate the dynamics. A prominent method to obtain a representative set of initial conditions is Wigner distribution sampling.

## 2.4.3 Wigner Sampling

The basic idea of the Wigner distribution<sup>53,54</sup> consists in deriving an expression, which gives a statistical description of the atomic coordinates and corresponding momenta for a quantum system. Formulation of such an equation is possible in phase space in the form of a Wigner distribution  $F_W(x, p)$ . It can be written based on uncoupled harmonic oscillators of the normal modes of the system at hand:

$$F_W(x, p) = \frac{1}{(\pi\hbar)^{3N_{nu}-6}} \prod_i^{3N_{nu}-6} \exp\left(-\frac{2\mu_i\eta_i x_i^2}{\hbar}\right) \exp\left(-\frac{2p_i^2}{\hbar\mu_i\eta_i}\right) \quad (2.77)$$

where  $i$  runs over all normal modes,  $x_i$ ,  $p_i$ ,  $\mu_i$ , and  $\eta_i$  are the corresponding coordinates, momentum, reduced mass, and angular frequency, respectively.

These probabilities can now be used to construct a set of initial conditions for a system based on the normal modes as obtained from a frequency calculation. Starting from the energetically minimized geometry, all calculated normal modes

are assigned a random number for a displacement in momentum and in phase space along the normal modes. The corresponding Wigner probability is then cross-checked for each normal mode with a random number to decide if these numbers should be kept. Repeating this process  $n$  times results in  $n$  geometries and corresponding velocities that are chosen based upon their probability in phase space. Using a sufficiently large  $n$ , a representative sampling is obtained.

## 3. Results and Discussion

In this section, the results and the way they were obtained is presented. As a first step, the initial system and its important features are discussed. Next, different methods are benchmarked to come up with the most suitable methods for the following non-adiabatic molecular dynamics simulations. The resulting dynamics obtained with the chosen methods is then presented where and the deactivation mechanisms are discussed paying attention to the differences observed with different solvents.

### 3.1 Cluster Systems

This thesis is dedicated to gain new insights into the excited state dynamics of DHI, a main building block of eumelanin. As already discussed in Section 1.2, the excited state deactivation mechanism for DHI<sup>2,18-20,22</sup> is incomplete despite recent investigations that provided numerous clues on the photodynamics of DHI. To shed some light upon this complicated picture, this work tries to complete the relaxation pathway proposed by Nogueira *et al.*<sup>18</sup> In their work, a rearrangement of solvent molecules after excitation to the first excited state was predicted using quantum chemical calculations. A solvated electron is subsequently formed which is stabilized by the new arrangement of solvent molecules. This electron transfer to the solvent is followed by a proton transfer from DHI to the solvent. After completing this proton transfer, the  $S_0$ - $S_1$  energy gap was found to reduce from almost 4 eV in the initial system to 0.5 eV. Therefore, it was concluded that the deactivation mechanism of DHI in solvent follows a proton-coupled electron transfer (PCET) mechanism. However, the investigation of the excited state dynamics after the transfer of both the electron and the proton to the solvent was not resolved. It is therefore the main goal of this thesis to explore the excited state behavior that follows this PCET mechanism.

In the work of Nogueira *et al.*<sup>18</sup> two different solvents were considered: water ( $H_2O$ ) and methanol (MeOH). Solvent effects were simulated using a microsolvation approach where the solute is surrounded by some solvent molecules in a solute-solvent cluster. The  $H_2O$  and the MeOH clusters of Reference 18 serve as a starting point for the dynamics simulations conducted in this work. Therefore, it is the intention of the following section to explain these cluster systems and

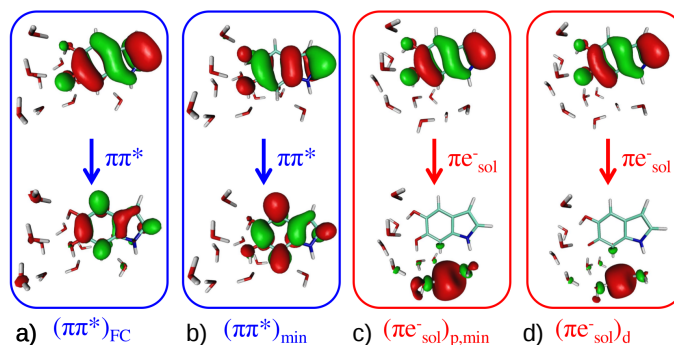


**Figure 3.1:** Key structures and orbitals involved in the deactivation mechanism obtained in Reference 18 for the H<sub>2</sub>O-DHI cluster. The two orbitals of the main contributing configuration are printed atop each step of the pathway. Panel a) shows the first excited state which is of  $\pi\pi^*$  character at the Franck-Condon geometry. Panel b) shows the minimum energy structure in the first excited  $\pi\pi^*$  state. Panel c) depicts the minimum energy geometry of the  $S_1$  with  $\pi\sigma$  character where the proton still is attached to DHI. d) the first excited state after proton transfer from DHI to the solvent. The Figure was adapted from Reference 18.

how they were obtained in Reference 18.

Both, the water and the methanol cluster systems were obtained using the same procedure: First, QM/MM molecular dynamics simulations were conducted including DHI in thousands of solvent molecules. The snapshot with the lowest potential energy was taken from the corresponding trajectory and classically minimized. From this optimized snapshot, all solvent molecules within a sphere of 2.5 Å radius from DHI were kept to form the microsolvation cluster while all other solvent molecules were discarded. The two resulting clusters differ in the number of solvent molecules: the MeOH-DHI cluster includes 6 solvent molecules while the H<sub>2</sub>O-DHI cluster incorporates 10 solvent molecules. The first excited state in these initial cluster systems is of  $\pi\pi^*$  character. The orbitals contributing to this excitation at the water cluster are shown in Figure 3.1a. The geometries of both clusters were then optimized in the first excited state, providing the geometry and contributing orbitals depicted in Figure 3.1b. The level of theory used for this optimization was CAM-B3LYP<sup>55</sup>/cc-pVDZ.<sup>56</sup> Starting from this  $\pi\pi^*$  minimum, the H atom of one of the two OH groups of DHI was manually attached to the closest hydrogen-bonding solvent molecule. Upon re-optimization at the same level of theory while keeping the transferred hydrogen atom attached, a large rearrangement of solvent molecules occurred in both cluster systems. This process was accompanied by a change of the character of the first excited state from a  $\pi\pi^*$  state to a  $\pi\sigma^*$  state. In this state, the excited electron is located in a molecular orbital forming a solvated electron  $e^-_{solv}$  which can be seen in Figure 3.1d. The solvated electron has contributions from three antibonding OH-orbitals of solvent

molecules and a small contribution of a CH bond of DHI. Later examination of key structures led to the conclusion that the electron transfer to the solvent precedes the proton transfer, hence, Figure 3.1c follows Figure 3.1b before resulting in Figure 3.1d. The mechanism of this PCET mechanism was observed in both cluster systems. At these cluster geometries, the  $S_0$ - $S_1$  energy gap was found to reduce from almost 4 eV in the initial system to 0.5 eV after the PCET was completed. This small energy gap led to the conclusion that from this point on, relaxation to the ground state should occur on a short time scale.

This work will employ the clusters obtained after the PCET has been completed in both microsolvation clusters, which will be called initial systems henceforth. The structural arrangements of these specific clusters are now presented in more detail to introduce the labelling scheme used throughout this chapter and to describe the important features of the initial systems.

### 3.1.1 DHI-H<sub>2</sub>O Cluster

The DHI-water cluster consists of ten water molecules that are found close to the more hydrophilic functionalities of DHI, as can be seen in Figure 3.2. A hydronium ion is present due to the already completed proton transfer from the solute to the solvent. It is located close to the green-highlighted  $O_{DHI}$  and contains the  $H_{DHI}$ ,  ${}^1H_{pt}$ , and  ${}^2H_{pt}$  atoms. All H<sub>2</sub>O molecules form DHI-H<sub>2</sub>O or H<sub>2</sub>O-H<sub>2</sub>O hydrogen bonds to stabilize this molecular configuration of the cluster. However, three water molecules are arranged in a seemingly rather extraordinary conformation with three hydrogen atoms pointing inwards. The latter hydrogen atoms are marked in blue in Figure 3.2 and stabilize the solvated electron which has its center located in the middle of the triangle spanned by the three hydrogens. These electron-stabilizing hydrogens will be named  ${}^1H_{el}$ ,  ${}^2H_{el}$ , and  ${}^3H_{el}$  in the following discussion. The green tags represent the donated hydrogen atom ( $H_{DHI}$ ) and the oxygen atom from where it was detached ( $O_{DHI}$ ) during the PCET mechanism. The orange hydrogen atoms  ${}^1H_{pt}$ ,  ${}^2H_{pt}$ , and  ${}^3H_{pt}$  are prone to undergo proton transfer as will be seen later. All water molecules without any labels were found not to participate in the deactivation mechanism that was observed later on in the dynamics.

### 3.1.2 DHI-MeOH Cluster

The MeOH-DHI cluster has a simpler arrangement due to the reduced number of six solvent molecules. Similar to the water cluster, the solvent molecules are found close to the more hydrophilic functionalities of DHI, as can be seen in Figure 3.3. A doubly protonated MeOH molecule is present close to the green-highlighted  $O_{DHI}$ , which contains the  $H_{DHI}$ , and  ${}^1H_{pt}$  atoms. The labeling of important hydrogen atoms follows the same conventions employed for the H<sub>2</sub>O-DHI cluster: the atoms  ${}^1H_{el}$ ,  ${}^2H_{el}$ , and  ${}^3H_{el}$  stabilize the solvated electron, the

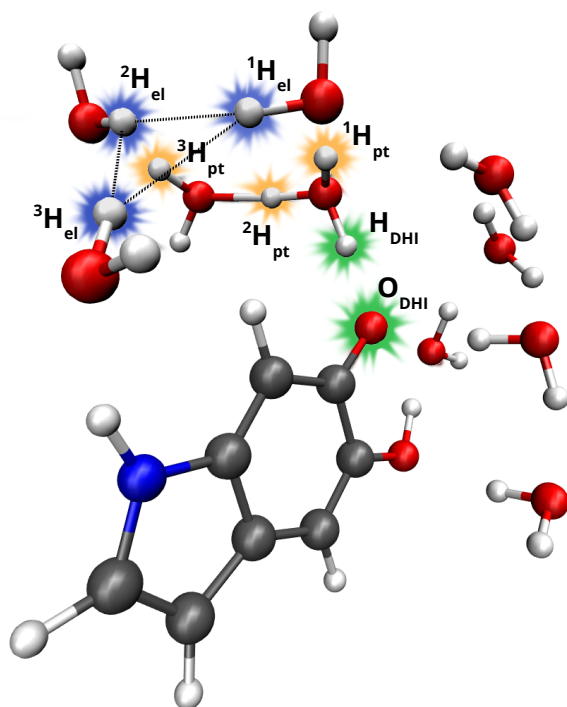


**Figure 3.2:**  $\text{H}_2\text{O}$ -DHI cluster system as used in Reference 18 which was obtained at the CAM-B3LYP/cc-pVDZ level of theory. Atoms that will play a role in the deactivation mechanisms or describe important structural features are highlighted and labelled; blue markings represent hydrogen atoms that stabilize the solvated electron, orange ones hydrogen atoms that were found to undergo proton transfer during the excited state deactivation, and green represents the atoms of the former hydroxy group of DHI prior to the PCET.

green  $\text{H}_{DHI}$  is the proton that was transferred from DHI to the solvent, and the green  $\text{O}_{DHI}$  is the former binding partner of  $\text{H}_{DHI}$ . In contrast to the water cluster, the number of protons that can get transferred during the simulations is reduced as the doubly protonated MeOH molecule has only one neighboring solvent molecule where it could transfer the proton ( ${}^1\text{H}_{pt}$ ) to, as will be seen later. The two remaining MeOH molecules without any label play no active role in the deactivation mechanism of the microsolvation cluster.

## 3.2 Stationary Excited State Calculations

With the geometries of the cluster systems at hand, a suitable electronic structure method had to be determined to investigate the excited state dynamics of the cluster systems. This represents a crucial step, as the electronic structure method

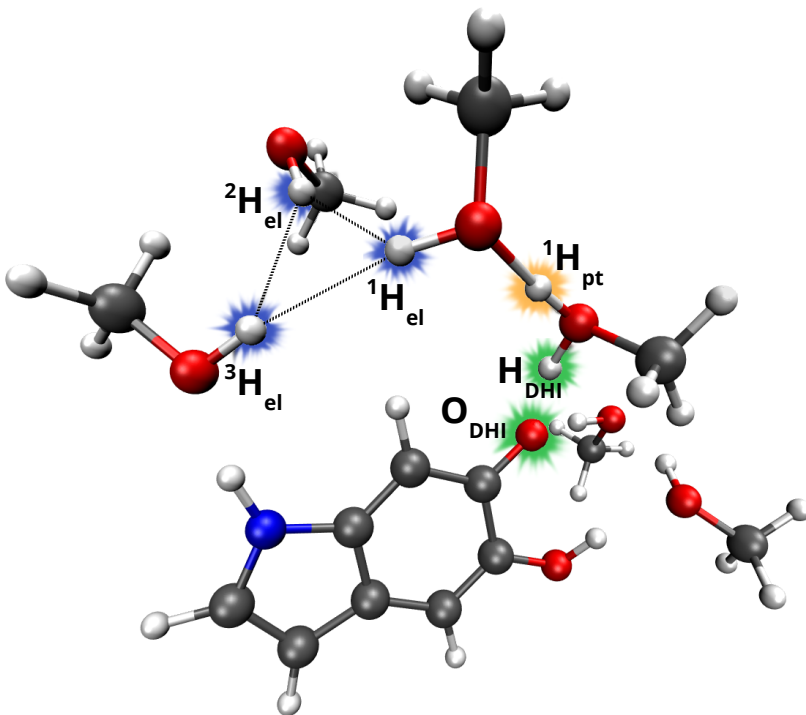


**Figure 3.3:** MeOH-DHI cluster system as used in reference 18 which was obtained at the CAM-B3LYP/cc-pVDZ level of theory. Atoms that will play a role in the deactivation mechanisms or describe important structural features are highlighted and labeled; blue markings represent hydrogen atoms that stabilize the solvated electron, orange ones hydrogen atoms that were found to undergo proton transfer during the excited state deactivation, and green represents the atoms of the former hydroxy group of DHI prior to the PCET.

is required to give very accurate results while at the same time being computationally affordable. This latter requirement is due to the fact that thousands of calculations are required during dynamical simulations. To find a method offering a good compromise between computational time and accuracy, stationary calculations were conducted on the clusters. The highest level of theory employed was MS-CASPT2<sup>36</sup>/cc-pVDZ<sup>56</sup> using 4 states (in the following just called CASPT2 calculation). This calculation and all related CASSCF calculations have been carried out using the MOLCAS 8.1<sup>57</sup> suite of programs. In all MOLCAS calculations, the two-electron integrals were approximated using the Cholesky<sup>58</sup> decomposition, the level shift<sup>37</sup> was set to 0.3 a.u and the IPEA shift<sup>59</sup> was set to 0.<sup>60</sup> Despite CASPT2 being a very time-consuming method and therefore unfeasible for dynamics computations, these calculations serve as a reference point to estimate the accuracy of other more economic methods. Agreement was consid-

ered good when energy gaps between different states could be reproduced. In the following section, the viability of TDDFT, ADC(2), and CASSCF as compared to CASPT2 is evaluated. Before delving into the details of this comparison, the CASPT2 results are described to explain the electronic structure of the clusters taken from Reference 18

### 3.2.1 CASPT2 Electronic Structure of the Clusters

Dihydroxyindole has 8  $\pi$  orbitals of which 6 are included in the active space of this calculation. The influence of the remaining two  $\pi$  orbitals on the calculated excited states was found to be small and these were therefore omitted for the sake of reducing the calculation time. The solvated electron is represented by a  $\sigma^*$  orbital that has large contributions from the three stabilizing OH-groups and also has to be incorporated in the active space. The resulting active spaces for the H<sub>2</sub>O-DHI and the MeOH-DHI clusters are shown in Figure 3.4 and Figure 3.5 respectively.

The results for the excited state calculations at the CASPT2/cc-pVDZ level of theory are given in Table 3.1. Here it can be seen, that the first excited state is dominated by a single transition from the  $\pi_1$  to the  $\sigma^*$  orbital in both cluster systems. This excitation has a high charge-transfer (CT) character as is readily apparent from the orbitals presented in Figures 3.4 and 3.5. The calculated  $S_0$ - $S_1$  energy gap equals 0.83 eV in the water cluster and 1.75 eV in the MeOH cluster. The second excited state is predicted 1.3 eV higher than the  $S_1$  in energy at both clusters and predominantly exhibits  $\pi_2\sigma^*$  character which again corresponds to a CT state.

State	Transition	$C$ [%]	$\Delta E$ [eV]
H <sub>2</sub> O-DHI			
$S_1$	$\pi_1 \rightarrow \sigma^*$	90	0.83
$S_2$	$\pi_2 \rightarrow \sigma^*$	88	2.14
$S_3$	$\pi_3 \rightarrow \sigma^*$	71	3.44
	$\pi_1 \rightarrow \sigma^* + \pi_1^*$	13	
MeOH-DHI			
$S_1$	$\pi_1 \rightarrow \sigma^*$	86	1.75
$S_2$	$\pi_2 \rightarrow \sigma^*$	82	3.03
$S_3$	$\pi_1 \rightarrow \pi_2^*$	61	4.10
	$\pi_2 \rightarrow \pi_1^*$	20	

**Table 3.1:** Excitation energies ( $\Delta E$ ) and transitions for the three lowest-lying excited states calculated at the CASPT2/cc-pVDZ level of theory averaging over 4 states. All excitation energies are given in eV,  $C$  is the contribution of the corresponding transition to the excited state in percentage.

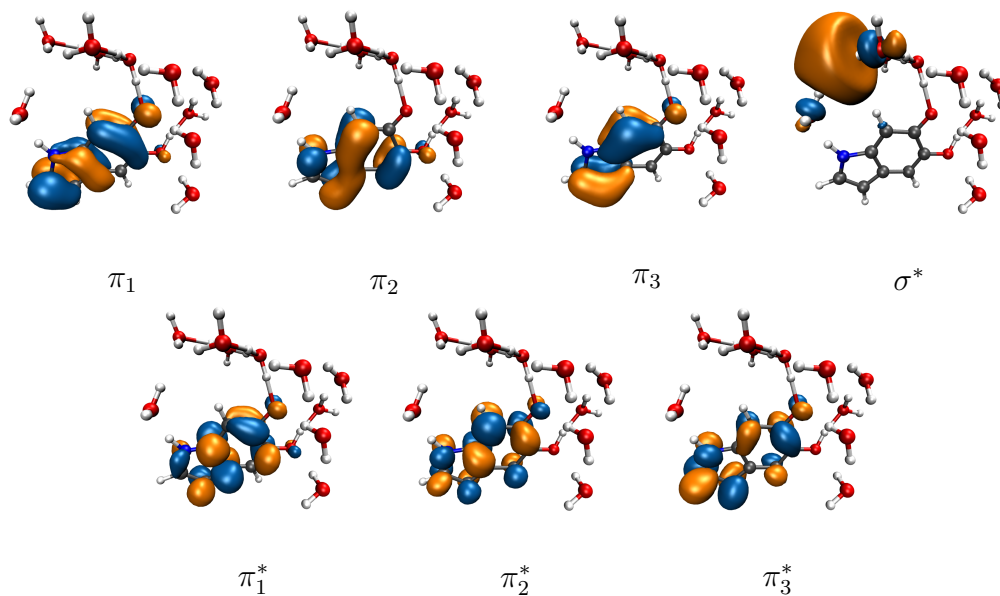


**Figure 3.4:** The orbitals comprising the (6,7) active space of the H<sub>2</sub>O-DHI cluster.

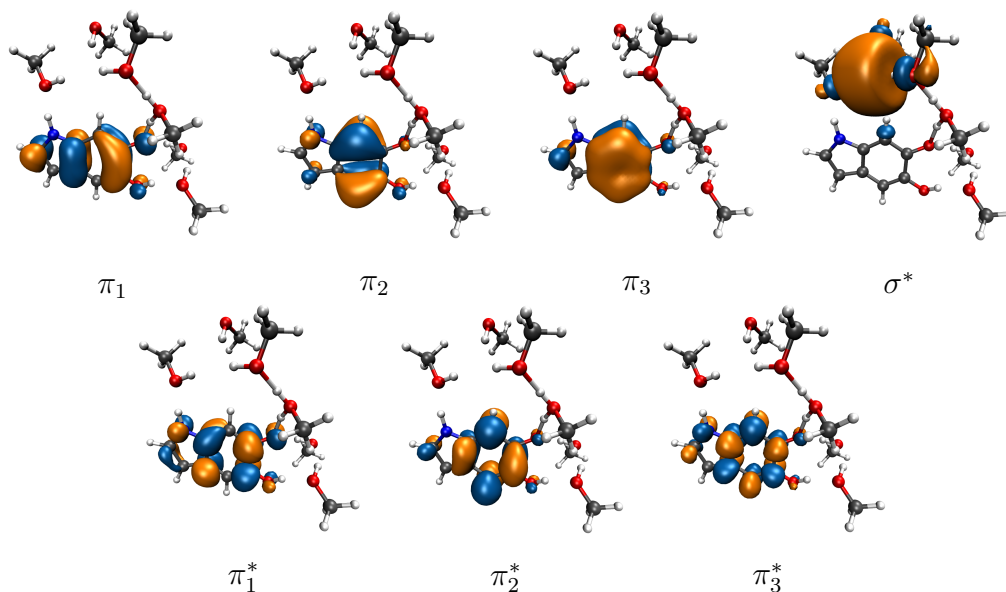


**Figure 3.5:** The orbitals comprising the (6,7) active space of the MeOH-DHI cluster.

### 3.2.2 Preliminary Benchmarking

In this section we compare the performance of different electronic structure methods against the previous CASPT2 results. An additional evaluation of the chosen methods will be presented in Section 3.4, using the results of the dynamics cal-

ulation.

For this initial benchmarking, the following methods have been considered: 4 states SA-CASSCF/cc-pVDZ computed with MOLCAS 8.1, ADC(2)<sup>39</sup>/def2-SVP<sup>61</sup> as implemented in TURBOMOLE 7.0<sup>62</sup> and TDDFT calculations using the B3LYP,<sup>63,64</sup> CAM-B3LYP,<sup>55</sup>  $\omega$ B97X,<sup>65,66</sup> and PBE0<sup>67</sup> functionals with the DZP<sup>68</sup> and the TZP<sup>68</sup> basis set from ADF2016.<sup>69-71</sup> The excitation energies computed at all these levels of theory are shown in Table A.1 of the Appendix. As can be seen there, the excitation energies calculated with B3LYP and PBE0 give a bad description for almost all excited states of the H<sub>2</sub>O-DHI cluster and completely fail to come close to the reference energies of the CASPT2 calculation on the MeOH-DHI cluster. Therefore, both methods are omitted in the following discussion. Increasing the basis set from DZP to TZP resulted only in small changes of the excitation energies for the CAM-B3LYP and the  $\omega$ B97X functionals while increasing computational time drastically. As increasing the basis set size did not necessarily result in better agreement with the reference calculation, only the results obtained at the functional/DZP level of theory are discussed in the following.

The excitation energies of the best performing methods are visualized in Figure 3.6a for the H<sub>2</sub>O-DHI cluster. As can be seen, the best agreement for all three depicted excited states was achieved using SA-CASSCF(6,7) averaging over four singlet states, i.e. the underlying calculation of the reference computation. ADC(2) overestimates the CASPT2 excitation energies by 0.5-0.8 eV. The range-separated functionals CAM-B3LYP and  $\omega$ B97X are also outperformed by CASSCF and give completely different estimations of the excitation energies. While the reference energies are underestimated by 0.3-0.5 eV at the CAM-B3LYP/DZP level of theory,  $\omega$ B97X overestimates the energies by 0.4-0.7 eV.

Results for the MeOH-DHI cluster can be seen in Figure 3.6b. ADC(2) excitation energies are overestimated in a range of 0.5-0.8 eV. The SA-CASSCF calculation gives a bad description of the third excited state which is overestimated by 0.9 eV while the first two excitation energies overestimate the CASPT2 energies by 0.3 eV. The CAM-B3LYP functional gives the best description of the MeOH-DHI cluster when looking at the error for all three states. The error for the first two excited states is almost equal to the CASSCF error and the error for the third excited state is the lowest one. As for the water cluster,  $\omega$ B97X overestimates the excitation energies by 0.4-0.8 eV.

Summarizing the results just presented, CASSCF yields the most accurate results for the water-DHI cluster but is slightly worse on the methanol-DHI cluster where CAM-B3LYP gives the best agreement with the reference calculation. Both ADC(2) and  $\omega$ B97X result in about 0.5 eV larger excitation energies at both clusters, when compared to the reference calculation.

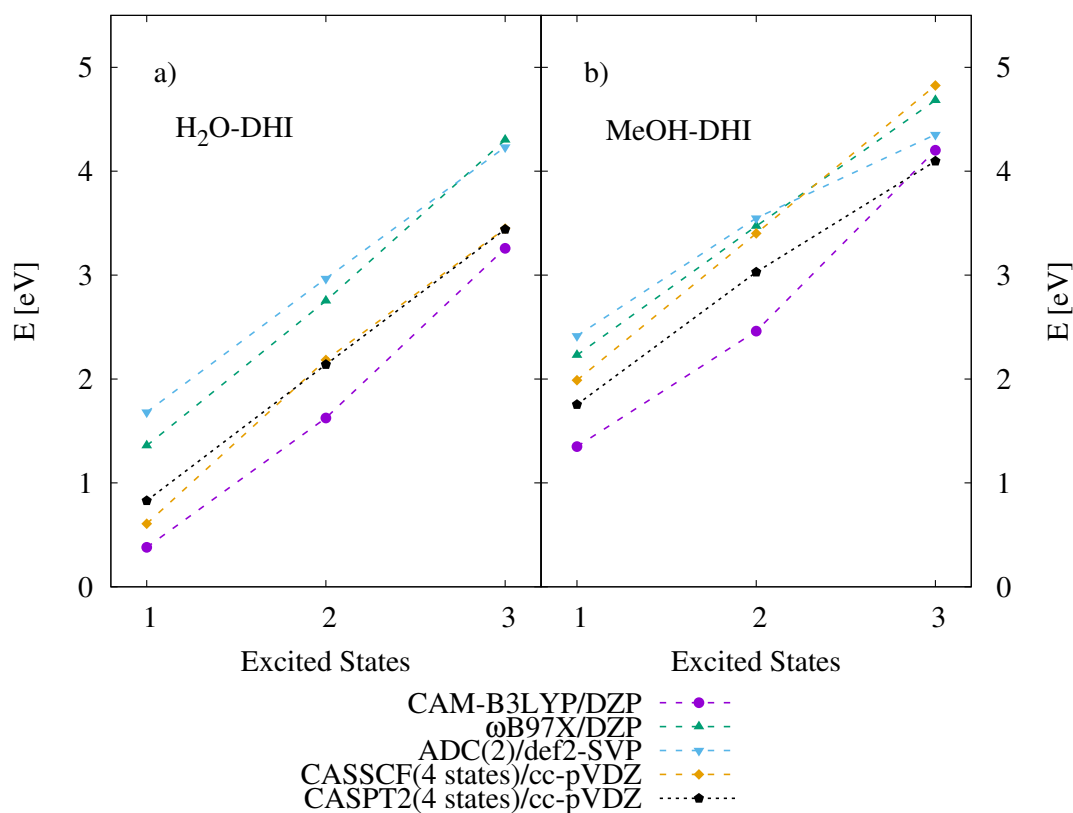


**Figure 3.6:** Calculated energies of the first three excited states for the H<sub>2</sub>O-DHI (a) and the MeOH-DHI (b) clusters at different levels of theory. Dashed lines are added between excited states of the same level of theory to allow for an easier comparison.

### Suitability for Dynamics Simulation

After accuracy, the second most important requirement that a method should meet is low computational cost. As explained in the theory part of this thesis, one electronic structure calculation has to be conducted at each time step to obtain excited state properties and the excited state gradients. The time needed for these calculations is crucial as it dictates the length of the whole simulation. Estimations of the total computer time to simulate a specific amount of time can be performed from dynamics simulations that are evolved for only a few time steps. Unfortunately, at this point we were confronted with the inability of various program packages to calculate analytical excited state gradients for range-separated functionals, as they are needed for the dynamics simulations. Therefore, range-separated functionals were not considered anymore in this work,

	ADC(2)		CASSCF	
	H <sub>2</sub> O-DHI	MeOH-DHI	H <sub>2</sub> O-DHI	MeOH-DHI
per ts	66 min	64 min	87 min	116 min
traj	46 d	44 d	60 d	81 d

**Table 3.2:** The row “per ts” contains the averaged times needed to calculate the 5<sup>th</sup> to 15<sup>th</sup> time step of an exemplary trajectory for each method at each of the cluster systems. The second row contains the estimated number of days to run a complete trajectory for 1000 time steps. ADC(2) trajectories were calculated on four cores while the CASSCF ones were restricted to one core as the amount of parallelization for those calculations is negligible. Both calculations were run on a machine using a Intel® Xeon® processor E5-2650 v1 at a clock rate of 2.00 GHz.

leaving only ADC(2) and CASSCF as options.

The average time needed to calculate a time step of the dynamics simulation for the different cluster systems with ADC(2) and CASSCF is given in Table 3.2. Clearly, ADC(2) outperforms CASSCF on both cluster systems, taking 21 min less per time step at the H<sub>2</sub>O-DHI cluster and 52 min less at the MeOH-DHI cluster. Adding up these differences for 1000 time steps at the H<sub>2</sub>O system, ADC(2) trajectories are assumed to take six and a half weeks which is two weeks faster than the corresponding CASSCF-driven simulation. The divergence in total time needed is much larger for the MeOH-DHI cluster where the ADC(2) trajectories would be finished five weeks in advance of the CASSCF trajectories. When combining efficiency and accuracy, the following can be concluded. On the one hand, ADC(2) was found to be more inaccurate in reproducing CASPT2 results at the static cluster system but is computationally more feasible. On the other hand, CASSCF was able to reproduce the excitation energies of the reference calculation very well but lags behind in computational performance. Both methods suffer from additional limitations in their use for dynamics calculations. Once the ground state is close in energy to an excited state, the ADC(2) formalism breaks down. Therefore, ADC(2) fails to describe the system once a conical intersection with the  $S_0$  is approached. To prevent the breakdown of ADC(2) from affecting the results, evaluation of ADC(2) simulations can be cut off once a  $S_0$ - $S_1$  energy gap of 0.15 eV is surpassed. Such a strategy has already been employed by Szabla *et al.*<sup>72</sup> on the investigation of smaller solute-solvent clusters and will be used in this work. Contrary to that, CASSCF is able to give a reasonable description of the system at such crossing points but may result in discontinuities of the calculated energies along the trajectory. These discontinuities in energy are caused by the nature of the SA approach (see the theory section of this work). In the SA approach, the obtained orbitals are the ones that minimize the average energy of all calculated states. In the case of dynamics simulations, the character of

the highest energy state may change in between time steps. If such a change occurs, the orbitals for the two time steps are obtained from minimizing different sets of states and therefore differ. The two sets of orbitals for both time steps result in a discontinuity in the calculated excitation energy at this point. Despite these drawbacks, both methods are routinely used for non-adiabatic surface hopping.<sup>73,74</sup> Therefore, we will employ them here too with the following strategy in mind: The ADC(2) trajectories are expected to give a stable description of the system until the threshold  $S_0$ - $S_1$  energy gap of 0.15 eV is reached. The CASSCF simulations in turn will be used to explore the dynamics in regions inaccessible to the ADC(2) trajectories.

### 3.3 Non-adiabatic Dynamics Calculations

With the choice of methods made, here we present the results obtained from the surface hopping dynamics simulations performed with ADC(2) and CASSCF. For this, a set of initial conditions was obtained beforehand from a Wigner distribution sampling. The normal modes for the sampling of the vibrational motion were obtained via a frequency calculation at the CAM-B3LYP/DZP level of theory. The CAM-B3LYP functional was chosen for the frequency calculations as the initial cluster systems were obtained with this functional. Some imaginary frequencies due to low-lying intermolecular normal modes were obtained, indicated by a corresponding negative frequency. The sign of those imaginary frequencies was reversed before sampling the initial conditions with a script included in the SHARC<sup>49,50,75</sup> program. A set of 20 initial conditions for each cluster system was obtained this way. ADC(2) dynamics simulations were performed on only 10 of those initial conditions for both cluster systems due to the associated computational cost of using four cores per trajectory. CASSCF simulations used all 20 initial conditions per cluster.

All generated initial conditions were set to start in the  $S_1$  state. Maximum simulation time was set to 500 fs using 0.5 fs time steps for the propagation of the nuclei and 0.02 fs for the electronic wavefunction. Interaction between gradients for energy gaps larger than 0.001 eV was forbidden.

In the following, the simulations using ADC(2) will be examined first to give an overview of the simulations at hand. Then, a more in-depth evaluation of the CASSCF trajectories will be shown. On the basis of these results, general deactivation mechanisms will be proposed and analyzed for both cluster systems.

#### 3.3.1 ADC(2) Trajectories

A summary of the events obtained by the ADC(2) simulations is collected in Table 3.3 for both cluster systems. The first cluster to be presented will be the H<sub>2</sub>O-DHI cluster.

	$n$	PT	PT to DHI	$\Delta E(S_1 - S_0)$	$t_{rel}$
H <sub>2</sub> O-DHI	10	6	3	6	274 fs
MeOH-DHI	10	10	1	9	18 fs

**Table 3.3:** Summary of the ADC(2) trajectories for both cluster systems. Here  $n$  denotes the number of trajectories simulated, “PT” is the number of trajectories where a proton transfer between solvent molecules occurred, and “PT to DHI” the number of trajectories where a proton transfer of H<sub>DHI</sub> from the solvent to O<sub>DHI</sub> was observed.  $\Delta E(S_1 - S_0)$  is the number of simulations where the threshold value of 0.15 eV was reached and the relaxation time ( $t_{rel}$ ) was obtained via a fit of the  $S_1$  excited state populations.

The ADC(2) trajectories at the H<sub>2</sub>O-DHI cluster were found to relax back to the adiabatic ground state within the simulated 500 fs in six out of ten cases. Additionally, most trajectories showed interactions of the hydronium ion with neighboring molecules via proton transfers<sup>†</sup>. Of the ten simulated trajectories, six approached the  $S_0$ - $S_1$  threshold value of 0.15 eV. The time passed until this threshold was reached ranged from 12.5 to 270 fs. Figure 3.7a shows the excited state populations for the two lowest-energy states during the simulated time. The time constant for the decay from the  $S_1$  to the  $S_0$  was obtained from an exponential fit and equals 274 fs. When looking at the trajectories at the point where the 0.15 eV gap is reached, no unifying geometrical feature accompanying the deactivating trajectories is discernible. This means that no geometric feature was identified as to facilitate excited state deactivation. The initial cluster system is depicted in Figure 3.8a, with all atoms important in the following discussion labeled. In two of the six deactivating trajectories, <sup>1</sup>H<sub>pt</sub> was transferred to the adjacent water molecule also containing <sup>1</sup>H<sub>el</sub> shortly before the limiting energy gap was reached. The other four reached the threshold value with all three hydrogens attached to the initial hydronium ion. Prior to deactivation, one of those four trajectories showed proton transfer to a neighboring water molecule from where the proton was transferred back after a short amount of time. A proton transfer of H<sub>DHI</sub> to O<sub>DHI</sub> was also observed in three of the simulations. Although this may seem to be a favorable event as this restores the initial geometry of all molecules before the excitation with light, the electronic state of the system is still the  $\pi\sigma^*$  state. However, in all of these three cases, the proton was reattached to the solvent molecule after varying amounts of time. This behavior seems to have no influence on the subsequent excited state dynamics as two out

<sup>†</sup>In the following a proton transfer will be said to have occurred once the distance between the hydrogen atom and the hydrogen bond bonding partner is shorter than the distance to the former covalently bound atom. An enhanced oscillation along the hydrogen bond may be labeled as a proton transfer followed by a transfer back to the original binding partner if the hydrogen atom comes close to the hydrogen bonding partner along the oscillation.

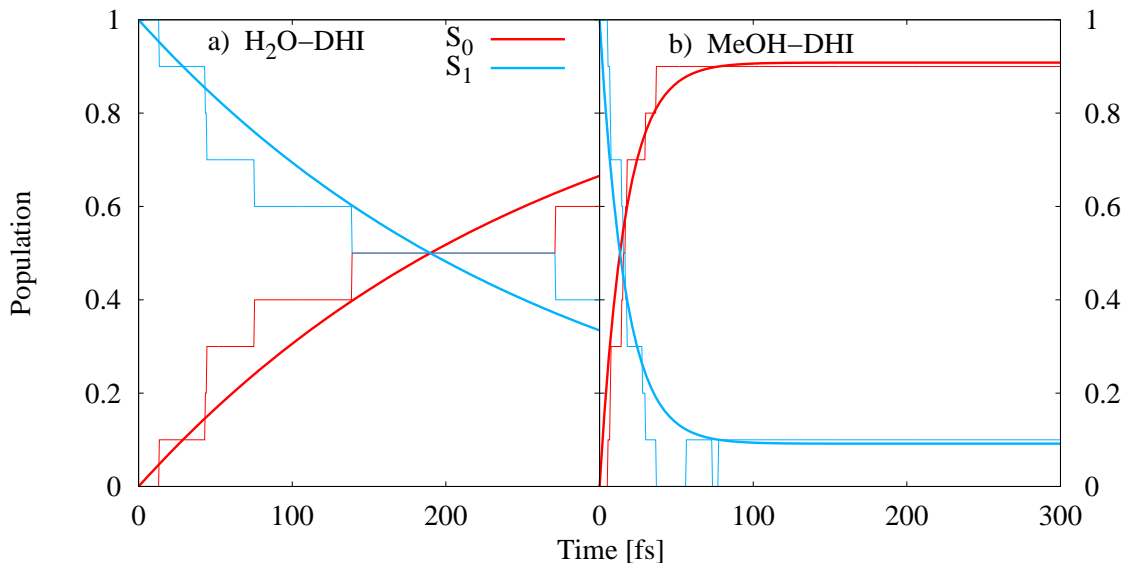


**Figure 3.7:** Excited state populations for the  $S_0$  and the  $S_1$  obtained from the ADC(2) dynamics for the H<sub>2</sub>O-DHI (a) and the MeOH-DHI (b) clusters. The thick lines represent exponential fits of the observed populations. The associated time constants for the relaxation from the  $S_1$  to the ground state equal 274 fs in water and 18 fs in methanol. It has to be noted, that this plot does not contain actual hops but the corresponding time when the limiting  $S_1$ - $S_0$  energy gap of 0.15 eV was surpassed. As the evaluation of the trajectories is stopped at this point, no return from the  $S_0$  to the  $S_1$  can possibly be observed. Therefore, the obtained relaxation time is assumed to be shorter than the actual excited state decay.

of the three trajectories where this proton transfer to DHI occurred relaxed to the ground state in the observed time scale once the proton was returned to the solvent. Two of the remaining four trajectories showed no proton transfer during the simulation. The other two trajectories showed proton transfer and back transfer to solvent or to DHI but did not relax to the ground state.

A drastically different picture is observed in the MeOH-DHI cluster. Here, the trajectories were found to undergo ultrafast deactivation to the  $S_0$  in a few dozen of femtoseconds with deactivation times ranging from 4 to 35 fs. Fitting of the corresponding excited state populations (see Figure 3.7b) yielded a time constant of 18 fs. Every deactivation was preceded by a proton transfer of  $^1\text{H}_{pt}$  to the neighboring hydrogen bonded MeOH molecule (see Figure 3.8b for the labeling). Hence, the deactivation does not occur at a geometry with the initially doubly protonated solvent molecule still intact but only after proton transfer along an already formed hydrogen bond to another solvent molecule. The rapidness of this hydrogen transfer indicates an energetically strongly favored conformation

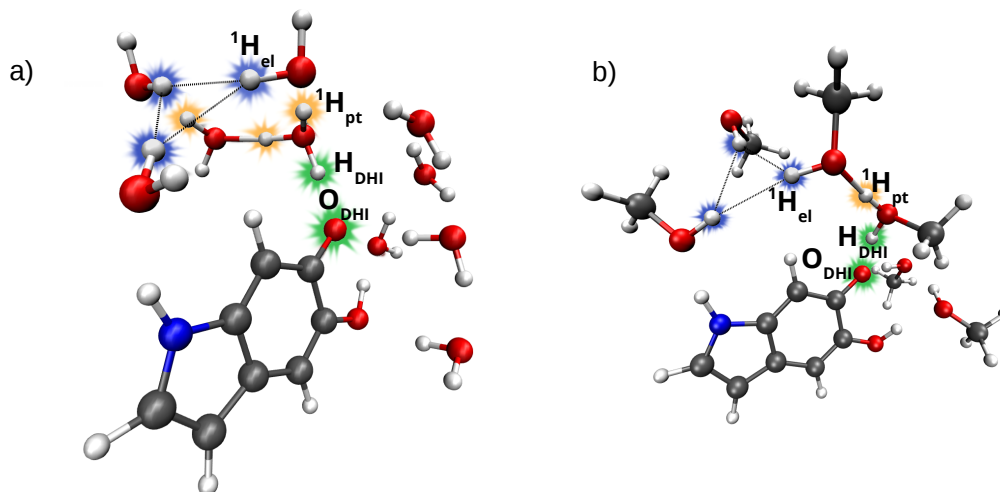


**Figure 3.8:** The  $\text{H}_2\text{O}$ -DHI (a) and the  $\text{MeOH}$ -DHI (b) clusters. Atoms important in the discussion of the ADC(2) trajectories are labeled. The highlighting of atoms is the following: blue markings represent hydrogen atoms that stabilize the solvated electron, orange ones hydrogen atoms that were found to undergo proton transfer during the excited state deactivation, and green represents the atoms of the former hydroxy group of DHI prior to the PCET.

where the positively charged solvent molecule is in direct proximity to the solvated electron. This concept of electron-driven proton transfers along preformed hydrogen bond “wires” was established recently by Szabla *et al.*<sup>72</sup> and applies for the  $\text{MeOH}$ -DHI cluster. Of the ten trajectories simulated, nine followed this relaxation pathway. In the one remaining trajectory, a proton was transferred to DHI after 8 fs where it stayed for the rest of the simulation time. In this conformation, the  $S_0$ - $S_1$  energy gap was found to increase to about 3 eV, rendering relaxation impossible. The inability to return the proton to the solvent molecule as in the  $\text{H}_2\text{O}$ -DHI cluster most likely stems from the larger energy barrier associated with this transfer in the  $\text{MeOH}$ -DHI cluster as was shown by Nogueira *et al.*<sup>18</sup>

Three main differences are encountered between the two cluster systems regarding their excited state dynamics behavior. First, the  $\text{MeOH}$ -DHI cluster was found to reach the limiting deactivation threshold value much faster than the  $\text{H}_2\text{O}$ -DHI cluster. Second, the deactivation in the  $\text{MeOH}$ -system is initiated via one geometric feature while the same does not hold true for the water cluster. The last difference is the energy barrier encountered upon transferring  $\text{H}_{\text{DHI}}$  from DHI to the solvent molecule after  $\text{H}_{\text{DHI}}$  has been transferred there in the  $S_1$ . This barrier seems to be larger in the case of the  $\text{MeOH}$ -DHI solvent cluster, increasing the likelihood of getting trapped in a state where  $\text{H}_{\text{DHI}}$  was transferred to DHI while still being in the first excited state. With these points discussed,

	$n$	PT	PT to DHI	dis	CS	$t_{rel}$
H <sub>2</sub> O-DHI	20	4	15	3	10	196 fs
MeOH-DHI	20	18	5	15	2	24 fs

**Table 3.4:** Summary of the CASSCF trajectories for both cluster systems. Here  $n$  denotes the number of trajectories simulated, “PT” is the number of trajectories where a proton transfer between solvent molecules occurred, and “PT to DHI” the number of trajectories where a proton transfer of H<sub>DHI</sub> from the solvent to O<sub>DHI</sub> was observed. The trajectories that returned to the lowest energy state are split in two groups: “dis” is the number of trajectories where a dissociation of a proton occurred in the  $\pi\sigma^*$  state while “CS” gives the number of trajectories that returned to a closed shell configuration. The time constant associated with the hop to the lowest energy state is given as  $t_{rel}$ .

the inability of ADC(2) to describe the complete deactivation mechanism of the solvent clusters is evident. While we get information about how the trajectories approach the limiting energy gap, we get no information about what happens at even smaller energy gaps and how the corresponding geometric features may change at these points. Furthermore, we have no information whatsoever about the mechanistic pathways of how H<sub>DHI</sub> will be reattached to DHI once the electronic ground state is reached. These informations should be provided by the CASSCF simulations which will be presented in the following.

### 3.3.2 CASSCF Trajectories

The results of the analysis of the CASSCF trajectories are collected in Table 3.4. As can be seen there, the number of deactivating trajectories can now be separated into two categories depending on their behavior following the deactivation to the  $S_0$ . After hopping to the lowest energy state, two things can be observed: either a transfer of H<sub>DHI</sub> to O<sub>DHI</sub> occurs which restores the initial geometry of DHI prior to activation with light, or the dissociation of a proton from one of the solvent molecules that combines with the solvated electron to form a hydrogen radical. Therefore, two deactivation pathways are accessible in both solvent clusters: a restoring pathway and a dissociative one. In the former case, the electronic configuration of the lowest energy state exhibits closed shell character while in the dissociation pathway, the lowest energy state has  $\pi\sigma^*$  character. The most important features of the excited state dynamics are presented in the following while a more detailed discussion of the observed deactivation mechanism will be presented after this section.

The 20 CASSCF trajectories at the H<sub>2</sub>O-DHI cluster were found to show a high amount of proton transfers to DHI and to the solvent. As can be seen in Table 3.4, a proton transfer between solvent molecules was observed in 4 of the

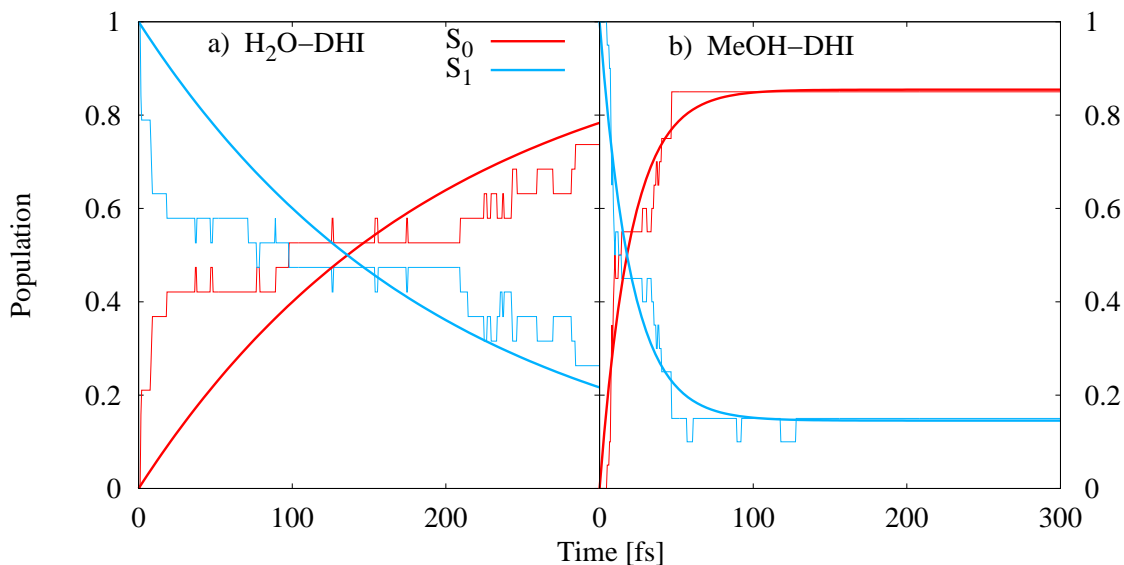


**Figure 3.9:** Excited state populations for the  $S_0$  and the  $S_1$  obtained from the CASSCF dynamics for the H<sub>2</sub>O-DHI (a) and the MeOH-DHI (b) clusters. The thick lines represent exponential fits of the observed populations. The associated time constants for the relaxation from the  $S_1$  to the ground state equal 196 fs in water and 24 fs in methanol.

trajectories while 15 trajectories showed proton transfer from the solvent to DHI. In the simulated time of 500 fs 13 trajectories hopped to the  $S_0$ . The associated time for this hopping ranges from 2 to 288 fs with a time constant of 196 fs. The corresponding excited state populations are plotted in Figure 3.9a. A schematic representation of all important steps of the excited state dynamics is given in Figure 3.10a where the interchange between all observed steps is plotted. Every rectangle in this figure represents a specific type of geometry: the initial state of the system where the solvated electron is present and the proton transferred to the solvent is labeled “in”. The geometry “DHI” is reached once the proton that was originally transferred to the solvent returns to DHI, restoring the structure of DHI. Transfer of a proton not to DHI but to another solvent molecule results in the geometry “PT”. The last geometry is “dis”, where a proton is dissociated by a solvent molecule into the vacuum surrounding the microsolvation cluster. The green and the blue box represent the  $S_1$  and the  $S_0$ . Initially, all trajectories start in the “in” geometry in the first excited state. From there, both the “DHI” and the “PT” geometries are observed as is the return to “in” from these geometries. Relaxation to the  $S_0$  occurs mainly at the “in” geometry (10 trajectories) but was also observed at “DHI” (1 trajectory) and “PT” (2 trajectories). From the relaxed “in” configuration, all but one trajectory transferred a proton to DHI after which no further proton transfers occurred, which means they ended up in

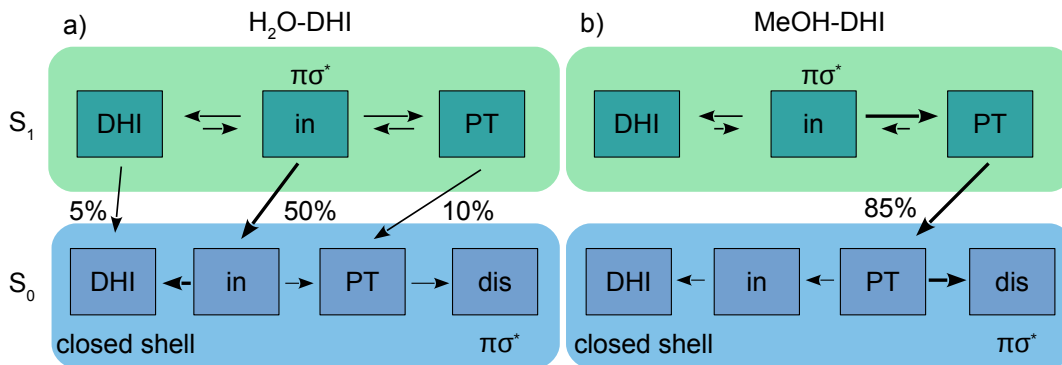


**Figure 3.10:** Overview of the different geometries accessed during the dynamics in the H<sub>2</sub>O-DHI (a) and the MeOH-DHI (b) clusters. Each block represents a type of geometry in either the  $S_1$  (green) or the  $S_0$  (blue). The initial structure (“in”) consists of the cluster system as taken from Reference 18. Transferring a proton from the solvent to DHI results in the geometry “DHI”, proton transfer between solvents leads to “PT”, and dissociation of a proton results in “dis”. The thickness of the arrow indicates how often this interchange of geometries was observed.

the “DHI” geometry. As the initial electronic and nuclear configuration of DHI is restored this way, this deactivation pathway is the restoring pathway. The remaining trajectory in the relaxed “in” state shows a solvent-solvent proton transfer which leads to conversion to the “PT” geometry. All trajectories that are at some point in the “PT” nuclear configuration in the  $S_0$  dissociate a proton, leading to the “dis” geometry in the corresponding dissociative pathway. Of the remaining 7 trajectories that did not return to the lowest energy state, 5 get trapped after a proton transfer to DHI in the “DHI” geometry. The other two trajectories crashed and could not be restarted.

The excited state dynamics at the MeOH-DHI cluster are found to be much faster and show less versatility than the dynamics on the H<sub>2</sub>O-DHI cluster. 17 of the trajectories returned to the ground state with a corresponding relaxation time constant of 24 fs (see Figure 3.9b). A general overview of the observed behavior in the trajectories is found in Figure 3.10b. There it can be seen that a quite distinct feature is needed for excited state deactivation, as all of the relaxing trajectories do so in the “PT” geometry. From the relaxed “PT” configuration, two trajectories undergo two subsequent proton transfers: first to the “in” conformation and then to “DHI” upon which the restoring pathway is completed. However, 15 trajectories follow the dissociative pathway and dissociate a proton in the ground state. The three remaining trajectories are found to be trapped after transferring  $H_{DHI}$  to DHI while still being in the first excited state.

Gratefully, when comparing the results from the CASSCF trajectories to the ADC(2) results, large similarities are evident. Both methods predict very similar

time scales for the deactivation of the MeOH-DHI cluster. The distinct deactivation condition in the MeOH-DHI cluster of transferring a proton from the initially doubly protonated MeOH molecule to another MeOH molecule is predicted by both methods. The one dissimilarity is encountered in the form of the trapping of trajectories after transfer of  $H_{DHI}$  to DHI. In ADC(2), the reversal of this proton transfer was possible in the  $H_2O$  cluster system but not in the MeOH cluster. The associated energy barriers upon reversion of this proton transfer seem to be larger in CASSCF as 5  $H_2O$ -DHI trajectories got trapped for hundreds of femtoseconds after transfer of  $H_{DHI}$  to DHI in the  $\pi\sigma^*$  state.

### 3.3.3 Relaxation Pathways in the Cluster Systems

A deeper analysis of the CASSCF trajectories will be shown in the following with the aim of providing insight into the observed deactivation mechanism of the cluster systems. ADC(2) trajectories are unable to provide information once the hopping point is approached and therefore cannot be used to investigate the mechanism once relaxation to the  $S_0$  occurred, which is the reason for focusing on the CASSCF results from now on.

#### H<sub>2</sub>O-DHI Cluster System

The  $H_2O$ -DHI cluster has shown two different excited state deactivation pathways. The restoring pathway is the main deactivation channel of this cluster and it is depicted in Figure 3.11. Relaxation to the  $S_1$  occurs after 18 fs with the initial hydronium ion still containing  $H_{DHI}$ ,  $^1H_{pt}$ , and  $^2H_{pt}$ . The solvated electron returns to DHI upon relaxation to the closed shell configuration - indicated by the blue arrow in the  $t=18$  fs snapshot. After relaxation,  $H_{DHI}$  is transferred to DHI, restoring the initial geometry ( $t=30$  fs).

The dissociative pathway leads to the formation of a hydrogen radical after one or multiple proton transfers (see Figure 3.12). In the shown trajectory, a solvent-solvent proton transfer of  $^2H_{pt}$  from the hydronium ion occurs after 60 fs. The newly formed hydronium ion has a hydrogen bond between  $^3H_{pt}$  and a neighboring water molecule. The formation of the hydronium ion weakens the O- $^3H_{pt}$  and the oscillations of this bond increase in intensity. The relaxation to the ground state of  $\pi\sigma^*$  character occurs at an elongated O- $^3H_{pt}$  bond length ( $t=98$  fs). After relaxation to the  $S_0$ ,  $^3H_{pt}$  is transferred to the neighboring water molecule ( $t=104$  fs). The formed hydronium ion is now in direct proximity to the solvated electron. In a next step, the hydronium ion dissociates a proton in the direction of the solvated electron ( $t=116$  fs). The proton and the solvated electron combine to form a hydrogen radical, which then leaves the cluster system.

Both pathways will be discussed in more detail, starting with the restoring pathway, paying attention to the geometries where the trajectories switch from the first excited state to the ground state, the so-called hopping geometries. In

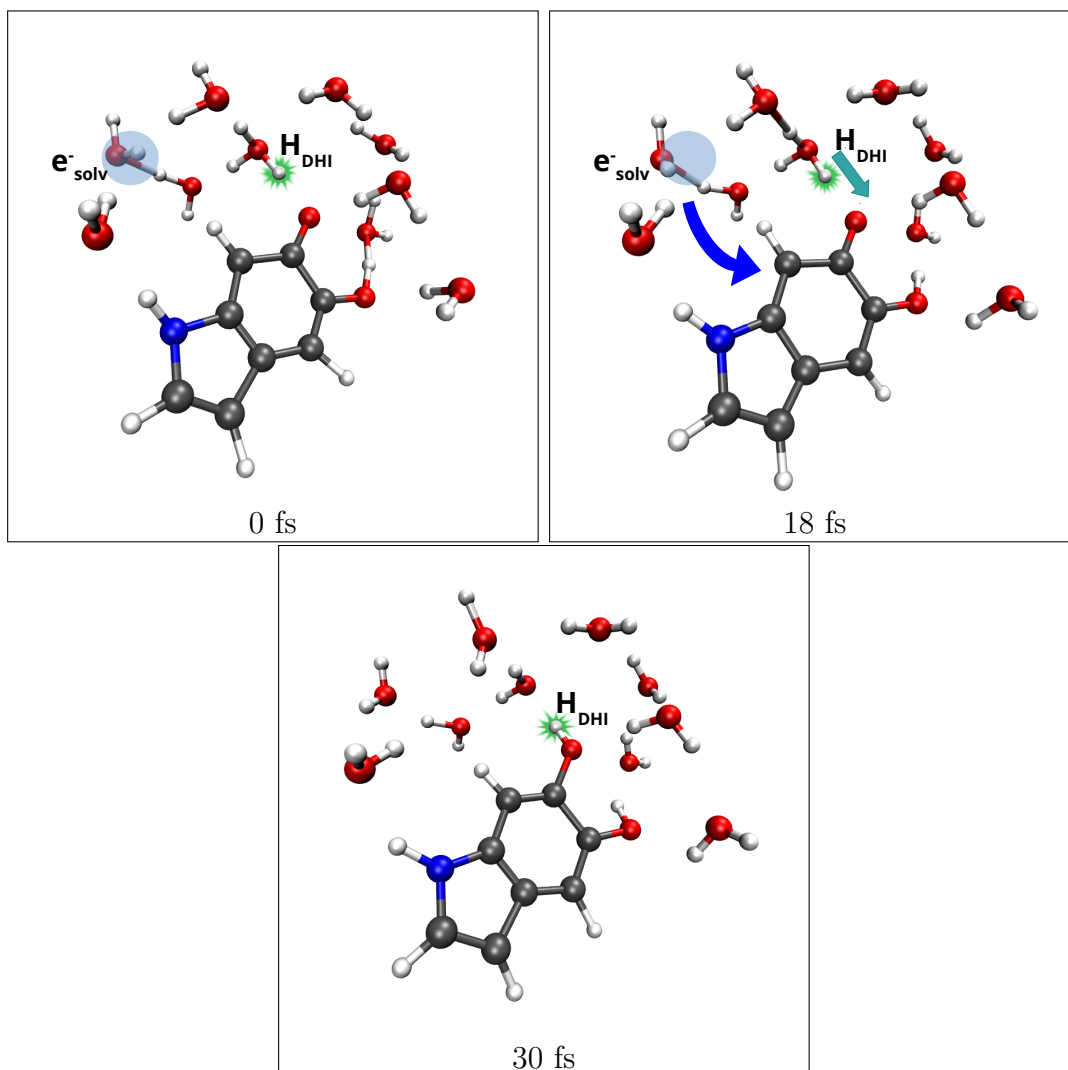


**Figure 3.11:** Snapshots of a representative trajectory of the  $\text{H}_2\text{O}$ -DHI cluster that follows the restoring relaxation pathway. Relaxation to the lowest energy state of closed shell character occurs at  $t=18$  fs.

Figure 3.13 all OH bond distances of the initial hydronium ion are plotted at these hopping geometries. Note that more dots than trajectories are visible in this plot since multiple hops can occur in one trajectory. In the case of the restoring pathway, relaxation occurs with  ${}^1\text{H}_{pt}$ ,  ${}^2\text{H}_{pt}$  and  $\text{H}_{DHI}$  being attached to the initially formed hydronium ion. For the restoring pathway, the average

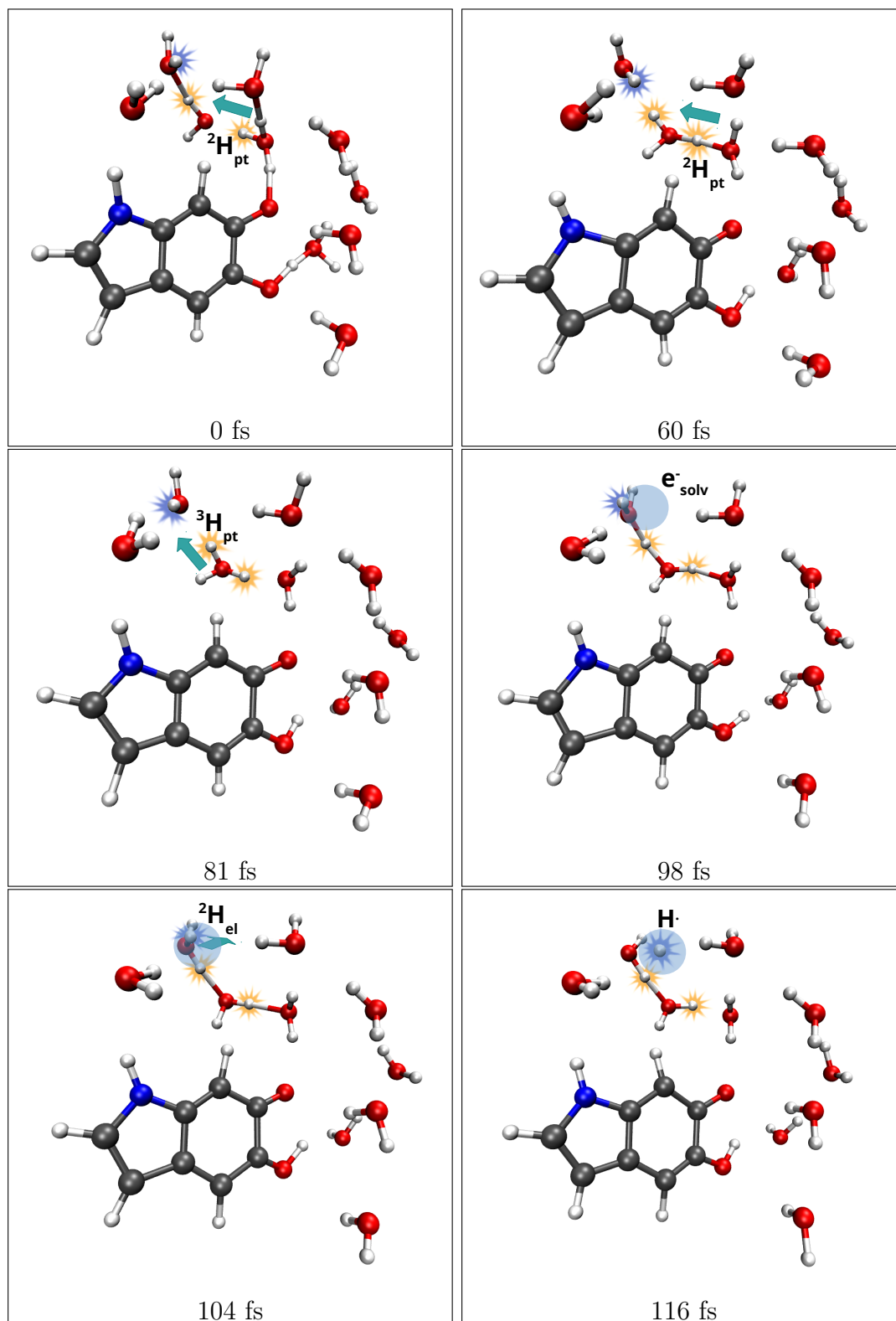


**Figure 3.12:** Snapshots of a trajectory of the H<sub>2</sub>O-DHI cluster that follows the dissociative relaxation pathway. Relaxation to the lowest energy state occurs at t=98 fs.

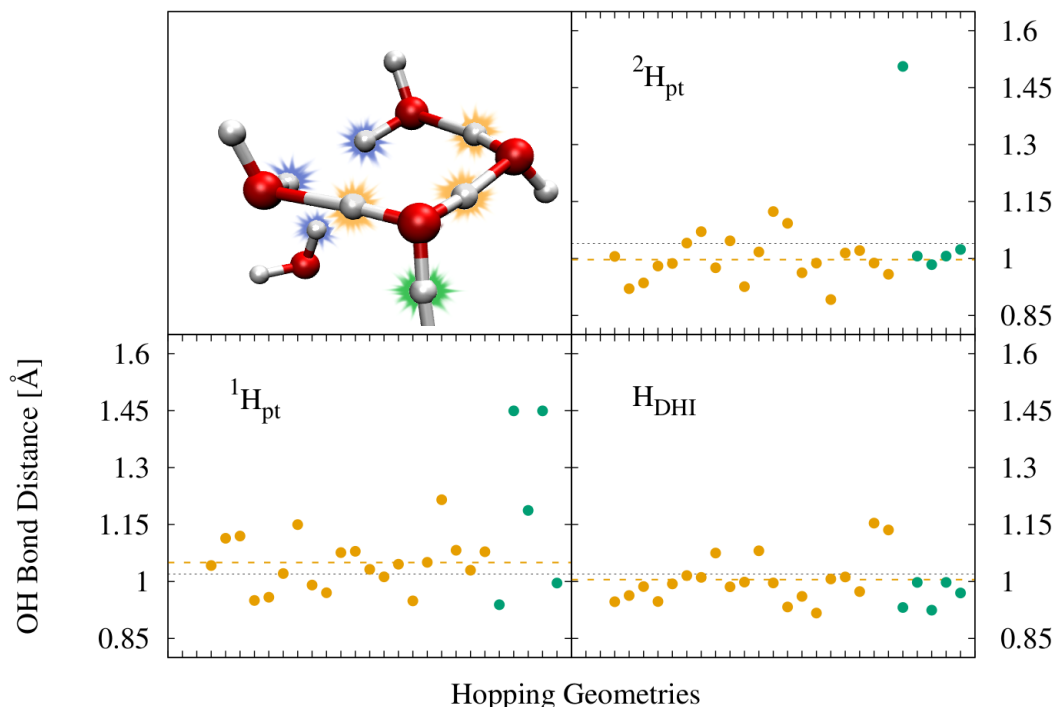


**Figure 3.13:** OH-bond distances at the geometries of the H<sub>2</sub>O-DHI cluster where the trajectories changed from the  $S_1$  to the lowest energy state. Orange dots represent trajectories that follow the restoring pathway while the green dots are trajectories that follow the dissociative pathway. The orange dashed line is the average of the orange dots. The bond distances at the initial cluster system are given as black dotted line.

bond distances at the hopping geometries are found to be  $0.03 \text{ \AA}$  larger than at the initial H<sub>2</sub>O cluster system for  ${}^1\text{H}_{pt}$ , and  $0.04 \text{ \AA}$  shorter for  ${}^2\text{H}_{pt}$ . Caution has to be taken when investigating the dynamics that follow the relaxation to the closed shell configuration as misleading information is produced. This is due to the return of the solvated electron to DHI which leaves the three hydrogens that formerly stabilized the solvated electron in a destabilizing configuration. The momentum generated by this repelling geometric configuration leads to the breakdown of the microsolvation model as the solvent molecules drift apart in the absence of another layer of solvent molecules. However, after relaxation to the closed shell ground state, a transfer of  $\text{H}_{DHI}$  to DHI in about 10 fs is observed in all of these trajectories. These 10 fs are well within the time window where the microsolvation model has not disbanded yet.

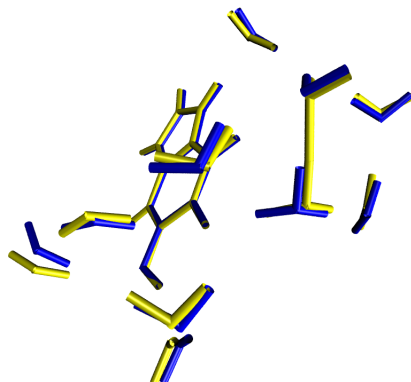


**Figure 3.14:** Superposition of the conical intersection geometry (yellow) for the H<sub>2</sub>O-DHI cluster optimized at the CASSCF/cc-pVDZ level of theory with the  $S_1$  optimized geometry at the same level of theory (blue).

With both the electronic closed shell configuration and the initial structure of DHI restored, this mechanism completely recovers the situation prior to excitation with light. Still, it is unclear how this pathway is initiated. Figure 3.13 shows only small deviations of the geometry at the hydronium ion of the hopping geometries when compared to the initial cluster. However, the  $S_0$ - $S_1$  energy gap was predicted to be 0.6 eV at the initial cluster system, which represents a large energy barrier to overcome when relaxing to the  $S_0$ . To gain more insight into the geometrical features that lower this energy barrier, the  $S_0$ - $S_1$  conical intersection was optimized. The resulting geometry is shown in Figure 3.14 together with the optimized  $S_1$  geometry. The conical intersection geometry was obtained at the CASSCF/cc-pVDZ level of theory using an interface that couples the MOLCAS calculation with the ORCA external optimization procedure<sup>76,77</sup> via a SHARC interface. Here it has to be noted, that the  $S_1$  minimum energy geometry as well as the conical intersection geometry differ in some features from the initial cluster systems. This difference is a direct consequence of the different levels of theory to obtain these system: the initial cluster was obtained from a CAM-B3LYP computation while the conical intersection geometry and the  $S_1$  minimum energy geometry were obtained with CASSCF. For a short discussion on this topic see Section A.3 in the Appendix. Coming back to Figure 3.14, both the conical intersection geometry as well as the  $S_1$  minimum-energy geometry are very similar and mainly differ in the position of solvent molecules that are not directly connected to the hydronium ion or the solvated electron. However, when comparing the  $S_0$ - $S_1$  energy gap, drastic differences are encountered. While the energy gap at the conical intersection geometry is 0.00 eV, an energy gap of 1.19 eV is obtained at the  $S_1$  minimum energy geometry. It is therefore concluded, that the reduction

of the energy gap to initiate the restoring relaxation pathway at the H<sub>2</sub>O-DHI cluster is due to a multitude of small bond elongations and contractions, as well as small changes in the position and orientation of neighboring solvent molecules.

When looking at the bond distances of the trajectories that follow the dissociative pathway, an elongation of the OH bond or a proton transfer has already taken place at the time of the hop in 4 out of 5 cases (see Figure 3.13). In the remaining case, the OH-bond breaks 2 fs after the hop. Here it can also be seen, that dissociation takes place regardless of which proton is transferred. Once the lowest energy state is reached dissociation of one of the H<sub>el</sub> protons after a few femtoseconds is observed. In the case where <sup>1</sup>H<sub>pt</sub> is transferred first the newly formed hydronium ion is already adjacent to the solvated electron and it can easily dissociate <sup>1</sup>H<sub>el</sub>. If not <sup>1</sup>H<sub>pt</sub> but <sup>2</sup>H<sub>pt</sub> is transferred during or after the hop, the mechanism follows the different steps depicted in Figure 3.12: the formed hydronium ion uses the preformed hydrogen bond-wire to transfer <sup>3</sup>H<sub>pt</sub> to a water molecule stabilizing the solvated electron. Once this step is completed a hydronium ion is formed capable of dissociating <sup>2</sup>H<sub>el</sub>. In both cases, the dissociated proton is propelled towards the solvated electron and receives additional momentum due to attractive interaction with the solvated electron. After traversing the center region of the solvated electron, the proximity to other hydrogen atoms pointing inwards leads to a repulsion of the proton. Next, either another repulsive interaction with another molecule changes the course of the proton again or it finally escapes into the vacuum surrounding the microsolvated cluster together with the formerly solvated electron as a hydrogen radical. However, the present cluster model cannot describe the dynamics after dissociation to the bulk solvent as only a small layer of solvent molecules is simulated. Hence, more information about the next steps of the relaxation mechanism cannot be obtained with the given solvent-cluster model. All in all, it can be concluded that this dissociative pathway does not restore the initial configuration of the DHI molecule prior to the excitation on a short time scale. The reasons for this assessment are that neither the initial structure of DHI was restored nor was the closed shell electron configuration. On the contrary, an additional reactive species in the form of a hydrogen radical is formed that passes the first layer of solvent molecules.

More information on the initiation of this dissociative pathway can be gathered by investigating each proton transfer explicitly by conducting scans along the OH bonds. Rigid scans along all hydrogen bonds involved in the dissociative pathway are plotted in Figure 3.15. These scans were obtained by elongating the corresponding OH bond by 15 increments of 0.05 Å, starting from a bond length of 0.82 Å. In the case of <sup>3</sup>H<sub>pt</sub>, some additional preparations have been conducted, as the elongation of this OH bond is only of importance if another proton transfer has already occurred. This can be seen in the mechanism depicted in Figure 3.12 where elongation of the O-<sup>3</sup>H<sub>pt</sub> is only of importance once <sup>2</sup>H<sub>pt</sub> has been transferred. Therefore, <sup>2</sup>H<sub>pt</sub> was manually attached to the water molecule of <sup>3</sup>H<sub>pt</sub> before the rigid scan was conducted to simulate this effect. The bond

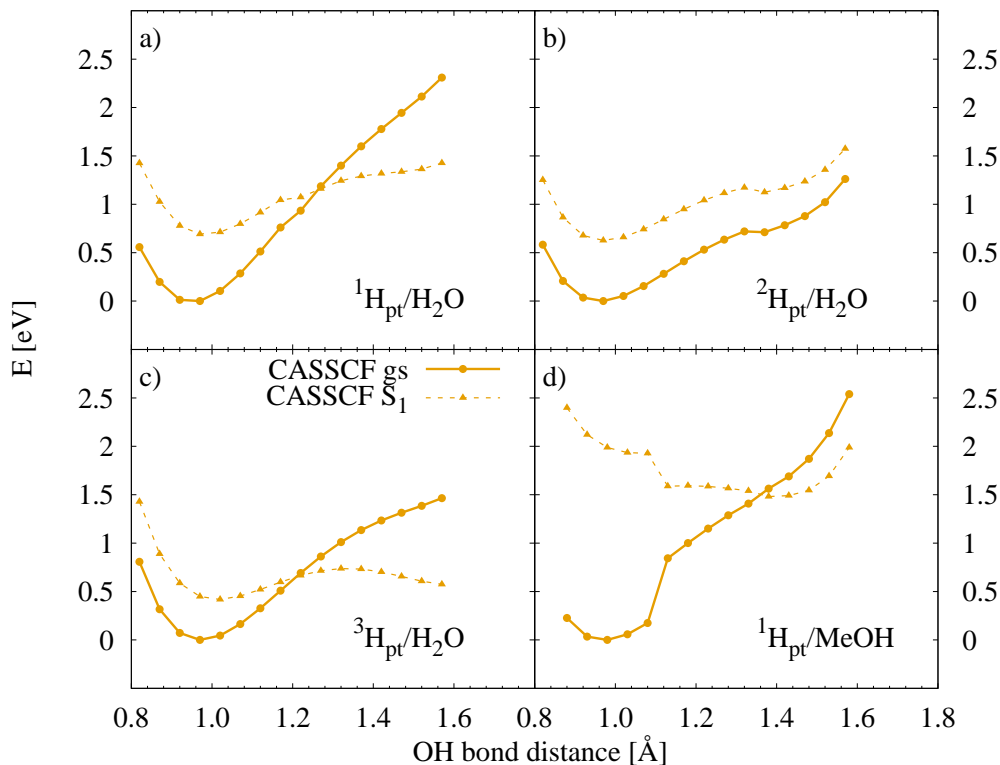


**Figure 3.15:** Rigid scans at the CASSCF/cc-pVDZ level of theory for all  $^x\text{H}_{pt}$  in the  $\text{H}_2\text{O}$  cluster as well as along the proton transfer axis of  $^1\text{H}_{pt}$  in the MeOH-DHI cluster. The scan along the O- $^3\text{H}_{pt}$  bond was conducted after transferring  $^2\text{H}_{pt}$  to the water molecule that contains  $^3\text{H}_{pt}$ .

length of the newly attached  $^2\text{H}_{pt}$  was set to 0.97 Å.

In Figure 3.15, it can be seen that elongation of a OH bond in the initial  $\text{H}_2\text{O}$ -DHI cluster in the  $S_1$  state is always associated with an energy barrier of 0.2 to 0.8 eV in the rigid scans. Due to the nature of rigid scans, this energy barrier is an overestimation of the energy gap encountered in the relaxed system. Crossing points with the  $S_0$  are encountered only for transfers of  $^1\text{H}_{pt}$  and  $^3\text{H}_{pt}$ . In the case of  $^2\text{H}_{pt}$  no crossing point is predicted along elongation of the OH bond. However, transfer of  $^2\text{H}_{pt}$  facilitates deactivation via the O- $^3\text{H}_{pt}$  bond. The scan along this OH bond resulted not only in the smallest associated energy barrier but also a crossing point between the  $S_1$  and the  $S_0$  at the comparatively small bond distance of 1.24 Å. When conducting relaxed scans in the first excited state along the same OH bonds, a completely different picture is encountered as can be seen in Figure 3.16. These scans started from an initial bond length of 0.98 Å and featured 6 increments of 0.1 Å. In the case of the O- $^3\text{H}_{pt}$  bond,  $^2\text{H}_{pt}$  was held fixed at 0.97 Å to the host of  $^3\text{H}_{pt}$  throughout the constrained optimization. No

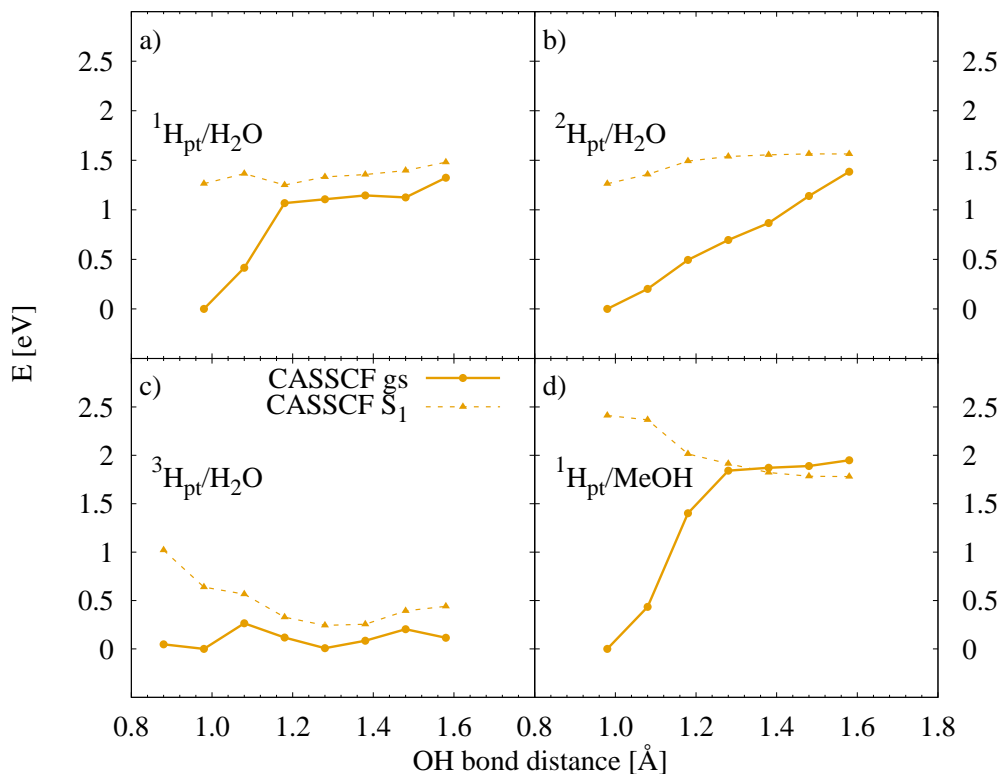


**Figure 3.16:** Relaxed scans in the first excited state at the CASSCF/cc-pVDZ level of theory for all  $^xH_{pt}$  in the  $H_2O$  water cluster as well as along the proton transfer axis of  $^1H_{pt}$  in the MeOH-DHI cluster. The scan along the O- $^3H_{pt}$  bond was conducted after transferring  $^2H_{pt}$  to the water molecule that contains  $^3H_{pt}$ .

crossing point is encountered along all three proton transfer axes when moving along the  $S_1$  minimum energy path of the bond elongations. The scan rather predicts very flat  $S_1$  energy profiles that are almost barrierless along elongation of OH bonds for  $^1H_{pt}$  or  $^2H_{pt}$  and even favors elongation of the O- $^3H_{pt}$  bond. Although no crossing point is reached in the relaxed scans, the  $S_0$ - $S_1$  energy gap decreases with elongation of all OH bonds and even retains a rather constant value of about 0.2 eV for OH bond elongations including  $^1H_{pt}$  and  $^3H_{pt}$ .

Combining the scans and the results of the dynamics simulation, three conclusions can be drawn regarding the dissociative pathway. First, elongation of  $^1H_{pt}$  or  $^2H_{pt}$  is an uphill reaction and can lead to a crossing point. Second, every trajectory that encountered a conical intersection upon elongation of a OH bond followed the dissociative pathway where the  $\pi\sigma^*$  state is the lowest energy state. Third, the relaxation in the dissociative pathway does not follow the  $S_1$  minimum energy path since no crossing point with the  $S_0$  is observed but rather is dependent on small changes in the surrounding solvent molecules.

### MeOH-DHI Cluster System

The MeOH-DHI cluster shows two excited state deactivation pathways. Similar to the H<sub>2</sub>O-DHI system, one results in a return to the closed shell electron configuration and a transfer of H<sub>DHI</sub> to the unprotonated oxygen atom of DHI. In the other, a change in the character of the lowest energy state is observed after a hop to the  $S_0$  which is then of  $\pi\sigma^*$  character. This electronic configuration then finally leads to the dissociation of a hydrogen radical. Unlike the H<sub>2</sub>O-DHI cluster, the latter pathway is found to be the major relaxation pathway in the MeOH cluster with 15 of 20 trajectories following this mechanism. Only two of the trajectories relaxed according to the other mechanism.

Snapshots of a trajectory that follows the dissociative relaxation pathway of the MeOH-DHI cluster are depicted in Figure 3.17. Here it can be seen that the first step in the deactivation mechanism of this trajectory is a proton transfer of

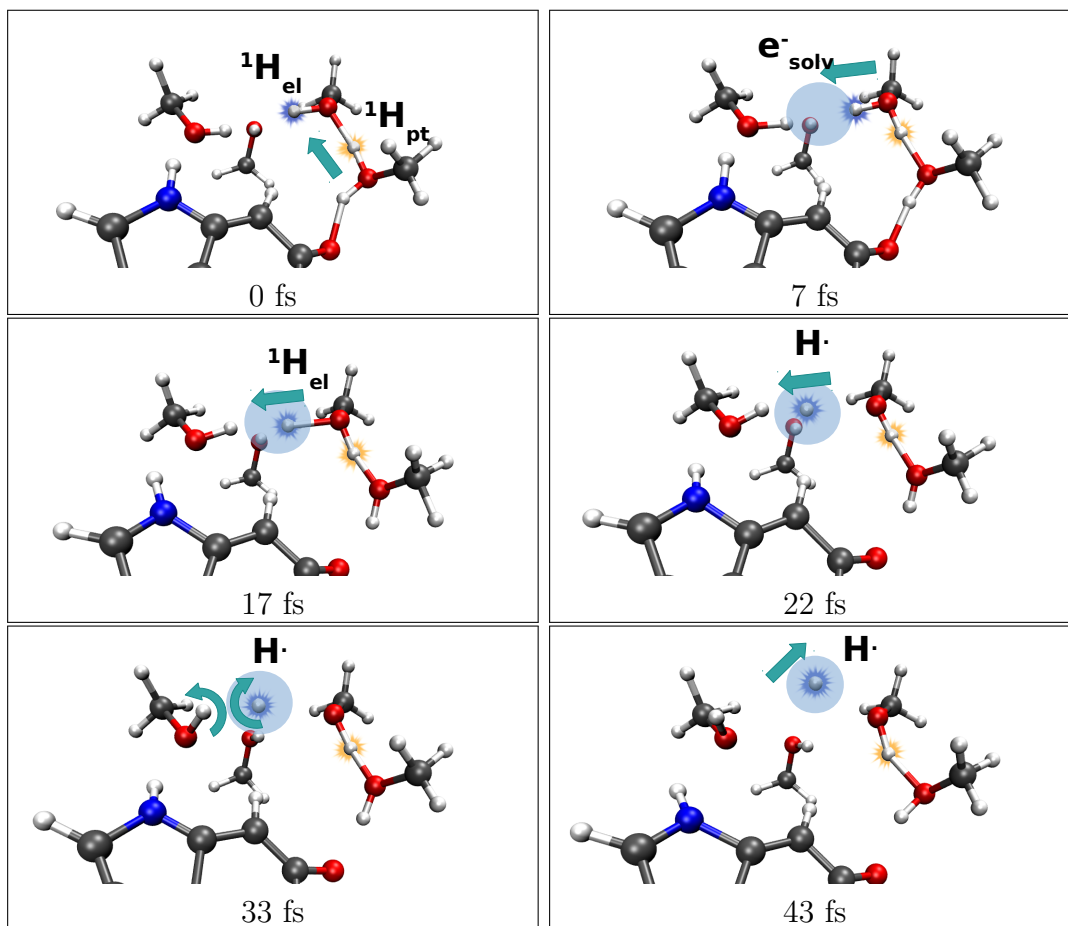


**Figure 3.17:** Snapshots of a representative trajectory of the MeOH-DHI cluster that follows the dissociative relaxation pathway. Relaxation to the lowest energy state occurs at  $t=7$  fs.

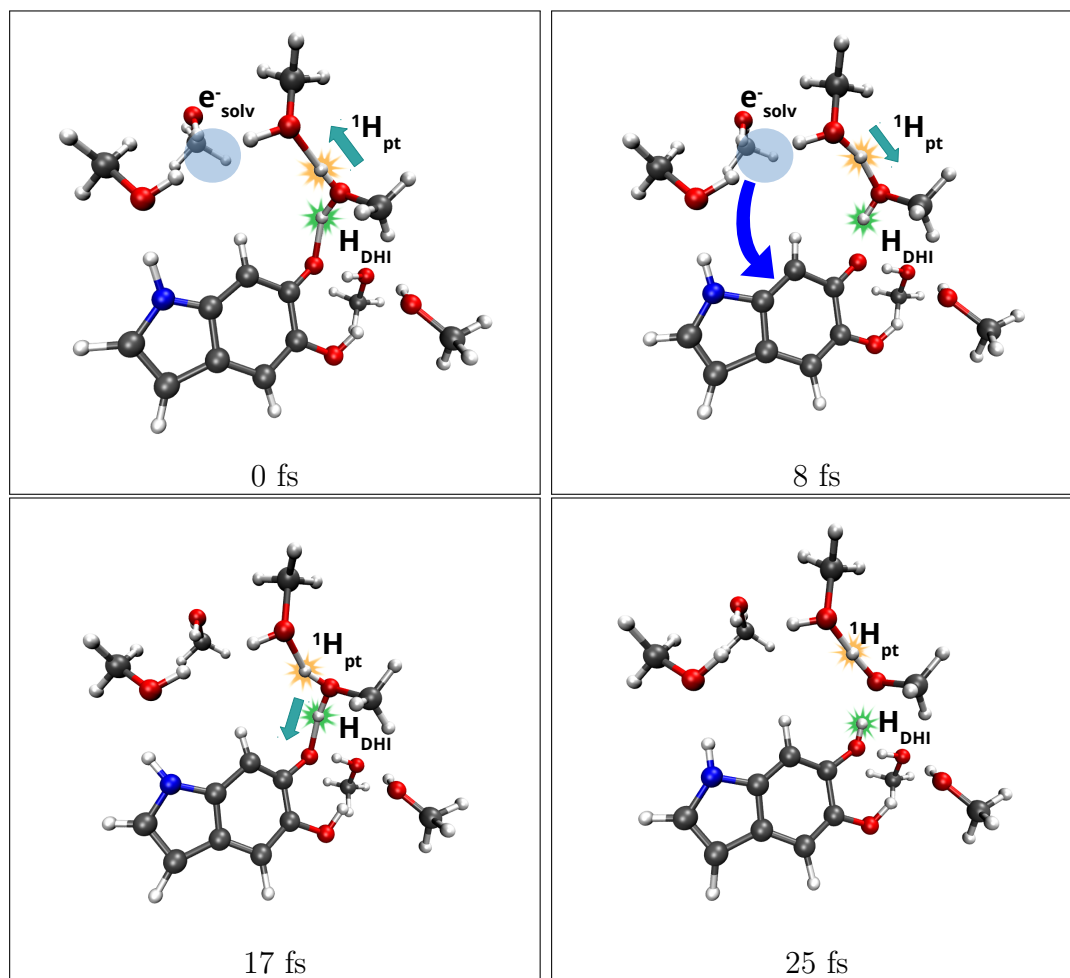


**Figure 3.18:** Snapshots of a representative trajectory of the MeOH-DHI cluster that follows the restoring relaxation pathway. Relaxation to the lowest energy state occurs for  $t=8$  fs.

$^1\text{H}_{pt}$  along a hydrogen bond from the  $\text{MeOH}_2^+$  molecule to a neighboring MeOH molecule in 7 fs. Relaxation to the ground state occurs in a geometric configuration where the proton transfer has been completed. The lowest energy state in this case is of  $\pi\sigma^*$  character and the solvated electron remains intact. After a few oscillations of the  $\text{O}-^1\text{H}_{el}$  bond towards the solvated electron,  $^1\text{H}_{el}$  is dissociated to form a hydrogen radical at the 22 fs snapshot. The momentum of the hydrogen radical leads to a close proximity of the hydrogen radical with another hydrogen that formerly stabilized the solvated electron. Both hydrogens repel each other as can be seen in the 33 fs snapshot. The new velocity vector of the hydrogen radical faces out of the microsolvation cluster which finally leads to an ejection of the hydrogen radical out of the cluster system.

The restoring pathway is depicted in Figure 3.18. The first step of the deacti-

vation mechanism is again a hydrogen transfer of  ${}^1\text{H}_{pt}$  from the doubly protonated MeOH molecule to a MeOH molecule that stabilizes the solvated electron. This proton transfer is completed after a few femtoseconds. Relaxation to the ground state occurs in this geometric conformation at the 8 fs snapshot. The lowest energy state is of closed shell character in this trajectory which means that the solvated electron is transferred back to DHI. After relaxation to the ground state,  ${}^1\text{H}_{pt}$  is transferred back to the MeOH molecule where it originated from (see snapshot at 17 fs). Finally,  $\text{H}_{DHI}$  is reattached to DHI which completes the restoring pathway after another 8 fs.

The OH bond distances at the hopping geometries for both hydrogens at the initially doubly protonated MeOH molecule are shown in Figure 3.19. Both the dissociative and the restoring pathway are initiated after  ${}^1\text{H}_{pt}$  has been transferred along the hydrogen bond towards a MeOH molecule that stabilizes the solvated electron. This proton transfer was not fully completed when approaching the  $S_0$ - $S_1$  hopping point only in two of the trajectories that followed the dissociative pathway. The choice of a particular pathway seems to be governed by small changes in the interactions of the molecules instead of a clear-cut geometric feature. Contrary to the water cluster it is therefore not possible to discern both pathways by observing the hopping geometries. Rigid and relaxed scans along this proton transfer axis are given in Figures 3.15d and 3.16d. Note the discontinuity in the energies predicted for the rigid scan at 1.1 Å as another state entered the state-average space of the calculation as discussed in Section 3.2.2. Both scans predict elongation along this bond to be downhill in energy in the  $S_1$  state. This explains the readiness of the trajectories to transfer this proton on such a short time scale. A crossing point between the  $S_0$  and the  $S_1$  is encountered in both scans. This crossing point is predicted to occur at bond elongations of 1.32 Å and 1.36 Å in the relaxed and the rigid scan, respectively. The average hopping bond length in the simulations was found to be 1.38 Å which is in good agreement with the scans.

### Comparison of the Relaxation Pathways on the two Clusters

Two relaxation pathways were identified to occur in both cluster systems: a restoring pathway and a dissociative one. Although the exact mechanisms for a given pathway differ between the clusters, the key points in the mechanisms are strikingly similar: The restoring pathway restores the initial electronic and nuclear configuration of DHI. The first step in this mechanism is the restoration of the closed shell electron configuration by relaxing to the  $S_0$ . Then the proton is transferred from the solvent to DHI after which this pathway is completed. The dissociative pathway is initiated by one or more solvent-solvent proton transfers. After at least one proton transfer, the trajectories relaxed to the  $S_0$  of  $\pi\sigma^*$  character. After a few femtoseconds, a proton is dissociated in direct proximity to the solvated electron. The dissociated proton and the solvated electron com-

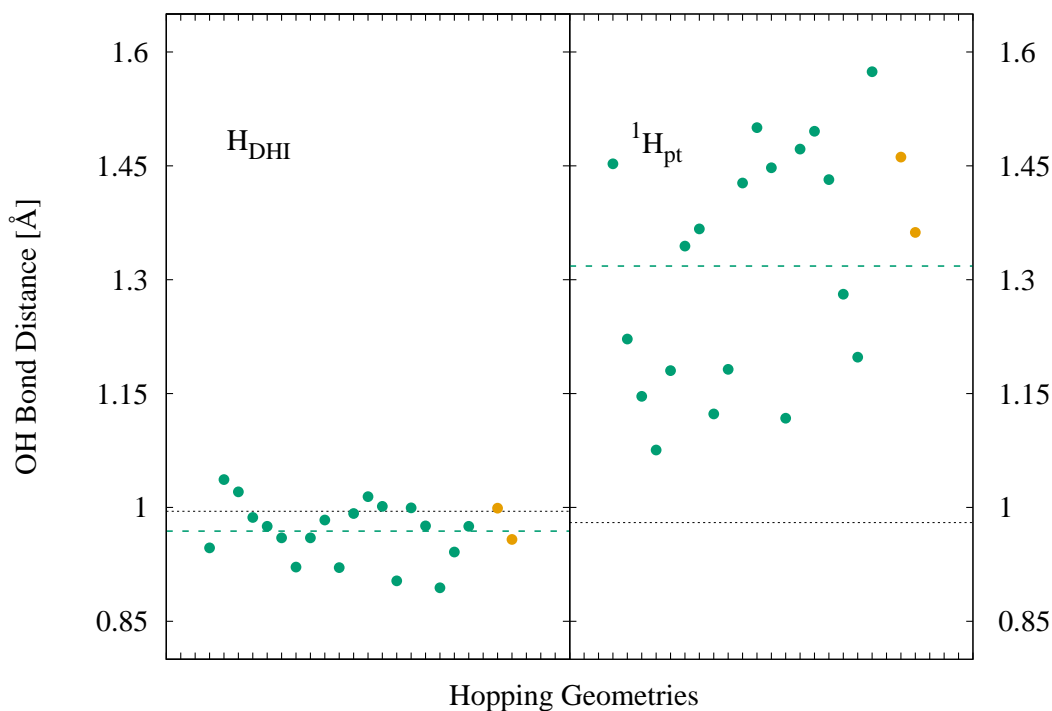


**Figure 3.19:** Important OH-bond distances of the MeOH-DHI cluster at the geometries where the trajectories changed from the  $S_1$  to the lowest energy state. Green dots represent trajectories that follow the dissociative pathway while the orange dots are trajectories that follow the restoring pathway. The green dashed line is the average of the green dots. The bond distances at the initial cluster system are given as black dotted line.

bine to form a hydrogen radical which leaves the DHI-solvent cluster. The most prominent differences between the two systems concern the nature of the major pathway and the corresponding relaxation time. While the restoring pathway is by far more dominant in the water cluster, the opposite is observed for the MeOH-DHI cluster. This can be reasoned by looking at the hopping geometries: in the water cluster, the dissociative mechanism was initiated by returning to the ground state after transferring  ${}^1\text{H}_{pt}$ . This results in a conformation where the hydronium and hence the positive charge is now located closer to the solvated electron. From this geometric arrangement, further transfers of protons along  $\text{H}_2\text{O}$  wires closer to the solvated electron seem to be preferred over returning the proton back to the initial hydronium. Once the proton has been transferred to a solvent molecule that stabilizes the solvated electron, the stabilizing proton is dissociated. Due to the presence of energy barriers associated with proton transfers from the initial hydronium in the water cluster, most trajectories return to

the ground state without transferring a proton to another solvent molecule. In the MeOH-DHI cluster, the transfer of  ${}^1\text{H}_{pt}$  is a downhill reaction and therefore occurs in a few fs. Deactivation to the ground state occurs readily in this geometry as can be seen in the presented scans or the conical intersection geometry. Hence, the trajectories of the MeOH cluster hop to the lowest energy state while the doubly protonated MeOH molecules is stabilizing the solvated electron. The dissociative pathway is readily accessible from this geometry which makes this pathway the dominant one in the MeOH cluster. The downhill  $S_1$  energy profile along the  ${}^1\text{H}_{pt}$  proton transfer axis to access geometries with a small  $S_0$ - $S_1$  energy gap is also the reason for the shorter observed relaxation time in the MeOH system. Due to this downhill reaction, it is energetically favorable to enter regions close to a crossing point which leads to faster relaxation times compared to the  $\text{H}_2\text{O}$ -DHI cluster where the reduction of the  $S_0$ - $S_1$  energy gap is dependent on a number of small changes and not a single geometric component.

As already mentioned, the dissociative pathway leads to the formation of reactive radicals that seem to penetrate deeper into the surrounding bulk solvent which increases their lifetime. However, due to the breakdown of the microsolvation model, no conclusion about this can be drawn for sure. Nevertheless, two different pathways seem accessible from the point where the hydrogen radical is formed: either the separation between DHI and the hydrogen radical increases which decreases the likelihood for direct recombination of the two species. Or, the presence of the actual bulk solvent hinders the hydrogen radical from distancing itself from the DHI radical. The former option would favor formation of various radical compounds until recombination of the radicals occur. The latter pathway would result in a contained hydrogen radical which at some point may eventually return to DHI. A short discussion on the possible latter mechanism and how it could possibly be observed in the dynamics simulations by increasing the size of the microsolvation cluster is shown in Section A.2 in the Appendix. Experimental work on DHI has shown that monomeric DHI is not photostable, but found the samples to be degraded after prolonged exposure of up to 10 minutes to light.<sup>20</sup> This verifies that reactive radical species can be formed during the deactivation mechanism. However, the extent of radical formation is either largely overestimated in the simulations or deactivation of the radicals in the bulk solvent occurs shortly after the formation of the hydrogen radical.

## 3.4 A Posteriori Benchmarking of CASSCF

In Section 3.2 the viability of CASSCF was investigated at the initial cluster system where it fared quite well. However, as mentioned above, CASSCF is often considered to be a rather unreliable method. Therefore, to estimate the accuracy of CASSCF in the description of the cluster systems throughout the dynamics simulations, various a posteriori comparisons with CASPT2 will be presented in this section.

### 3.4.1 Static Calculations at Key Points in the Trajectories

The most straightforward way to estimate the accuracy of a given method during the simulations consists in taking key points from the trajectories and conduct static calculations at those nuclear configurations. This has been done for one trajectory of each cluster system that followed the dissociative pathway. The reason for taking this pathway was the assumption that the description of the electronic configuration throughout the dissociative pathway is more complicated than the return to a closed shell configuration. The energetic profiles of the two sampled trajectories are shown in Figure 3.20. The following discussion will start with the trajectory of the H<sub>2</sub>O-DHI cluster which can be found in Figure 3.20a. Here it can be seen that the  $S_0$ - $S_1$  energy gap predicted at the CASSCF and the CASPT2 levels of theory differ by a maximum of 0.5 eV. The CASSCF crossing point is found at 8 fs in the graph. At this point the CASPT2 energy gap equals 0.38 eV with the closed shell configuration being the  $S_0$ . For the latter points, a difference between the static CASSCF  $S_0$ - $S_1$  energy gap and the one obtained from the dynamics simulations, also at CASSCF level, is observed. This is due to a change in the active space in the dynamics, which is triggered through the exchange of two states in the SA approach while the active space used for the static calculations was the one presented in Figure 3.4. C When looking at the MeOH-trajectory, similar trends are observed albeit larger differences in the calculated energy gaps are observed. The largest deviation between CASSCF and CASPT2 excitation energies is found at 14 fs where it equals 1.00 eV. In the few femtoseconds where the  $S_0$  and the  $S_1$  are almost isoenergetic, the CASPT2 excitation energy equals 0.3-0.4 eV. Similar to the H<sub>2</sub>O cluster, the crossing point is only surpassed at later time steps.

In conclusion, calculated differences between CASSCF and CASPT2 in the excitation energies along the dynamics are in the same range as the differences found in the static calculations at the initial cluster geometries. This means that slightly smaller differences between the CASSCF and the CASPT2 results are encountered for computations at the water cluster compared to the methanol cluster where the initial static calculations showed a larger gap between both methods. However, the CASPT2 calculations still show a large separation of the

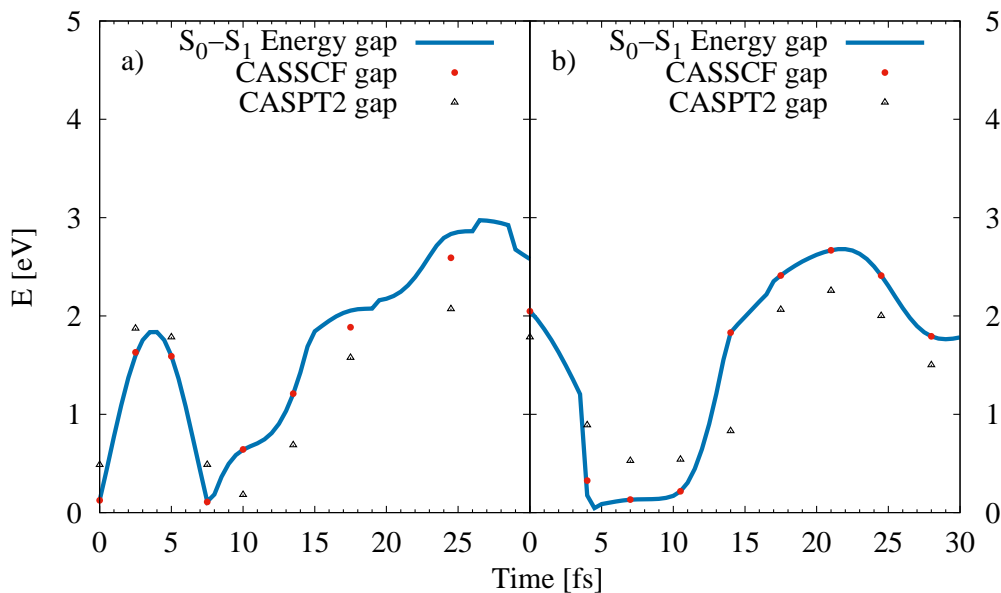


**Figure 3.20:** Two examples of trajectories that follow the dissociating pathway. On the left hand side (a), a trajectory of the water cluster is shown while the right hand side (b) shows a trajectory of the MeOH cluster. The blue line is the CASSCF  $S_0$ - $S_1$  energy gap obtained from the dynamics calculations. Red dots and black triangles depict the  $S_0$ - $S_1$  energy gap at the CASSCF/cc-pVDZ and the CASPT2/cc-pVDZ level of theory, respectively on the geometry at the corresponding point in the trajectory. For the last two points in panel a), differences between the CASSCF  $S_0$ - $S_1$  energy gap in the trajectory and the static calculation occurred due to changes in the active space in the dynamics that are not reflected in the static calculations.

$S_0$  and the  $S_1$  at geometries where CASSCF predicts them to be almost isoenergetic. This can be demonstrated better by comparing the energies obtained at the CASSCF optimized conical intersection geometries. When looking at the  $S_0$ - $S_1$  energy gap at the conical intersection geometry at the water cluster, this energy is found to equate to 0.37 eV at the CASPT2/cc-pVDZ level of theory. In the MeOH-DHI cluster the CASPT2 excitation energy is found to be 0.51 eV at the conical intersection geometry. These values are slightly worse than the average differences between CASSCF and CASPT2 energies obtained so far. General agreement with CASPT2 is remarkably good for CASSCF. In an attempt to further assess the quality of the description,  $S_0$ - $S_1$  crossing points of CASPT2 along important OH bond lengths are investigated in the following section.

### 3.4.2 Rigid Scans

The rigid scans of OH bond lengths already conducted for CASSCF in Section 3.3.3 of both cluster systems have been repeated at the CASPT2/cc-pVDZ level of theory. The resulting potential energy scans are shown in Figure 3.21.

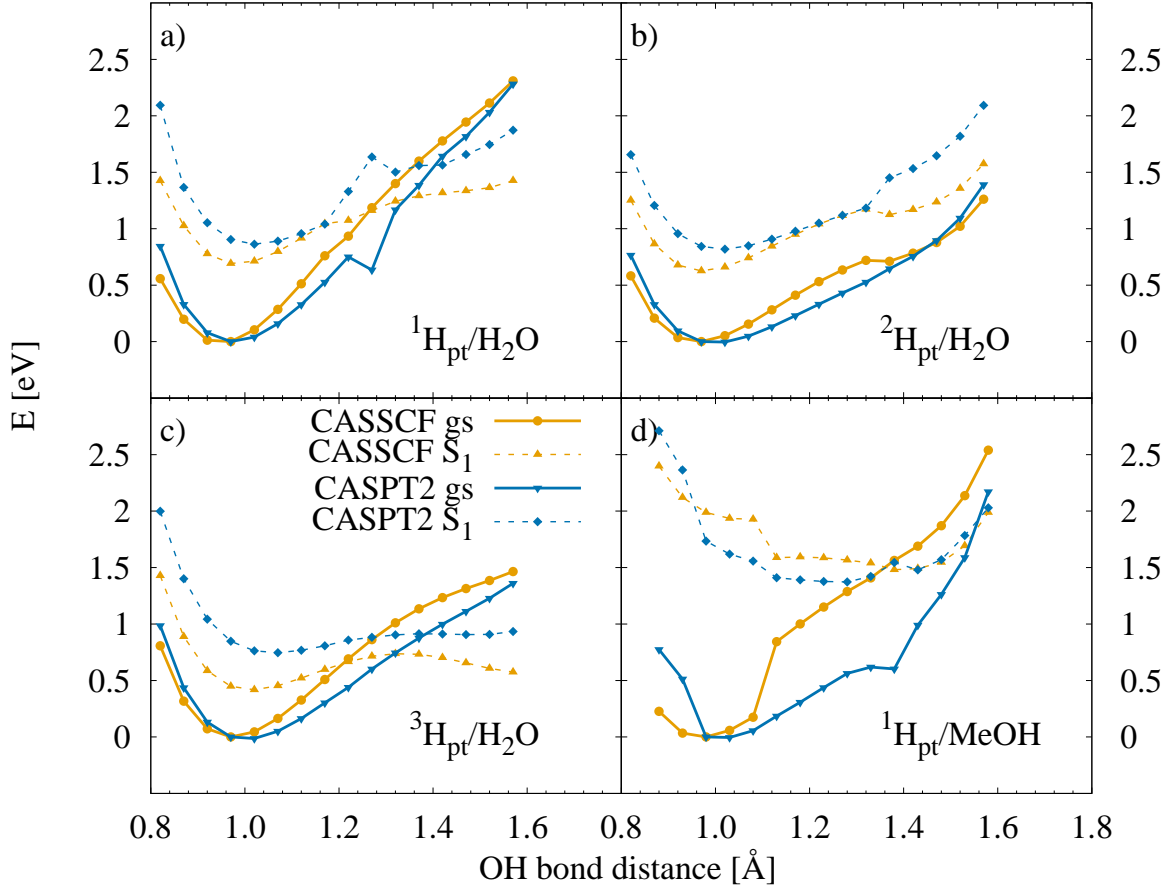


**Figure 3.21:** Rigid scans at the CASSCF/cc-pVDZ and the CASPT2/cc-pVDZ levels of theory for all  $^x\text{H}_{pt}$  in the  $\text{H}_2\text{O}$  water cluster as well as along the proton transfer axis of  $^1\text{H}_{pt}$  in the MeOH-DHI cluster. The scan along the O- $^3\text{H}_{pt}$  bond was conducted after transferring  $^2\text{H}_{pt}$  to the water molecule that contains  $^3\text{H}_{pt}$ .

For the  $\text{H}_2\text{O}$ -DHI cluster, all CASSCF scans are found to be in good qualitative agreement with the CASPT2 trajectories. As already discussed in the previous section, CASPT2 yields excitation energies for the  $S_1$  at the crossing point geometries of CASSCF that are in the same order of magnitude as the value obtained at the conical intersection geometry. However, here it can be seen that the CASPT2  $S_0$ - $S_1$  energy gap diminishes upon further bond elongation by about 0.2 Å. Hence, crossing points in CASPT2 and CASSCF are encountered

along the same proton transfer axes in the rigid scans. Surprisingly, an unexpected behavior of the CASPT2 calculation was observed in the scan along the  $O-^1H_{pt}$  axis as the description of the CASPT2 states seems to break down at the CASSCF crossing point at 1.25 Å (see Figure 3.21a). This should not be the case in CASPT2 computations but neither inspection for intruder states nor checking the active space produced any indication on the nature of this behavior. This was also observed in the MeOH cluster scan (Figure 3.21d) albeit to a lesser extent. However it was not detected at the crossing point in the  $O-^3H_{pt}$  scan (Figure 3.21c).

When looking at the scan along the proton transfer axis in the MeOH-DHI cluster in Figure 3.21D, the degree of agreement between the CASSCF and the CASPT2 scan is reduced compared to the water cluster. The nature of this discontinuity has been discussed in Section 3.2.2. With the CASPT2 scan at hand, the influence this has on the predicted features can be estimated. The discontinuity is encountered at a bond length of 1.1 Å. At this point, the  $0-1$  energy gap decreases from 1.7 eV to 0.75 eV. This behavior is not observed in CASPT2 which proves this rapid change in the excitation energy to be a mere artifact of the SA approach. Upon further elongating this OH bond, a crossing point is reached according to the CASSCF computation. The corresponding crossing point in CASPT2 is only reached once the proton transfer is complete and a distance of 0.98 Å to the newly bond oxygen is reached. Note that the  $S_1$  energy profile is uphill before reaching this crossing point.

The comparison of the rigid CASSCF and CASPT2 scans gives an indication on how far the conical intersections at both methods are separated. For the  $H_2O$ -DHI cluster a good agreement between both scans was found. Crossing points for CASPT2 were detected at slightly larger OH-bond distances compared to the CASSCF crossing points. Combining these observations with the energy gap observed along the trajectory, it is concluded that CASSCF gives a good description of the dynamic processes occurring at the  $H_2O$ -DHI cluster system. In the MeOH-DHI cluster, larger deviations between the CASSCF and the CASPT2 scan were detected. However, the downhill  $S_1$  energy profile for the transfer of  $^1H_{pt}$  combined with a decreasing  $S_0-S_1$  energy gap along this proton transfer axis is found in the CASSCF and the CASPT2 scan. Therefore it is assumed, that a qualitative description of the excited state dynamics at the MeOH-DHI cluster can be achieved with CASSCF.

## 4. Summary

In this thesis, the excited state dynamics of solvent-5,6-dihydroxyindole (DHI) clusters were investigated. DHI is one of the main building blocks of eumelanin, which acts as photoprotector in the human skin. The examined cluster systems contained 10 water ( $\text{H}_2\text{O}$ ) molecules and 6 methanol ( $\text{MeOH}$ ) molecules surrounding DHI. A previous theoretical study<sup>18</sup> on these cluster systems was able to trace the initiation of a possible relaxation mechanism where an electron and a proton are subsequently transferred from DHI to the surrounding solvent molecules. However, the static calculations employed in that investigation<sup>18</sup> proved insufficient to elucidate the subsequent deactivation steps. These were investigated in this study by non-adiabatic excited state dynamics simulations starting from the cluster systems. For the propagation of the semi-classical trajectories, the SHARC program package<sup>49,50,75</sup> was used in combination with ADC(2) and CASSCF *on the fly* electronic structure calculations.

ADC(2) trajectories evidence a higher reactivity in methanol compared to water. Of the 10 simulated trajectories of the MeOH-DHI cluster, 9 reached a degeneracy between the ground ( $S_0$ ) and the first excited state ( $S_1$ ), which indicates that these trajectories will return to the lowest energy state shortly after reaching this point. The associated relaxation time was found to be 18 fs. Dynamics at the water cluster were found to be slower with only 6 out of 10 trajectories relaxing to the ground state in the simulated period with a time constant of 274 fs.

The CASSCF trajectories provide additional information, as they do not suffer from the breakdown at small  $S_0$ - $S_1$  energy gaps that occurs in the ADC(2) calculations. Deactivation time constants of 196 fs in water and 24 fs in methanol have been obtained from the CASSCF dynamics, similar as those found in the ADC(2) simulations. However, two different relaxation pathways were observed to occur in both cluster systems after returning to the lowest energy state: a restoring one where the electron and the proton are subsequently transferred back to DHI and a dissociative one where a hydrogen radical is ejected following one or more proton transfers. The restoring pathway is found to be dominant in the water cluster with 10 out of 20 trajectories adhering to this pathway while only 3 trajectories showed the dissociative behavior. Here, the decision which pathway is followed is governed by the geometry at the point where the trajectory switches

to the lowest energy state. Trajectories following the restoring pathway return to the lowest energy state when they are in a conformation with the initially formed hydronium ion still intact. Contrary to that, the dissociative pathway is initiated when a hydrogen has been transferred from this hydronium ion along one of the two solvent-solvent hydrogen bonds, which results in the formation of a hydronium ion closer to the solvated electron. The electrostatic attraction between the solvated electron and the positively charged molecule facilitates further proton transfers until a proton is ejected into the space occupied by the solvated electron. Subsequently, the proton and the solvated electron form a hydrogen radical and leave the microsolvation cluster. In the MeOH-DHI cluster, the opposite ratio is observed with most trajectories deactivating via dissociation of a hydrogen radical and only a few restore the initial electronic and nuclear conformation of DHI. This can be reasoned by looking at the MeOH-MeOH hydrogen bond of the initially doubly protonated solvent molecule. This proton transfer is associated with a downhill potential energy profile in the first excited state, resulting in a fast occurring proton transfer, after which the crossing with the ground state occurs. Subsequent dissociation towards the solvated electron from this conformation readily occurs in a few femtoseconds.

The dynamics simulated provided new insights on the deactivation channels in solvated DHI. The restoring pathway indicates very fast deactivation of the cluster system once the initial stage of the dynamics is reached. Both the restoring and the dissociative pathways were found to be accessible in both cluster systems although the ratio of the chosen pathway is reversed when going from the water where the restoring pathway is dominant to MeOH. However, the dissociative mechanism results in the formation of additional reactive species that get separated from the DHI radical, hindering fast recombination. Hence, the relaxation of DHI in solvent results in the formation of solvated electrons, DHI radicals and hydrogen radicals. The reactivity of these species increases the likelihood of formation of new photoproducts during the relaxation mechanism. DHI in solution therefore exhibits phototoxic properties which is contrary to the photoprotective function observed in melanins. However, it still remains an open question if and to what extent, solvent-pigment interactions play a role in the deactivation mechanism of the whole melanin pigment. This is due to the solvent-excluding nature of the pigments that stems from the tight stacking conformation and the unknown participation of solvent-pigment interactions at the edges of the pigment. To investigate the extent of this interaction in the larger pigment, much larger systems have to be considered that include not one monomer but one or more stacks of oligomers of the eumelanin building blocks in solution. The computational effort associated with this size of cluster models renders the presented dynamics approach unfeasible at the moment and new methodological models will have to be developed to study larger systems.

# A. Appendix

## A.1 Initial Stationary Calculations

	MeOH-DHI			H <sub>2</sub> O-DHI		
	$E(S_1)$	$E(S_2)$	$E(S_3)$	$E(S_1)$	$E(S_2)$	$E(S_3)$
B3LYP/DZP	0.12	1.03	2.69	0.93	1.05	2.58
B3LYP/TZP	0.02	0.93	2.60	0.98	1.11	2.52
PBE0/DZP	0.50	1.44	3.01	-0.46	0.62	2.20
PBE0/TZP	0.32	1.25	2.90	0.73	1.08	2.62
CAM-B3LYP/DZP	1.35	2.46	4.20	0.38	1.63	3.26
CAM-B3LYP/TZP	1.19	2.28	3.74	0.24	1.47	2.91
$\omega$ B97X/DZP	2.23	3.47	4.63	1.36	2.75	4.30
$\omega$ B97X/TZP	2.03	3.25	4.46	1.21	2.57	4.07
ADC(2)/def2-SVP	2.42	3.55	4.35	1.68	2.97	4.23
SA-CASSCF/cc-pVDZ	1.99	3.40	4.83	0.61	2.18	3.45
CASPT2/cc-pVDZ	1.64	3.03	3.88	0.92	2.38	3.56

**Table A.1:** Excitation energies for the three lowest-lying excited states calculated at different levels of theory. All excitation energies are given in eV. Energies are given with respect to the electronic closed shell state.

## A.2 Increasing the Size of the Microsolvation Model

As has been shown in Section 3.3, the microsolvation model breaks down once the proton is ejected towards the solvated electron. In all trajectories that follow the dissociative pathway, the formed hydrogen radical leaves the simulated solvent shell. Once this event occurs in one of the trajectories, no further information about the deactivation mechanism can be obtained. This mainly affected the interpretation of the deactivation mechanism in MeOH where most of the trajectories followed this pathway. As mentioned in Section 3.3.3, two different kinds

of pathways are conceivable after formation of a hydrogen radical: the hydrogen radical penetrates deeper into the solvent, which would facilitate the formation of long lived radical species, as recombination of the two radicals is hampered due to the distance between the radicals. Alternatively, the hydrogen radical would be subject to interactions with the second layer of solvent molecules. This hinders the hydrogen radical from leaving the cluster. Therefore, the hydrogen radical would remain closer to the DHI radical for a longer time, which in turn supports recombination of both radicals. In order to know which pathway is more likely to occur in the MeOH-DHI cluster, more solvent molecules within the microsolvation cluster would be required before the dynamics simulations are conducted. In this section, a method to systematically increase the size of the microsolvation cluster is presented which can help to further investigate the behavior of the hydrogen radical. For this, two things are needed: first, the places where additional solvent molecules would have the strongest impact on the hydrogen radical should be determined. Second, the placement of these solvent molecules should not result in an unrealistic arrangement of solvent molecules.

The position of the additional solvent molecules was estimated by plotting the momentum of the hydrogen radicals that leave the initial microsolvation cluster, see Figure A.1a. There, two main “escape” routes can be distinguished: one

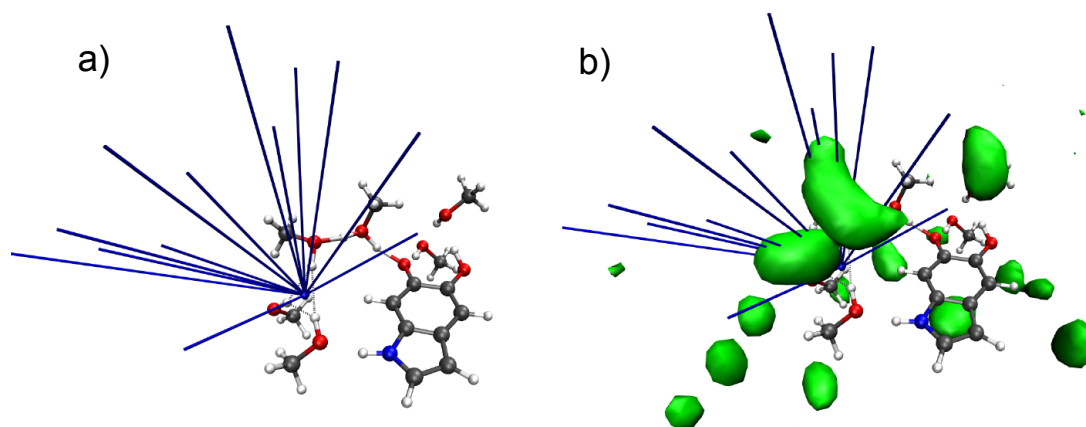


**Figure A.1:** Left hand side: Ejection paths of the hydrogen radicals. Right hand side: mass-weighted distributions of MeOH molecules as sampled from a MD simulation where the initial cluster system was held fixed.

where most of the hydrogen radicals leave the cluster along the empty site atop the triangle, and another where the hydrogens leave along the one side of the triangle where no methyl group of one of the MeOH molecules is present. To block the initiation of these two escape routes, the addition of two MeOH molecules at these two positions should increase the time where the hydrogen radical is subject to solvent effects by simulating a local additional solvent shell. Accordingly, two

MeOH molecules were placed at the suggested positions and their exact positions determined through reoptimization of the whole cluster system to promote a favorable hydrogen bonding for all molecules. However, due to time limitations, the corresponding excited state dynamics have not been conducted with the larger cluster model.

In an attempt to verify the placement of the MeOH molecules, classical MD simulations have been conducted using Amber16.<sup>78</sup> In these simulations 535 additional MeOH molecules have been simulated around the initial cluster system for 1 million time steps of 0.1 fs per time step. This simulation was then used to calculate locations where the simulated MeOH molecules preferred to stay during the simulations via summing the mass harbored by each point in space during the whole simulation. Regions that showed a higher than average mass are preferred positions due to the electrostatic interactions with the fixed solvent cluster. These high-density regions are shown on the right hand side in Figure A.1b where it can be seen that a high density of MeOH molecules is obtained for the two main escape channels of the hydrogen radicals. However, this attempt of verifying if these placements accord to areas that preferentially harbor a MeOH molecule may work for other cluster systems, but breaks down for this cluster system. The reason for this is the existence of a solvated electron and the corresponding change in the geometric features of this cluster system. Although the solvated electron is nonexistent in the classical MD simulation, the geometric configuration of its stabilizing triangle in the initial cluster has a huge impact on the dynamics. Three MeOH molecules are stabilizing the solvated electron with hydrogen atoms that are pointing to each other. In the MD simulation, the neutralizing effect of the solvated electron is missing and a large positive partial charge is generated due to the proximity of three hydrogens. This in turn attracts the oxygen of a MeOH molecule which then stays at this position for the remainder of the simulation. Inclusion of a negatively charged dummy atom at the center of the triangle should negate these effects and make this kind of verification viable. However, this was not done in the course of this thesis as some more work would have been required to balance the total charges of the initial MeOH-DHI cluster when introducing this negative charged dummy atom. Nevertheless, a suitable approach to increase the size of the microsolvation cluster has been presented which can be used in the future to investigate the dissociative pathway in more detail.

### **A.3 Influence of the Chosen Method on the Geometry of the Clusters**

Throughout this work, the cluster systems were taken from Reference 18. These cluster systems were obtained via TDDFT calculations at the CAM-B3LYP/cc-pVDZ level of theory. As discussed in Section 3.2.1, the same level of theory

could not be used in the dynamics simulations. Instead those were conducted at both the ADC(2)/def2-SVP and the CASSCF/cc-pVDZ levels of theory using an active space of six electrons in seven orbitals in the CASSCF calculations. For these calculations, the initial geometries for the cluster systems were used that were obtained using TDDFT. In general, TDDFT based methods are considered to give more accurate structures than the other two methods which was the reason for directly using these geometries. However, later examination of the CASSCF trajectories showed a strong tendency to increase the size of the triangle spanned by the three hydrogen atoms that stabilize the solvated electron. Although this effect was to be expected to some extent when going from the static calculations to dynamic ones, the observed changes were larger than assumed. To gain more information about this behavior, the two cluster systems were optimized in the  $S_1$  state at the CASSCF/cc-pVDZ level of theory. For this, the bond length of  $^1\text{H}_{pt}$  to the initial ion was held fixed in the MeOH-DHI cluster, as elongation of this bond corresponds to a downhill energy profile in the  $S_1$ . The reason why this elongation is unwanted is based upon the nature of the cation in the cluster systems as these represent transition state-like structures in the deactivation process. In the water cluster, such restrictions were not necessary as the elongation of all OH bonds in the hydronium ion are associated with uphill energy profiles. The resulting CASSCF “optimized” cluster systems are shown in Figure A.2 together with the initial TDDFT cluster systems. When comparing the geometries obtained at different levels of theory, two differences are observed. First, the size of the triangle spanned by the three solvated electron-stabilizing hydrogens is much larger in the CASSCF cluster systems than in the TDDFT ones. Such differences in the geometries predicted by two different methods for the cavity that stabilizes the solvated electron have been observed before, see supporting information of Reference 79. Second, almost all intermolecular distances are slightly larger in the CASSCF cluster systems. This means that a more compact cluster is favored at the CAM-B3LYP/cc-pVDZ level of theory than at the CASSCF/cc-pVDZ one. Hence, when using these TDDFT cluster systems as the initial point of a dynamics simulation using CASSCF/cc-pVDZ, the system will start in a strained conformation as all intermolecular distances are shorter than the optimized distances for this electronic structure method. The dynamics calculations will therefore result in a strong expansion of the whole system in the first few time steps. How much this affects the deactivation dynamics of the two cluster systems is unknown. A method to estimate if and how this alters the observed relaxation mechanism would consist in performing the dynamics calculations starting from the CASSCF “optimized” cluster system.

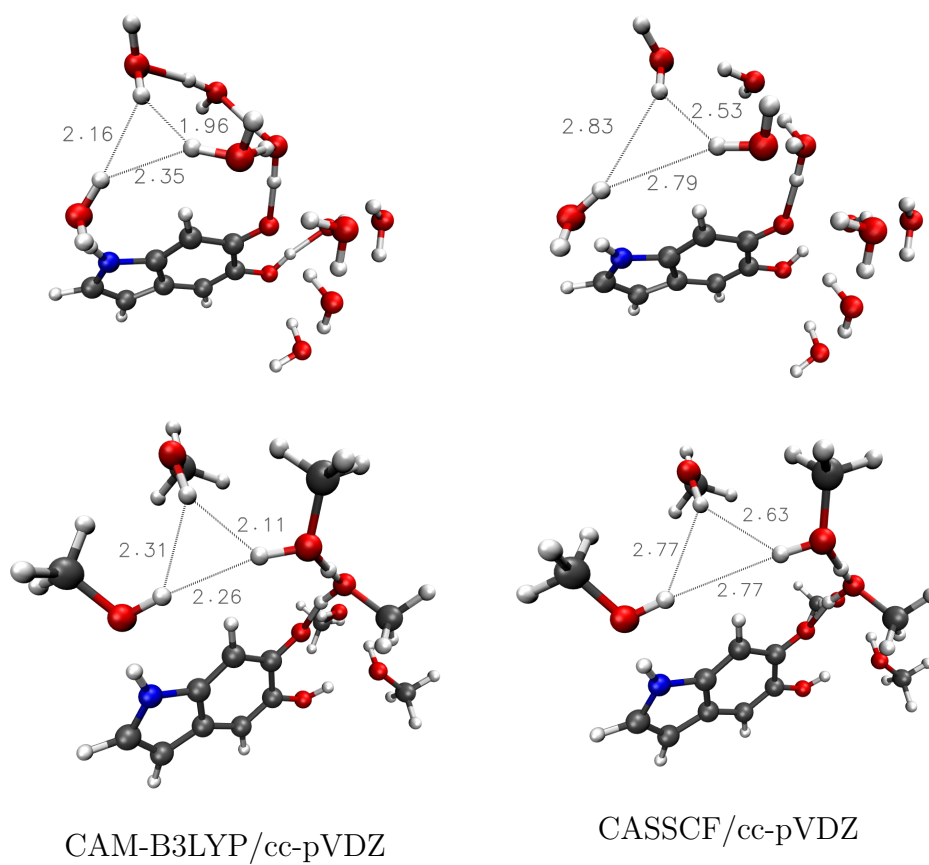


**Figure A.2:** Initial cluster systems as taken from Reference 18 and the corresponding CASSCF cluster systems.

## Bibliography

- [1] F. Solano. Melanins: Skin pigments and much more - types, structural models, biological functions, and formation routes. *New J. Sci.*, 2014(5):498276, 2014.
- [2] A. Huijser, A. Pezzella, and V. Sundström. Functionality of epidermal melanin pigments: current knowledge on UV-dissipative mechanisms and research perspectives. *Phys. Chem. Chem. Phys.*, 13:9119–9127, 2011.
- [3] M. d’Ischia, K. Wakamatsu, F. Cicoira, E. Di Mauro, J. C. Garcia-Borron, S. Commo, I. Galván, G. Ghanem, K. Kenzo, P. Meredith, A. Pezzella, C. Santato, T. Sarna, J. D. Simon, L. Zecca, F. A. Zucca, A. Napolitano, and S. Ito. Melanins and melanogenesis: from pigment cells to human health and technological applications. *Pigment Cell Melanoma Res.*, 28(5):520–544, 2015.
- [4] A. A. R. Watt, J. P. Bothma, and P. Meredith. The supramolecular structure of melanin. *Soft Matter*, 5:3754–3760, 2009.
- [5] P. Meredith and T. Sarna. The physical and chemical properties of eumelanin. *Pigment Cell Res.*, 19(6):572–594, 2006.
- [6] J. D. Simon, D. Peles, K. Wakamatsu, and S. Ito. Current challenges in understanding melanogenesis: bridging chemistry, biological control, morphology, and function. *Pigment Cell Melanoma Res.*, 22(5):563–579, 2009.
- [7] J. B. Nofsinger and J. D. Ye, T. and Simon. Ultrafast nonradiative relaxation dynamics of eumelanin. *J. Phys. Chem. B*, 105(14):2864–2866, 2001.
- [8] T. Ye and J. D. Simon. Comparison of the ultrafast absorption dynamics of eumelanin and pheomelanin. *J. Phys. Chem. B*, 107(40):11240–11244, 2003.
- [9] P. Meredith, B. J. Powell, J. Riesz, S. P. Nighswander-Rempel, M. R. Pederson, and E. G. Moore. Towards structure-property-function relationships for eumelanin. *Soft Matter*, 2:37–44, 2006.

- [10] M. L. Tran, B. J. Powell, and P. Meredith. Chemical and structural disorder in eumelanins: A possible explanation for broadband absorbance. *Biophys. J.*, 90(3):743–752, 2006.
- [11] E. Kaxiras, A. Tsolakidis, G. Zonios, and S. Meng. Structural model of eumelanin. *Phys. Rev. Lett.*, 97:218102–218106, 2006.
- [12] M. d’Ischia, O. Crescenzi, A. Pezzella, M. Arzillo, L. Panzella, A. Napolitano, and V. Barone. Structural effects on the electronic absorption properties of 5,6-dihydroxyindole oligomers: The potential of an integrated experimental and DFT approach to model eumelanin optical properties. *Photochem. Photobiol.*, 84(3):600–607, 2008.
- [13] K. B. Stark, J. M. Gallas, G. W. Zajac, M. Eisner, and J. T. Golab. Spectroscopic study and simulation from recent structural models for eumelanin: I. monomer, dimers. *J. Phys. Chem. B*, 107(13):3061–3067, 2003.
- [14] C.-T. Chen, C. Chuang, J. Cao, V. Ball, D. Ruch, and M. J. Buehler. Excitonic effects from geometric order and disorder explain broadband optical absorption in eumelanin. *Nat. Commun.*, 5:3859, 2014.
- [15] G. Prampolini, I. Cacelli, and A. Ferretti. Intermolecular interactions in eumelanins: a computational bottom-up approach. I. small building blocks. *RSC Adv.*, 5(48):38513–38526, 2015.
- [16] S. Meng and E. Kaxiras. Mechanisms for ultrafast nonradiative relaxation in electronically excited eumelanin constituents. *Biophys. J.*, 95(9):4396–4402, 2008.
- [17] D. Tuna, A. Udvarhelyi, A. L. Sobolewski, W. Domcke, and Domratcheva T. Onset of the electronic absorption spectra of isolated and  $\pi$ -stacked oligomers of 5,6-dihydroxyindole: An *Ab Initio* study of the building blocks of eumelanin. *J. Phys. Chem. B*, 120(14):3493–3502, 2016.
- [18] J. J. Nogueira, A. Corani, A. El Nahhas, A. Pezzella, M. d’Ischia, L. González, and V. Sundström. Sequential proton-coupled electron transfer mediates excited-state deactivation of a eumelanin building block. *J. Phys. Chem. Lett.*, 8(5):1004–1008, 2017.
- [19] A. L. Sobolewski and W. Domcke. Photophysics of eumelanin: Ab initio studies on the electronic spectroscopy and photochemistry of 5,6-dihydroxyindole. *ChemPhysChem*, 8(5):756–762, 2007.
- [20] M. Gauden, A. Pezzella, L. Panzella, A. Napolitano, M. d’Ischia, and V. Sundström. Ultrafast excited state dynamics of 5,6-dihydroxyindole, a key eumelanin building block: Nonradiative decay mechanism. *J. Phys. Chem. B*, 113(37):12575–12580, 2009.

- [21] A. Corani, A. Huijser, A. Iadonisi, A. Pezzella, V. Sundström, and M. d’Ischia. Bottom-up approach to eumelanin photoprotection: Emission dynamics in parallel sets of water-soluble 5,6-dihydroxyindole-based model systems. *J. Phys. Chem. B*, 116(44):13151–13158, 2012.
- [22] A. Datar and A. Hazra. Pathways for excited-state nonradiative decay of 5,6-dihydroxyindole, a building block of eumelanin. *J. Phys. Chem. A*, 121(14):2790–2797, 2017.
- [23] E. Schrödinger. An undulatory theory of the mechanics of atoms and molecules. *Phys. Rev.*, 28:1049–1070, Dec 1926.
- [24] E. Schrödinger. Quantisierung als eigenwertproblem. *Ann. Phys.*, 384(4):361–376, 1926.
- [25] M. Born and R. Oppenheimer. Zur quantentheorie der molekeln. *Ann. Phys.*, 389(20):457–484, 1927.
- [26] D. R. Hartree. The wave mechanics of an atom with a non-coulomb central field. part I. theory and methods. *Math. Proc. Cambridge*, 24(1):89–110, 1928.
- [27] J. C. Slater. The Theory of Complex Spectra. *Phys. Rev.*, 34:1293–1322, 1929.
- [28] C. C. J. Roothaan. New developments in molecular orbital theory. *Rev. Mod. Phys.*, 23:69–89, 1951.
- [29] P Löwdin. Correlation problem in many-electron quantum mechanics I. review of different approaches and discussion of some current ideas. *Adv. Chem. Phys.*, 2:207–322, 1959.
- [30] F. Jensen. *Introduction to Computational Chemistry*. John Wiley & Sons, 2006.
- [31] E. U. Condon. The theory of complex spectra. *Phys. Rev.*, 36:1121–1133, Oct 1930.
- [32] B. O. Roos, P. R. Taylor, and P. E. M. Siegbahn. A complete active space SCF method (CASSCF) using a density matrix formulated super-CI approach. *Chem. Phys.*, 48(2):157–173, 1980.
- [33] J. Olsen. The CASSCF method: A perspective and commentary. *International Journal of Quantum Chemistry*, 111(13):3267–3272, 2011.
- [34] C. Møller and M. S. Plesset. Note on an approximation treatment for many-electron systems. *Phys. Rev.*, 46:618–622, Oct 1934.

- [35] K. Andersson, P. Å. Malmqvist, B. O. Roos, A. J. Sadlej, and K. Wolinski. Second-order perturbation theory with a CASSCF reference function. *J. Phys. Chem.*, 94(14):5483–5488, 1990.
- [36] P. Å. Malmqvist, A. Rendell, and B. O. Roos. The restricted active space self-consistent-field method, implemented with a split graph unitary group approach. *J. Phys. Chem.*, 94(14):5477–5482, 1990.
- [37] B. O. Roos and K. Andersson. Multiconfigurational perturbation theory with level shift - the Cr<sub>2</sub> potential revisited. *Chem. Phys. Lett.*, 245(2):215–223, 1995.
- [38] J. Finley, P. Å. Malmqvist, B. O. Roos, and L. Serrano-Andrés. The multi-state CASPT2 method. *Chem. Phys. Lett.*, 288(2-4):299–306, 1998.
- [39] J. Schirmer. Beyond the random-phase approximation: A new approximation scheme for the polarization propagator. *Phys. Rev. A*, 26:2395–2416, Nov 1982.
- [40] A. B. Trofimov and J. Schirmer. An efficient polarization propagator approach to valence electron excitation spectra. *J. Phys. B: At., Mol. Opt. Phys.*, 28(12):2299, 1995.
- [41] A. Dreuw and M. Wormit. The algebraic diagrammatic construction scheme for the polarization propagator for the calculation of excited states. *Wiley Interdiscip. Rev. Comput. Mol. Sci.*, 5(1):82–95, 2015.
- [42] P. Hohenberg and W. Kohn. Inhomogeneous electron gas. *Phys. Rev.*, 136:B864–B871, Nov 1964.
- [43] Y. A. Wang, N. Govind, and E. A. Carter. Orbital-free kinetic-energy density functionals with a density-dependent kernel. *Phys. Rev. B*, 60:16350–16358, Dec 1999.
- [44] W. Kohn and L. J. Sham. Self-consistent equations including exchange and correlation effects. *Phys. Rev.*, 140:A1133–A1138, Nov 1965.
- [45] E. Runge and E. K. U. Gross. Density-functional theory for time-dependent systems. *Phys. Rev. Lett.*, 52:997–1000, Mar 1984.
- [46] A. Dreuw and M. Head-Gordon. Single-reference ab initio methods for the calculation of excited states of large molecules. *Chemical Reviews*, 105(11):4009–4037, 2005.
- [47] J. C. Tully and R. K. Preston. Trajectory surface hopping approach to nonadiabatic molecular collisions: The reaction of H<sup>+</sup> with D<sub>2</sub>. *J. Chem. Phys.*, 55(2):562–572, 1971.

- [48] P. Marquetand, J. Richter, M. and González-Vázquez, I. Sola, and L. González. Nonadiabatic ab initio molecular dynamics including spin-orbit coupling and laser fields. *Faraday Discuss.*, 153:261–273, 2011.
- [49] M. Richter, P. Marquetand, J. González-Vázquez, I. Sola, and L. González. SHARC: ab initio molecular dynamics with surface hopping in the adiabatic representation including arbitrary couplings. *J. Chem. Theory Comput.*, 7(5):1253–1258, 2011. PMID: 26610121.
- [50] S. Mai, P. Marquetand, and L. González. A general method to describe intersystem crossing dynamics in trajectory surface hopping. *Int. J. Quantum Chem.*, 115(18):1215–1231, 2015.
- [51] L. Verlet. Computer "experiments" on classical fluids. I. thermodynamical properties of lennard-jones molecules. *Phys. Rev.*, 159:98–103, Jul 1967.
- [52] J. C. Tully. Molecular dynamics with electronic transitions. *J. Chem. Phys.*, 93(2):1061–1071, 1990.
- [53] E. Wigner. On the quantum correction for thermodynamic equilibrium. *Phys. Rev.*, 40:749–759, Jun 1932.
- [54] J. P. Dahl and M. Springborg. The morse oscillator in position space, momentum space, and phase space. *J. Chem. Phys.*, 88(7):4535–4547, 1988.
- [55] T. Yanai, D. P. Tew, and N. C. Handy. A new hybrid exchange-correlation functional using the Coulomb-attenuating method (CAM-B3LYP). *Chem. Phys. Lett.*, 393:51–57, July 2004.
- [56] T. H. Dunning Jr. Gaussian basis sets for use in correlated molecular calculations. i. the atoms boron through neon and hydrogen. *J. Chem. Phys.*, 90(2):1007–1023, 1989.
- [57] F. Aquilante, J. Autschbach, R. K. Carlson, L. F. Chibotaru, M. G. Delcey, L. De Vico, I. Fdez. Galván, N. Ferré, L. M. Frutos, L. Gagliardi, M. Garavelli, A. Giussani, C. E. Hoyer, G. Li Manni, H. Lischka, D. Ma, P. Å. Malmqvist, T. Müller, A. Nenov, M. Olivucci, T. B. Pedersen, D. Peng, F. Plasser, B. Pritchard, M. Reiher, I. Rivalta, I. Schapiro, J. Segarra-Martí, M. Stenrup, D. G. Truhlar, L. Ungur, A. Valentini, S. Vancoillie, V. Veryazov, V. P. Vysotskiy, O. Weingart, F. Zapata, and R. Lindh. Molcas 8: New capabilities for multiconfigurational quantum chemical calculations across the periodic table. *J. Comput. Chem.*, 37(5):506–541, 2016.
- [58] F. Aquilante, R. Lindh, and T. B. Pedersen. Unbiased auxiliary basis sets for accurate two-electron integral approximations. *J. Chem. Phys.*, 127(11):114107, 2007.

- [59] G. Ghigo, B. O. Roos, and P. Å. Malmqvist. A modified definition of the zeroth-order hamiltonian in multiconfigurational perturbation theory (caspt2). *Chem. Phys. Lett.*, 396(1):142–149, 2004.
- [60] J. P. Zobel, J. J. Nogueira, and L. González. The IPEA dilemma in CASPT2. *Chem. Sci.*, 8(2):1482–1499, 2017.
- [61] F. Weigend and R. Ahlrichs. Balanced basis sets of split valence, triple zeta valence and quadruple zeta valence quality for H to Rn: Design and assessment of accuracy. *Phys. Chem. Chem. Phys.*, 7:3297–3305, 2005.
- [62] TURBOMOLE V6.2 2010, a development of University of Karlsruhe and Forschungszentrum Karlsruhe GmbH, 1989-2007, TURBOMOLE GmbH, since 2007; available from <http://www.turbomole.com>.
- [63] Axel D. B. Density-functional thermochemistry. III. the role of exact exchange. *J. Chem. Phys.*, 98(7):5648–5652, 1993.
- [64] C. Lee, W. Yang, and R. G. Parr. Development of the Colle-Salvetti correlation-energy formula into a functional of the electron density. *Phys. Rev. B*, 37:785–789, Jan 1988.
- [65] J.-D. Chai and M. Head-Gordon. Systematic optimization of long-range corrected hybrid density functionals. *J. Chem. Phys.*, 128(8):084106, 2008.
- [66] J.-D. Chai and M. Head-Gordon. Long-range corrected hybrid density functionals with damped atom-atom dispersion corrections. *Phys. Chem. Chem. Phys.*, 10:6615–6620, 2008.
- [67] C. Adamo and V. Barone. Toward reliable density functional methods without adjustable parameters: The PBE0 model. *J. Chem. Phys.*, 110(13):6158–6170, 1999.
- [68] E. Van Lenthe and E. J. Baerends. Optimized slater-type basis sets for the elements 1â118. *J. Comput. Chem.*, 24(9):1142–1156, 2003.
- [69] G. te Velde, F. M. Bickelhaupt, E. J. Baerends, C. Fonseca Guerra, S. J. A. van Gisbergen, J. G. Snijders, and T. Ziegler. Chemistry with ADF. *J. Comput. Chem.*, 22(9):931–967, 2001.
- [70] C. Fonseca Guerra, J. G. Snijders, G. te Velde, and E. J. Baerends. Towards an order-n DFT method. *Theor. Chem. Acc.*, 99(6):391–403, Nov 1998.
- [71] Evert Jan Baerends, Tom Ziegler, A. J. Atkins, Jochen Autschbach, Donald Bashford, O. Baseggio, A. Bérces, F. Matthias Bickelhaupt, C. Bo, P. M. Boerritger, Luigi Cavallo, C. Daul, D. P. Chong, D. V. Chulhai, L. Deng,

- R. M. Dickson, J. M. Dieterich, D. E. Ellis, M. van Faassen, A. Ghysels, A. Giammona, Stan J. A. van Gisbergen, A. Goetz, A. W. Götz, S. Gusarov, F. E. Harris, P. van den Hoek, Z. Hu, Christoph R. Jacob, H. Jacobsen, L. Jensen, L. Joubert, J. W. Kaminski, G. van Kessel, C. König, F. Kootstra, A. Kovalenko, Mykhaylo Krykunov, Erik van Lenthe, D. A. McCormack, A. Michalak, M. Mitoraj, S. M. Morton, Johannes Neugebauer, V. P. Nicu, Louis Noodleman, V. P. Osinga, S. Patchkovskii, Michele Pavanello, C. A. Peeples, Pierre Herman Theodoor Philipsen, D. Post, Cory C. Pye, H. Ramanantoanina, P. Ramos, W. Ravenek, J. I. Rodríguez, P. Ros, R. Rüger, P. R. T. Schipper, D. Schlüns, H. van Schoot, G. Schreckenbach, J. S. Seldenthuis, Mike Seth, Jaap G. Snijders, Miquel Solà, Stener M., M. Swart, D. Swerhone, G. te Velde, V. Tognetti, P. Vernooijs, L. Versluis, Lucas Visscher, O. Visser, Fan Wang, T. A. Wesolowski, E. M. van Wezenbeek, G. Wiesenekker, S. K. Wolff, T. K. Woo, and A. L. Yakovlev. ADF2017, SCM, Theoretical Chemistry, Vrije Universiteit, Amsterdam, The Netherlands, <https://www.scm.com>.
- [72] R. Szabla, R. W. Góra, M. Janicki, and J. Šponer. Photorelaxation of imidazole and adenine via electron-driven proton transfer along H<sub>2</sub>O wires. *Faraday Discuss.*, 195:237–251, 2016.
- [73] G. A. Worth, P. Hunt, and M. A. Robb. Nonadiabatic dynamics: A comparison of surface hopping direct dynamics with quantum wavepacket calculations. *J. Phys. Chem. A*, 107(5):621–631, 2003.
- [74] F. Plasser, R. Crespo-Otero, M. Pederzoli, H. Lischka, and M. Barbatti. Surface hopping dynamics with correlated single-reference methods: 9H-adenine as a case study. *J. Chem. Theory Comput.*, 10(4):1395–1405, 2014.
- [75] S. Mai, M. Richter, M. Ruckebauer, M. Oppel, P. Marquetand, and L. González. Sharc: Surface hopping including arbitrary couplings - program package for non-adiabatic dynamics. [sharc-md.org](http://sharc-md.org), 2014.
- [76] F. Neese. The ORCA program system. *Wiley Interdiscip. Rev. Comput. Mol. Sci.*, 2(1):73–78, 2012.
- [77] B. G. Levine, J. D. Coe, and T. J. Martínez. Optimizing conical intersections without derivative coupling vectors: Application to multistate multireference second-order perturbation theory (MS-CASPT2). *J. Phys. Chem. B*, 112(2):405–413, 2008.
- [78] D. A. Case, D. S. Cerutti, T. E. Cheatham, III, T. A. Darden, R. E. Duke, T. J. Giese, H. Gohlke, A. W. Goetz, D. Greene, N. Homeyer, S. Izadi, A. Kovalenko, T. S. Lee, S. LeGrand, P. Li, C. Lin, J. Liu, T. Luchko, R. Luo, D. Mermelstein, K. M. Merz, G. Monard, H. Nguyen, I. Omelyan,

A. Onufriev, F. Pan, R. Qi, D. R. Roe, A. Roitberg, C. Sagui, C. L. Simmerling, W. M. Botello-Smith, J. Swails, R. C. Walker, J. Wang, R. M. Wolf, X. Wu, L. Xiao, D. M. York, and P. A. Kollman. Amber 2017, 2017. University of California, San Francisco.

- [79] A. Kumar, J. A. Walker, D. M. Bartels, and M. D. Sevilla. A simple ab initio model for the hydrated electron that matches experiment. *J. Phys. Chem. A*, 119(34):9148–9159, 2015.

# Acknowledgments

This thesis has been developed from February to September 2017 in the group of Prof. Leticia González at the University of Vienna.

First, I want to thank Prof. Leticia González not only for the possibility to conduct my master studies in her group but also for the continuous support throughout my time in the group.

Next, I want to thank Dr. Juan Jose Nogueira who provided me with an interesting system to study. Despite the difficulties associated with this system, the many discussions with him helped me overcome the many obstacles encountered during my work and were essential for completing this thesis.

Special thanks go to Dr. Sebastian Mai, who patiently endured my endless questions and failed attempts to use SHARC, as well as to everyone who kept my computer and my jobs running, namely Dr. Markus Oppel, Markus Hickl, and Dimitri Robl.

Furthermore, I want to thank Patrick Zobel, Dr. Michael Gastegger, Maximilian Meixner, Davide Avagliano, and Julia Westermayr for helpful discussions during my work. I am very grateful for all the numerous people in this group I had the honor and joy of working together or sharing a room with, that made my time in this group enjoyable.

Finally, I want to thank all my family for their continued support and for their patience and desire to understand what I was doing in for my thesis.